HAWASSA UNIVERSITY

SCHOOL OF POSTGRADUATE STUDIES

COLLEGE OF NATURAL AND COMPUTATIONAL SCIENCES

DEPARTMENT OF CHEMISTRY

BIOSYNTHESIS OF Fe_3O_4/Co_3O_4 NANOCOMPOSITE FOR PHOTOCATALYTIC DEGRADATION OF CONGO RED AND MALACHITE GREEN DYES UNDER SOLAR IRRADIATION

MSc THESIS

BY:

AKINAW AGALU TAYE

ADVISOR: Prof. SISAY TADESSE (PhD)

NOVEMBER, 2024

HAWASSA, ETHIOPIA

BIOSYNTHESIS OF Fe_3O_4/Co_3O_4 NANOCOMPOSITE FOR PHOTOCATALYTIC DEGRADATION OF CONGO RED AND MALACHITE GREEN DYES UNDER SOLAR IRRADIATION

BY

AKINAW AGALU TAYE

ADVISOR: Prof. SISAY TADESSE (PhD)

A THESIS SUBMITTED TO THE DEPARTMENT OF CHEMISTRY, COLLEGE OF NATURAL AND COMPUTATIONAL SCIENCES, SCHOOL OF GRADUATE STUDIES OF HAWASSA UNIVERSITY IN PARTIAL FULFILLMENT OF THE REQUIREMENTS FOR THE DEGREE OF MASTERS OF SCIENCE IN PHYSICAL CHEMISTRY

NOVEMBER, 2024

HAWASSA, ETHIOPIA

DECLARATION

I hereby declare that this MSc thesis entitled **"Biosynthesis of Fe_3O_4/Co_3O_4 Nanocomposite for Photocatalytic Degradation of Congo red and Malachite green Dyes under Solar Irradiation"** is my original work and has not been presented for a degree in any other university. All sources of material used for this thesis have been duly acknowledged.

AKINAW AGALU TAYE _____ _____

Student Name Signature Date

This MSc thesis has been submitted for examination with my approval as thesis advisor.

Prof. Sisay Tadesse (PhD) _____ _____

Advisor Name Signature Date

ADVISORS' APPROVAL SHEET

SCHOOL OF GRADUATE STUDIES

HAWASSA UNIVERSITY

This is to certify that the thesis entitled **"Biosynthesis of Fe_3O_4/Co_3O_4 Nanocomposite for Photocatalytic Degradation of Congo red and Malachite green Dyes under Solar Irradiation"** submitted in partial fulfillment of the requirements for the Degree of Master's with specialization in Physical Chemistry, the Graduate Program of the Chemistry Department/School of Natural and Computational Sciences, and has been carried out by **AKINAW AGALU**, ID No**; GPPhyCR/0001/14**, under my supervision. I have read and evaluated this thesis, which complies with the regulations of the university and meets the required standards with respect to originality and quality. Therefore, I recommend that the student has fulfilled the requirements and hence hereby can submit the thesis to the department with my approval as a university advisor.

Prof. Sisay Tadesse (PhD)	_____	_____
Advisor Name	Signature	Date

EXAMINERS' APPROVAL SHEET

SCHOOL OF GRADUATE STUDIES

HAWASSA UNIVERSITY

We, the undersigned, members of the Board of Examiners of the final Thesis open defense by **AKINAW AGALU** have read and evaluated his thesis entitled **"Biosynthesis of Fe_3O_4/Co_3O_4 Nanocomposite for Photocatalytic Degradation of Congo red and Malachite green Dyes under Solar Irradiation"** and examined the candidate. This is, therefore, to certify that the thesis has been accepted in partial fulfillment of the requirements for the Degree of Master of Science in Physical Chemistry.

_____	_____	_____
Name of Advisor	Signature	Date
_____	_____	_____
Name of Chairperson	Signature	Date
_____	_____	_____
Name of Internal examiner	Signature	Date
_____	_____	_____
Name of External examiner	Signature	Date
_____	_____	_____
SGS Approval	Signature	Date

Signature Date Final approval and acceptance of the thesis is contingent upon the submission of the final copy of the thesis to the School of Graduate Studies (SGS) through the Department/School Graduate Committee (DGC/SGC) of the candidate's department.

Stamp of the SGS Date: _____

ACKNOWLEDGEMENT

First and for most, I would like to thank the almighty God for everything. Then, I wish to express my sincere thanks and gratitude to my advisor Prof. Sisay Tadesse (PhD), for his effective and intellectual guidance, encouragement, and support of fruitful ideas throughout my thesis work. He was also always approachable and patient with me and gave me the confidence to finalize this thesis work.

I wish also to extend my gratitude to Hawassa University Chemistry Department for accepting me to study for my MSc degree program. Then I would like to thank Adama science and Technology University for their support for the characterization of my samples.

I would like to acknowledge my associate technical staff member, Mr. Tilahun Tumiso, for providing a pleasant and friendly working environment in the laboratory during the experimental work. I extend my thanks to Yohannes Shuka, the chief laboratory chemist and researcher, for his unwavering support during lab sessions and with software.

I am very grateful to the Chirone Woreda Education Office in Sidama Regional State for sponsoring me to do this post-graduate study at Hawassa University.

Last but not least, I would especially like to thank my classmates and friends for the support that I need during my Studies. Finally, I also extend my thanks to my family for their endless prayers and supporting in all possible ways to the success thesis work and MSc degree program.

TABLE OF CONTENTS

CONTENTS PAGE

DECLARATION II

ADVISORS' APPROVAL SHEET III

EXAMINERS' APPROVAL SHEET IV

ACKNOWLEDGEMENT V

TABLE OF CONTENTS VI

LIST OF FIGURES X

LIST OF TABLES XII

LIST OF APPENDICES XIII

LIST OF ACRONYMS AND ABBREVIATIONS XIV

ABSTRACT XV

CHAPTER ONE 1

1. INTRODUCTION 1

1.1. Background of the Study 1

1.2. Statement of the Problem 3

1.3. Objectives of the Study 5

1.3.1. General objective 5

1.3.2. Specific objectives 5

1.4. Significance of Study 5

CHAPTER TWO 6

2. LITERATURE REVIEW 6

2.1. Metal Oxide Nanoparticles (MONPs) 6

2.2. Synthesis of Metal Oxide Nanoparticles 7

2.2.1. Physical method for synthesis of metal oxide nanoparticles 8

2.2.2. Chemical method for synthesis of metal oxide nanoparticles 8
2.2.3. Green method for synthesis of metal oxide nanoparticles 9
2.3. Properties of Iron Oxide (Fe_3O_4) and Cobalt Oxide (Co_3O_4) Nanoparticles 9
2.4. Fe_3O_4/Co_3O_4 Nanocomposite (NCs) 11
2.5. *Bougainvillea spectabilis* 12
2.6. General about Organic Dyes and their Toxicity 13
2.7. Factors influencing the photocatalytic degradation 16
2.7.1. Catalyst dosage 16
2.7.2. Temperature 16
2.7.3. Initial dye concentration 16
2.7.4. pH of dyes 17
2.7.5. Reaction time 17
2.8. Photocatalysis 18
2.9. Pseudo Kinetics of Photocatalytic Degradation 18
2.10. Advanced Oxidation Process (AOP) 20
CHAPTER THREE 23
3. MATERIALS AND METHODS 23
3.1. Chemicals and Reagents 23
3.2. Instrument and Apparatus 23
3.3. Preparation of *Bougainvillea spectabilis* Flower Extract 24
3.4. Biosynthesis of Iron Oxide (Fe_3O_4), Cobalt Oxide (Co_3O_4) NPs and Fe_3O_4/Co_3O_4 Nanocomposites 24
3.4.1. Biosynthesis of Fe_3O_4 NPs 24
3.4.2. Biosynthesis of Co_3O_4 NPs 25
3.4.3. Biosynthesis of Fe_3O_4/Co_3O_4 NCs 26
3.5. Characterizations of Nanoparticles and Nanocomposites 27

3.6. Photocatalytic Degradation of Congo red and Malachite green Dyes 28
3.6.1. Photocatalyst dosage 28
3.6.2. Initial concentration of the dye 29
3.6.3. Exposure time 29
3.6.4. pH of dyes 29
3.7. Instrumental Calibration 29
3.8. Kinetics Study 29
3.9. Study on Catalyst Reusability 30
CHAPTER FOUR 31
4. RESULTS AND DISCUSSION 31
4.1. Characterization of Synthesized Nanoparticles and Nanocomposites 31
4.1.1. Ultraviolet-Visible (UV-Vis) Spectroscopy Analysis 31
4.1.2. Fourier Transform Infrared Spectroscopy (FT-IR) Analysis 34
4.1.3. Scanning Electron Microscope (SEM) Analysis 36
4.1.4. X-Ray Diffraction (XRD) Analysis 37
4.2. Evaluation of Photocatalytic Activity 40
4.2.1. Effect of photocatalyst dosage 40
4.2.2. Effect of the initial concentration of CR and MG 42
4.2.3. Effect of exposure time 43
4.2.4. Effect of the solution pH 44
4.3. Kinetics Study 46
4.3.1. Pseudo-zero-order kinetics 47
4.3.2. Pseudo-first-order kinetics 48
4.3.3. Pseudo-second-order kinetics 49
4.4. Photocatalytic Degradation Mechanisms 50
4.5. Catalyst Reusability Tests 52

CHAPTER FIVE 54
5. CONCLUSION AND RECOMMENDATION 54
5.1. Conclusion 54
5.2. Recommendation 55
REFERENCES 56
APPENDICES 65

LIST OF FIGURES

Figure 1: Top-down vs. Bottom-up synthesis schemes [29] 8

Figure 2: Plant and *B. spectabilis* flower [picture taken by investigator, Feb 2024] 13

Figure 3: Chemical structure of the Congo red (A) and Malachite green (B) dyes 15

Figure 4: Schematic illustration of the dye degradation mechanism 21

Figure 5: Flow chart for the preparation of *B. spectabilis* flower extract 24

Figure 6: Flow diagram of the synthesis of Fe_3O_4 NPs 25

Figure 7: Flow diagram of the synthesis of Co_3O_4 NPs 26

Figure 8: Flow diagram of the synthesis of Fe_3O_4/Co_3O_4 NCs 27

Figure 9: UV-Vis spectra of biosynthesized pure Fe_3O_4 NPs (a), Co_3O_4 NPs (b), and Fe_3O_4/Co_3O_4 NCs (c) 31

Figure 10: Tauc's plot bandgap energy of biosynthesized Fe_3O_4 NPs (a), Co_3O_4 NPs (b) and Fe_3O_4/Co_3O_4 NCs (c) 32

Figure 11: FT-IR spectra of the *B. Spectabilis* flower extract (a), Fe_3O_4 NPs (b), Co_3O_4 NPs (c) and Fe_3O_4/Co_3O_4 NCs (d) 34

Figure 12: SEM images and histogram of particle size distribution analysis for the Fe_3O_4 NPs (a), Co_3O_4 NPs (b), and Fe_3O_4/Co_3O_4 NCs (c) 37

Figure 13: XRD patterns for Fe_3O_4 NPs (a), Co_3O_4 NPs (b) and Fe_3O_4/Co_3O_4 NCs (c) 38

Figure 14: Effect of nano photocatalyst loading on the photocatalytic degradation CR and MG by biosynthesized pure Fe_3O_4 NPs (a), Co_3O_4 NPs (b), and Fe_3O_4/Co_3O_4 NCs (c), with 20 ppm/25 mL for CR and 15 ppm/25 mL for MG 41

Figure 15: Effect of initial concentration of CR and MG on the photocatalytic degradation by biosynthesized Fe_3O_4 NPs (a), Co_3O_4 NPs (b), and Fe_3O_4/Co_3O_4 NCs (c), photocatalyst dosage: 0.09 gm/25mL for CR and photocatalyst dosage: 0.06 gm /25mL for MG 42

Figure 16: Effect of exposition time on the photocatalytic degradation of CR and MG by biosynthesized Fe_3O_4 NPs (a), Co_3O_4 NPs (b), and Fe_3O_4/Co_3O_4 NCs (c),

photocatalyst dosage: 0.09 gm/25 mL, initial concentration 20 ppm for CR and photocatalyst dosage: 0.06 gm/25mL, initial concentration 15 ppm for MG.....44

Figure 17: Effect of solution pH on the photocatalytic degradation of CR and MG by biosynthesized Fe_3O_4 NPs (a), Co_3O_4 NPs (b), and Fe_3O_4/Co_3O_4 NCs (c), photocatalyst dosage: 0.09 gm/25mL, Initial concentration; 20 ppm, reaction time 75 min for CR and photocatalyst dosage 0.06 gm/25mL, Initial concentration; 15 ppm and reaction time 90 min for MG 45

Figure 18: Calibration curves of initial concentration of CR and MG 46

Figure 19: Pseudo zero-order kinetic model for the photocatalytic degradation of CR and MG by biosynthesized pure Fe_3O_4 NPs (a), Co_3O_4 NPs (b), and Fe_3O_4/Co_3O_4 NCs (c) respectively 47

Figure 20: Pseudo-first-order kinetic model for the photocatalytic degradation of CR and MG by biosynthesized Fe_3O_4 NPs (a), Co_3O_4 NPs (b), and Fe_3O_4/Co_3O_4 NCs (c) respectively.....48

Figure 21: Pseudo-second-order kinetic model for the photocatalytic degradation of CR and MG by biosynthesized Fe_3O_4 NPs (a), Co_3O_4 NPs (b), and Fe_3O_4/Co_3O_4 NCs (c) respectively.....49

Figure 22: Possible mechanisms of photocatalytic degradation of CR and MG in the presence of sunlight irradiation with *B. spectabilis* flower extract-mediated biosynthesized Fe_3O_4/Co_3O_4 NCs 52

Figure 23**:** Recyclability of pure Fe_3O_4, Co_3O_4 NPs, and Fe_3O_4/Co_3O_4 NCs for the degradation of CR (a) and MG (b) 53

LIST OF TABLES

Table 1: The optical band gap energies of biosynthesized Fe_3O_4, Co_3O_4 NPs, and Fe_3O_4/Co_3O_4 NCs 33

Table 2: X-ray diffraction (XRD) analysis of biosynthesized nanomaterials 39

Table 3: Rate constant (k) and correlation coefficient (R^2) calculated for the kinetic model for the photocatalytic degradation of CR and MG by biosynthesized pure Fe_3O_4 NPs, Co_3O_4 NPs, and Fe_3O_4/Co_3O_4 NCs 50

LIST OF APPENDICES

Appendix 1: Effect of Photocatalyst Dosage 65

Appendix 2: Effect of Initial Concentration of CR and MG 66

Appendix 3: Effect of Exposure Time 68

Appendix 4: Effect of pH 70

Appendix 5: Calibration Curve Data 72

Appendix 6: Kinetic Data 72

Appendix 7: Photocatalyst Reusability 75

LIST OF ACRONYMS AND ABBREVIATIONS

AOPs	Advanced Oxidation Processes
B. spectabilis	*Bougainvillea spectabilis*
CB	Conduction band
CR	Congo red
E_g	Energy bandgap
FT-IR	Fourier Transforms Infrared Spectroscopy
MG	Malachite Green
MONPs	Metal Oxide Nanoparticles
MRI	Magnetic Resonance Imaging
NPs	Nanoparticles
NCs	Nanocomposites
SEM	Scanning Electron Microscope
SPR	Surface plasmon resonance
TMO	Transition metal oxide
UV-Vis	Ultra violet-visible
VB	Valence band
XRD	X-ray Diffractometer

ABSTRACT

The global concern regarding environmental pollution caused by organic pollutants, as population growth and industrial expansion, has increased the demand for the development of efficient nanomaterials for pollution control. In this study, Fe_3O_4, Co_3O_4 NPs, and Fe_3O_4/Co_3O_4 NCs were synthesized using a green method involving the extract of B. spectabilis flowers. Characterization of the synthesized nanomaterials was conducted using UV-Vis, FT-IR, SEM, and XRD. UV-Vis analysis confirmed the successful synthesis and optical properties of Fe_3O_4, Co_3O_4 NPs, and Fe_3O_4/Co_3O_4 NCs at the nanoscale via green methods, with energy band gaps measured at 2.18 eV, 2.2 eV, and 1.98 eV respectively. FT-IR analysis indicated the presence of peaks corresponding to Fe-O 484 cm^{-1} and Co-O 558 cm^{-1} bonds. SEM images revealed that the Fe_3O_4, Co_3O_4 NPs, and Fe_3O_4/Co_3O_4 NCs exhibited a smooth surface with non-uniform, rough, and closely packed irregular granular structures. A sponge-like morphology characterized by numerous irregular pores was observed, combined with surface functionalization of Fe_3O_4 due to Co_3O_4 nanoparticle agglomeration, which displayed a smooth and uniform morphology. The average particle size distributions were determined to be 1949 nm, 1437 nm, and 1622 nm respectively. XRD analysis confirmed the successful synthesis of Fe_3O_4, Co_3O_4 NPs, and Fe_3O_4/Co_3O_4 NCs, revealing planes indicative of a high degree of crystallinity in the iron oxide phase and a cubic spinel structure for cobalt oxide. Multiple diffraction peaks corresponding to the spinel structures of both Fe_3O_4 and Co_3O_4 were observed, with crystallite sizes determined to be 31.02 nm 19.05 nm, and 24.2 nm respectively. Photocatalytic activity towards CR and MG using Fe_3O_4/Co_3O_4 NCs, maximum degradation efficiencies of 96.13% for CR (catalyst dose of 0.09 g, initial concentration of 20 ppm, exposure time of 75 min, pH of 6) and 94.40% for MG (catalyst dose of 0.06 g, initial concentration of 15 ppm, exposure time of 90 min, and pH of 8). The degradation efficiencies of 93.65% for CR and 91.39% for MG by Fe_3O_4 NPs, as well as Co_3O_4 NPs, which demonstrated efficiencies of 92.57% for CR and 90.57% for MG were achieved under optimal conditions. Kinetic studies revealed that the Fe_3O_4/Co_3O_4 NCs follow a pseudo-first-order kinetic model for the degradation of CR, exhibiting the highest correlation coefficient ($R^2 = 0.988$). In contrast, the degradation of MG follows a pseudo-second-order kinetic model, with the highest correlation coefficient ($R^2 = 0.997$).

Keywords: Photocatalytic degradation, Fe_3O_4/Co_3O_4 NCs, *Bougainvillea spectabilis*

CHAPTER ONE

1. INTRODUCTION

1.1. Background of the Study

The risk of environmental pollution has increased as industrialization has progressed [1]. Every year, about 700,000 tons of organic dyes are produced worldwide. During production, 12% of these are lost in effluents, and 20% are released into wastewater after usage. Overall, industries are thought to emit approximately 150,000 tons of dyes into effluents annually [2, 3]. These organic dyes reduce the amount of oxygen required for aquatic life in the marine environment by forming a layer on the water's surface. In addition, organic dyes have several negative consequences on plants and human health when they are discharged into the environment. In general, they are toxic, carcinogenic, and non-biodegradable [4]. Due to these toxic chemicals' strong chemical stability and resistance to standard techniques, getting free of them from industrial effluents has become a serious concern for both human health and the environment. Diverse methods have been proposed for removing organic dyes from wastewater; nevertheless, heterogeneous photocatalysis is far more beneficial than the other methods [5]. Researchers possess difficulties in developing techniques for dye degradation. Ion exchange, chemical oxidation, ozonolysis, photocatalytic degradation, and coagulation-based procedures are some of these strategies. Water pollutants can be removed through adsorption. On the other hand, photocatalytic degradation with a semiconductor photocatalyst is considered an economical and environmentally friendly method of effectively degrading organic dyes [1].

The fastest-moving industries in science and technology are producing green technologies. One of the most fascinating subjects used to create and use materials with interatomic structural features is nanotechnology. In the 21st century, nanotechnology has become a scientific innovation. Particles with sizes between 1 and 100 nm and diameters on a one-billionth-of-meter scale are collectively referred to as nanoparticles. Generally, there are two ways to create nanoparticles: "top-down" and "bottom-up." The beginning approach involves breaking down more substantial structures (bulk) by the use of cutting, grinding, and ablation methods until a nanometric structure is achieved. However, the chemical characteristics of atoms and molecules that cause them to attract one another and cluster together to form an ordered structure of nanometric size are typically eliminated by the

bottom-up method. Several synthetic pathways employ this methodology, such as the sol-gel technique, chemical vapor deposition, Pechini, microemulsion, green synthesis, and so on. Nanoparticles are modern substances that have a wide range of uses in the chemical, pharmaceutical, agricultural, medical, and electrical industries. One of the fundamental goals of chemistry has been the biosynthesis of nanoparticles with desired morphology (shape, size, and crystalline nature), which can be used for a variety of applications, such as catalysis, biomedicine, less expensive electrodes, and biosensors. Aside from their unique physical and chemical characteristics, nanoparticles functioned as a link between bulk materials and molecular or atomic structure. As a result, they are the ideal choice for many crucial applications, including electrochemistry, biotechnology, medicine, and trace material identification [6, 7].

Nowadays, metal oxide nanoparticles are the most useful material on planet Earth, particularly for preventing environmental pollution, delivering drugs, enhancing battery cells, acting as a catalyst during synthesis, and having antibacterial properties [8–10]. One interesting option for photocatalytic applications is Fe_3O_4, a metal oxide photocatalyst [11]. It has a bandgap of 2.1 eV, is low in synthesis cost, does not produce secondary pollutants, and exhibits n-type semiconducting characteristics [12].

The Co_3O_4 NPs have direct optical band gaps of around 1.48 and 2.19 eV, making them suitable for application as a photocatalyst in the visible light degradation of organic pollutants [13]. Co_3O_4 is a black, antiferromagnetic, p-type semiconductor material that crystallizes in a normal spinel structure based on a cubic close-packing arrangement of oxide ions. In Co_3O_4, Co^{2+} ions occupy eight tetrahedral A-sites, while Co^{3+} ions occupy sixteen octahedral B-sites. Significant research has been done on Co_3O_4 nanoparticles, which have the chemical formula AB_2O_4. The process of gradually replacing the Co metal ions in their structure with other metal ions (Mg and Ni, Fe, Mn, Cd, Cu, Pd, Mo), resulting in the development of a mixed cobalt oxide, is one such well-established method of changing their properties. As a result, several methods for producing cobalt oxide and mixed cobalt oxides have been reported, including simple combustion, sol- gel, hydrothermal, chemical spray pyrolysis, chemical vapor deposition, and facile solvothermal process [14].

The three main categories of wastewater treatment methods for dye removal are physical, chemical, and biological. Physical techniques such as ion exchange, oxidation, radiation, and adsorption are frequently employed; however, they can be labor-intensive, complex, and

require multiple processing steps. On the other hand, the photocatalytic degradation process is gaining popularity as a successful dye removal technique. It is a productive and eco-friendly technique for wastewater dye degradation. It is an appropriate choice for the treatment of colored effluents from many sectors due to its selectivity, efficiency, flexibility, and affordability. Large dye molecules are oxidized during this process to produce smaller byproducts including water, carbon dioxide, and minerals. It is a modern method that is often used to remove pigments or break down dyes. This process involves the movement of electrons from the valence band to the conduction band on a semiconductor surface upon exposure to a wavelength-appropriate light. After that, the excitons are formed and react with oxygen or water to form superoxide anions and hydroxide radicals, which have strong oxidizing abilities that can break down a variety of compounds, including dyes. These processes of decontamination, which make use of reactive oxygen species (ROS) as well as other reactive species, are referred to as Advanced Oxidation Processes (AOPs) [15, 16].

Traditional medicines, or natural products derived from plants, animals, and microorganisms, represent the oldest forms of healthcare worldwide and are used for illness prevention and treatment. Phytochemical analysis of the stem, leaves, and flowers of *B. spectabilis* revealed the presence of alkaloids, flavonoids, furanoids, glycosides, phenols, phlobotannins, quinones, saponins, steroids, tannins, and terpenoids [17].

In this study, Fe_3O_4, Co_3O_4 nanoparticles, and Fe_3O_4/Co_3O_4 nanocomposites were synthesized by green synthesis method using *Bougainvillea spectabilis* flower extract as a reducing and capping agent during the synthesis of the nanocomposite not only stabilizes the nanoparticles but may also contribute to the photocatalytic activity by providing additional functional groups that can enhance the degradation process. Finally, the synthesized nanoparticles and nanocomposites were used for the photocatalytic degradation of Congo red and Malachite green dyes under sunlight irradiation.

1.2. Statement of the Problem

In contrast to physical methods, chemical methods have been the preferred method for producing nanomaterials in recent decades. However, chemical methods themselves can be costly, energy-intensive, and sometimes even involve toxic or hazardous chemicals, the residue of which is thought to be environmentally hazardous. Additionally, using these techniques to produce nanoparticles may result in the production of waste materials and other byproducts that limit their application in biomedicine [18]. Scientists have recently

introduced biological or green method synthesis of nanomaterials, especially metal nanoparticles and their oxides, which helps to overcome some of the disadvantages and limits of nanoparticle synthesis methods, especially chemical methods.

Water pollution has been identified as one of the world's most serious problems since it can hurt people. As a result, many people die each year from diseases that are brought on by contaminated water. Particularly problematic to the environment are pollutants originating from the discharge of effluents from industries like textile, cosmetics, paint, plastic, pharmaceutical, paper, pesticides, herbicides, and petrochemicals. This is because these industries produce a significant amount of hazardous organic pigments, which makes treating effluents even more difficult. Currently, more than 10,000 different businesses use dyes, with the textile dying process utilizing the greatest amount of these dyes. Approximately 10-15% of organic dyes are released into wastewater, and this suggests that they are a significant source of environmental pollution [19]. However, green or biological methods have made the process of producing nanoparticles simple, cost-effective, and health-friendly; these methods are considered to be economical, eco-friendly, and low-energy as they use plant extracts or natural organisms (bacteria, algae, viruses, etc.) as the stabilizing and mitigating agents instead of toxic and hazardous chemicals [20–22].

Green synthesis of metal oxide nanoparticles (Nps) and metal oxide nanocomposites (NCs) is an innovative, eco-friendly, and low-cost method for degrading organic dyes along with water treatment. In this study, the efficiency of the synthesized Fe_3O_4/Co_3O_4 nanocomposite in degrading specific dyes Congo red and Malachite green compared to existing photocatalysts. This could fill a gap in knowledge regarding the performance of this specific nanocomposite under solar irradiation.

Green synthesis of NPs minimizes waste generation in the synthesis process and implements sustainable processes. The research might assess the environmental impact of using these nanocomposites in treating dye-contaminated water, contributing to discussions on sustainable practices in wastewater treatment. So in this work for best treatment efficiency the above limitation will be improved by synthesizing Fe_3O_4/Co_3O_4 NCs using the aqueous flower extract of *Bougainvillea spectabilis* as a reducing and capping agent.

1.3. Objectives of the Study

1.3.1. General objective

The main objective of this study was to investigate the photocatalytic activity of biosynthesized Fe_3O_4/Co_3O_4 nanocomposite for photocatalytic degradation of Congo red and Malachite green dyes under solar irradiation.

1.3.2. Specific objectives

- To biosynthesis Fe_3O_4, Co_3O_4 NPs, and Fe_3O_4/Co_3O_4 NCs via using *B. spectabilis* flower extract as a reducing agent and capping agent.
- To analysis the synthesized Fe_3O_4, Co_3O_4 NPs, and Fe_3O_4/Co_3O_4 NCs using various characterization techniques such as UV-Vis, FT-IR, SEM, and XRD.
- To evaluate the key parameters and kinetics of biosynthesized Fe_3O_4, Co_3O_4 NPs, and Fe_3O_4/Co_3O_4 NCs in degrading the CR and MG dyes under sunlight irradiation.
- To compare the photocatalytic degradation efficiency of biosynthesized Fe_3O_4/Co_3O_4 NCs over pure Fe_3O_4, and Co_3O_4 NPs, for the photocatalytic degradation of CR and MG dyes under sunlight irradiation.

1.4. Significance of Study

This study demonstrates the utilization of aqueous flower extract of *Bougainvillea spectabilis* for the synthesis of Fe_3O_4/Co_3O_4 NCs, highlighting a green chemistry approach. This method is environmentally friendly, reducing the need for toxic chemicals typically used in nanoparticle synthesis and promoting sustainability in material production. Furthermore, the focus on degrading harmful organic dyes like CR and MG addresses a significant environmental issue, as these dyes are known for their toxicity and persistence in the environment. Developing an efficient photocatalytic method to degrade them can have substantial implications for wastewater treatment and pollution control. Additionally, the study emphasizes the use of solar irradiation as an energy source for photocatalysis, aligning with global efforts to harness renewable energy. This makes the process more sustainable and cost-effective compared to traditional energy sources. The biosynthesis of the Fe_3O_4/Co_3O_4 NCs presents a potential advancement in photocatalytic materials. Moreover, this study bridges multiple fields, including materials science, environmental science, chemistry, and botany. It encourages interdisciplinary collaboration that can lead to innovative solutions for complex environmental challenges.

CHAPTER TWO

2. LITERATURE REVIEW

2.1. Metal Oxide Nanoparticles (MONPs)

Nanomaterials are substances with at least one dimension that range from 1 to 100 nm with unique pores, shape, and other property characteristics. Metal oxides are produced when an oxygen gas and a metal cation interact. Because of their numerous shapes and characteristics, metal oxides are an interesting group of organic compounds that have been extensively studied and discovered. The attractive electrical, optical, and magnetic features of transition metal oxide nanoparticles make them particularly significant. Due to their varied forms and characteristics, these inorganic materials also referred to as metal oxides have gained the attention of researchers. Particularly, transition metal oxide nanoparticles exhibit desirable electrical, optical, and magnetic characteristics that make them ideal for a wide range of applications, such as sensors, lithium-ion batteries, environmental applications, and catalysis. Therefore, there is an increasing need to investigate their special qualities and features in a range of applications. Metal oxides are more difficult to synthesize than pure metals, and their bonds might be almost ionic, very covalent, or even metallic. Similar to this, MONPs have diverse properties that make them useful in a range of industries, such as solar energy conversion, sensors, electronics, catalytic processes, and magnetic storage media. TiO_2, Fe_3O_4, CuO, and ZnO are the metal oxide types that have been studied the most concerning plant-based metal oxide nanoparticle synthesis [23, 24].

As a result of their potent adsorption capabilities and electrocatalytic activities, transition metal oxide nanoparticles have drawn a lot of interest in electrochemical and biosensing applications. Iron oxide (Fe_3O_4) NPs are becoming more popular among metal oxides for use in biosensing applications given their attractive optical and magnetic properties, advantageous band gap, biocompatibility, nontoxicity, and high natural abundance. Because of the electron exchange between Fe^{2+} and Fe^{3+} ions, Fe_3O_4 NPs have strong electrical conductivity even at room temperature, providing new opportunities in the field of electrochemical sensing [25]. Fe_3O_4-NPs have been synthesized due to their special characteristics, which include their superparamagnetic, biocompatible, biodegradable, and expected non-toxicity to humans. Fe_3O_4-NPs unique properties enable their broad applicability in a wide range of areas, including biosensors, magnetic resonance imaging

(MRI), catalysis, magnetic storage media, and targeted delivery of drugs [26]. Transition metal oxides (TMOs) are highly efficient as a cathode catalyst material in fuel cells owing to their huge surface area, low diffusion path lengths, and various oxidation states. The following are a few examples: cobalt oxide (Co_3O_4), iron oxide (Fe_3O_4), nickel oxide (NiO), zinc oxide (ZnO), tungsten oxide (WO_3), manganese dioxide (MnO_2), vanadium oxide (V_2O_5), and molybdenum oxide (MoO_2) [27]. Among metal oxide nanoparticles, Co_3O_4 NPs have attracted significant research interest due to their low cost and good electroactivity. However, cobalt is a transition metal that can exhibit several possible oxidation states: Co^{2+}, Co^{3+}, and Co^{4+} [28].

2.2. Synthesis of Metal Oxide Nanoparticles

Green synthesis uses clean, safe, cost-effective, and environmentally friendly processes to construct nanomaterials. Microorganisms, including bacteria, yeast, fungi, algae, and certain plants, act as substrates for this green synthesis of nanomaterials. The final morphology and size of nanoparticles are determined by different active molecules and precursors, such as metal salts. Furthermore, green synthesis offers nanomaterial benefits ranging from antimicrobial to natural reducing and stabilizing properties. Certain enzymes, amino acid groups, proteins, or chemical structures are frequently found in the portion of green species that is used in the creation of nanomaterials. Nano-sized materials are synthesized in a multitude of ways, but there are generally two approaches to their creation: top-down and bottom-up synthesis (Figure 1). The former utilizes larger bulk materials and breaks them down into nano-sized particles, and the latter utilizes individual atoms and builds them up into larger nanomaterials. Traditional synthesis methods have fallen out of favor, which has paved the way for green synthesis. Given the ongoing climate crisis, it is crucial to develop innovative methods that adhere to the 12 Principles of Green Chemistry.

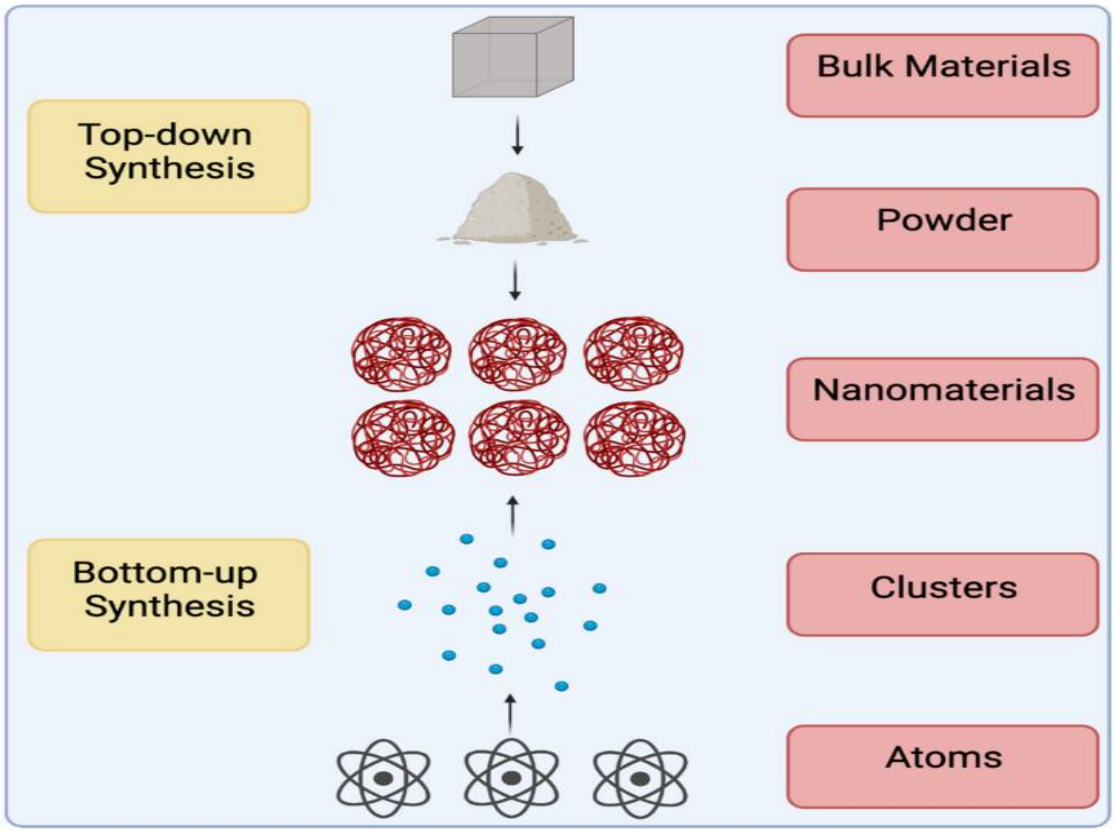

Figure 1: Top-down vs. Bottom-up synthesis schemes [29]

2.2.1. Physical method for synthesis of metal oxide nanoparticles

Thermolysis, physical vapor deposition (PVD), pulsed laser synthesis, microwave-assisted synthesis, high-energy ball milling, melt mixing, laser ablation, ion implantation, sputter deposition, electric arc deposition, and other physical techniques are used to synthesize nanoparticles. Every one of these methods modifies a single physical parameter; for instance, thermolysis modifies temperature, ball milling modifies pressure, ion implantation modifies pH, laser ablation modifies radiation, etc. By keeping the optimal parameters, it is possible to acquire the required size and shape of the nanoparticles. Physical methods have a few disadvantages, however, mainly expensive equipment, longer procedures, and high parameters that are harmful to the environment. On the other hand, physical methods can assist in producing nanoparticles with uniform size and structure [30].

2.2.2. Chemical method for synthesis of metal oxide nanoparticles

Chemical synthesis is a commonly employed technique for quickly and efficiently generating vast amounts of nanoparticles. The radiofrequency plasma method, co-precipitation, chemical vapor deposition, sol-gel process, and solvothermal synthesis are

some of these techniques. To control the size and stabilize the synthesized nanoparticles, these procedures require capping agents like triethanolamine, oleic acid, and thioglycerol, as well as powerful reducing agents to reduce the nanoparticles. The primary drawbacks of chemical techniques are their high toxicity and high chemical expense [30].

2.2.3. Green method for synthesis of metal oxide nanoparticles

Green fabrication is becoming more and more popular as an eco-friendly substitute for conventional chemical processes in the production of MONPs. Green synthesis refers to methods, techniques, and strategies that use processing, cleaning, control, and regulation to minimize energy use and get free of hazardous byproducts. The main principles of green synthesis include waste reduction and minimization, the use of renewable raw materials, environmentally friendly or non-toxic solvents and additives, and both. Green synthesis techniques can be used more successfully to produce metallic nanoparticles since reduction and capping agents are required by the synthesis processes. Natural sources for the environmentally benign creation of nanoparticles include actinomycetes, bacteria, yeast, fungal organisms, and cyanobacteria in addition to plant components (fruit, root, flower, and leaves). The entire algal cell, a plant-microbe, or an extract can be used as a reducing medium to produce nanoparticles and as a capping medium to stabilize those nanoparticles [23].

The biological, or "green," method offers a more ecologically friendly way to synthesize nanoparticles than the chemical and physical methods. Furthermore, this process does not call for expensive, dangerous, or hazardous ingredients. The biological approach, which has been widely employed recently, makes it possible to create metallic nanoparticles with a wide range of contents, sizes, forms, and physicochemical characteristics. Biological organisms such as bacteria, action bacteria, yeasts, molds, algae, and plants, or their byproducts, can be used to complete synthesis in a single step. The creation of nanoparticles is carried out by the reduction of molecules found in plants and microbes, including proteins, enzymes, phenolic compounds, amines, alkaloids, and pigments [31, 32].

2.3. Properties of Iron Oxide (Fe_3O_4) and Cobalt Oxide (Co_3O_4) Nanoparticles

In macroscopic applications, iron reactivity is quite important (especially in rusting), but it is more noticeable at the nanoscale. In its finely split condition, it is pyrophoric. Due to its high reactivity, it is difficult to find and undesirable for use in applications. On the other hand, self-heating, applying an external magnetic field, and moving into magnetic resonance

along the attraction field can all quickly activate iron oxide NPs [33]. Since iron is present in large quantities in the human body and is tolerated at higher concentrations than other metals, iron oxide NPs are typically the most desired and utilized NPs [34]. Iron oxide NPs have garnered a lot of interest and have been studied extensively because of their remarkable properties, which include their low toxicity, simple synthesis, large surface area, dependable surface modification, and superparamagnetic qualities [35, 36]. The magnetic p-type semiconductor cobalt oxide (Co_3O_4) NPs are a member of the significant class of inorganic metal oxides with a normal spinel structure and a cubic close-packing array of oxide ions. In addition to other important features like easy synthesis, varied shape, and excellent catalytic capacity. Co_3O_4 has possibilities in the fields of fuel cells for the production of renewable energy, photocatalysis for the treatment of wastewater, lithium batteries for energy storage applications, gas sensors for biomedical applications, and artificial photosynthesis. Because of its different availability and cost-effectiveness [37]. Cobalt oxide (Co_3O_4) nanomaterials are currently more attractive due to their simple preparation method, diverse morphology, high catalytic activity, and applicability in electrocatalysis [38].

The oxidation state and electronic configuration of a transition metal ion determine its magnetic properties. Co_3O_4 is a p-type semiconductor with a low direct optical band gap which is known for its quantum tunneling magnetization. The most stable phase of Co_3O_4 with a direct optical bandgap of 1.48 and 2.19 eV, cobalt oxide is a multifunctional, antiferromagnetic p-type semiconductor [39]. In the cubic spinel crystal structure of Co_3O_4, the tetrahedral positions are occupied by Co^{2+} ions, and the octahedral sites by Co^{3+} ions. Crystal field splitting of $3d^6$ orbitals in an octahedral crystal field causes octahedral Co^{3+} ions to become diamagnetic. Electrons within the crystal field interact to pair electrons in lower triplet T_{2g} levels, which results in the diamagnetic state. Conversely, Co_3O_4, or $Co^{2+}[Co^{3+}]_2O_4$, has a normal spinel crystal structure because the p states of O_2^- ions are close to the d states of Co^{3+} ions. This allows for the simple transition of p electrons, which results in two UV absorption bands: $p(O^{2-}) \rightarrow E_g(Co^{3+})$ and $p(O^{2-}) \rightarrow T_2(Co^{2+})$. When size is lowered to the nano realm, thermal energy outweighs anisotropy energy, explaining the reason Co_3O_4 NPs are frequently super-paramagnetic at room temperature. Co_3O_4 NPs are attractive in magnetic, optical, and electrochemical applications, especially photocatalysis and magneto-optical ones, because of their distinct optical characteristics [40].

Co_3O_4 displays a distinct magnetic order from Fe_3O_4, which is ferromagnetic, despite the crystallographic similarities between the two materials. Mechanical hardness, strong electrical resistance, and chemical stability are other attributes of cobalt oxides. As a result of the interaction between Co and Fe and O, these physical and chemical characteristics encourage the production of stable oxides on the surface of metals and alloys, which helps to prevent low-carbon steels from corroding in acids [41]. Iron oxide (Fe_3O_4) is the most prevalent natural iron oxide with an inverse spinel structure. While black crystalline materials possess a larger field stabilization energy than other substances, ferrous (Fe^{2+}) ions occupy half of the octahedral positions of the Fe_3O_4 spinel structure, whereas Fe^{3+} ions occupy the remaining octahedral positions and all tetrahedral sites. Fe_3O_4 nanoparticles' magnetic behavior is highly dependent on their fabrication technique. Additionally, magnetite's magnetic properties are largely determined by the NPs shape. Therefore, understanding the ideal Fe_3O_4 nanoparticle characteristics is essential for improved applicability [42, 43].

2.4. Fe_3O_4/Co_3O_4 Nanocomposite (NCs)

Composite substances with at least one dimension less than 100 nm are known as nanocomposites. The unique design possibilities and multifunctional features of nanocomposites have drawn the interest of scientists all around. Because of their numerous applications, nanocomposites are the materials of future generations. To create nanocomposites with distinctive features, scientists are attempting to develop new techniques for their synthesis on a global scale. By combining suitable ingredients for the synthesis of certain nanocomposites, researchers hope to increase the practical use of nanocomposite's effectiveness, efficiency, and durability. The utilization of transition metal oxide nanoparticles has been extensively investigated for several applications, among which are restricted to supercapacitors, sensors, solar cells, and photocatalysis. Additional research has revealed that these transition metal oxides can be modified by mixing or doping them with other nanoparticles, such as conducting polymers, metal oxide nanoparticles, carbon-based nanoparticles, etc., to increase their efficiency. This could lead to new applications in a variety of scientific fields, including chemistry, physics, biology, and material science. Through modification, transition metal oxide-based nanoparticles can acquire new characteristics, including increased conductivities, decreased electron-hole recombination, improved porosity, increased surface area, and increased surface activities. According to

current research, transition metal oxide-based nanocomposites have attracted a great deal of interest as flexible and advantageous materials with a wide variety of practical applications across practically all scientific domains. Although nanocomposites have a greater capacity for accepting electrons, more charges can be transferred between dyes and metals, generating excitation between electrons and holes and leading to improved photocatalytic activity. Free radicals (OH) are created when electrons and holes bound by hydroxyl ions combine to remove pollutants through redox processes [44, 45].

Researchers are interested in metal oxide nanocomposites for a variety of uses, including fuel cells, photocatalysis, sensors, antibacterial agents, and UV protection [46]. Magnetic Fe_3O_4 is a well-known and widely desired transition metal oxide NPs because of its high ratio of spin polarization, strong magnetic moment, and relatively high conductivity. However, because of their large surface area, bare Fe_3O_4 NPs readily aggregate irreversibly, which significantly reduces their electrical and optical performance. Fe_3O_4/Co_3O_4 NCs can break up these aggregations and supply Co ions with many valence states. Additionally, the hybridization of Co 3d and O 2p improves optical performance and electrical conductivity [40].

2.5. *Bougainvillea spectabilis*

A genus of flowering plants native to South America, Bougainvillea is part of the Nyctaginaceae family. Due to its great adaptability to several agro-climatic zones across the globe, it is primarily utilized in dry landscapes for horticultural, medicinal, agricultural, and environmental industries. This genus has 18 species: *B. berberidifolia, B. buttiana, B. campanulata, B. glabra, B. herzogiana, B. infesta, B. lehmanniana, B. lehmannii, B. malmeana, B. modesta, B. pachyphylla, B. peruviana, B. pomacea, B.praecox, B. spectabilis, B. spinosa, B. stipitata, and B. trollii,* with three that are horticulturally important which includes *B. spectabilis, B. glabra and B. peruviana*. The Brazilian species *B. spectabilis* is also utilized extensively. It reaches a height of six feet. Compared to other bougainvilleas, it has darker leaves that are hairy and have noticeable hairs on the underside. It has brilliant red or purple bracts that open in the summer [17, 47]. Thousands of phytochemicals derived from plants were discovered to be safe, widely useful substitutes with fewer side effects. Bougainvillea species have been shown to possess phenolics, flavonoids, alkaloids, anthocyanin, tannins, saponins, phytate, and oxalate. *B. spectabilis* is a rich source of extraordinary secondary metabolites with several pharmacological

properties like antibacterial, antioxidant, anticancer, antidiabetic, anti-inflammatory, and antihyperlipidemic [48].

Figure 2: Plant and *B. spectabilis* flower [picture taken by investigator, Feb 2024]

2.6. General about Organic Dyes and their Toxicity

Over 7×10^7 tons of dyestuff are produced annually worldwide, and there are more than 100,000 commercially available dyes [49]. The paper and textile industries are the main users of dyes. The usage of synthetic complex organic dyes as coloring agents has increased significantly in these industries. Environmental remediation efforts have recently focused on dye from the textile industry and other commercial dyestuffs. The existing industrial activity pattern releases new chemicals into the environment and modifies the normal flow of materials [50]. Dyes are an organic compound that absorbs light in the visible region. The main attributes of the dye include chromogen-chromophore conjugate system (electron acceptor), resonance of electron (delocalized π-electron of aromatic ring), and solubility. Chromogene is an aromatic ring of benzene, naphthalene, or anthracene, which binds chromophore (e.g., azo (—N=N—), methine (—CH=), carbonyl (=C=O), etc.) in double conjugated links. The conjugate system is responsible for the electromagnetic absorption that imparts color. The presence of electron donor-ionizable functional groups known as auxochrome (e.g., amino (—NH_2), carboxyl (—COOH), hydroxyl (—OH), etc.) improves the solubility of the dye in water. They intensify the color and confer the binding capacity of dye onto materials. Dye is typically used for coloring products in heavy industries such as textile, paper, and food processing. It is reported that the discharge of dyes in effluent accounts for 20 % of water pollution [51].

Dyes are characterized by their capacity to absorb light radiation in the visible spectrum (from 380 to 750 nm). The transformation of white light into colored light by reflection on a body or by transmission or diffusion results from the selective absorption of energy by certain groups of atoms called chromophoric groups. The more or less intense coloration of the different substances is linked to their chemical constitution. A dye is a body capable of absorbing certain luminous radiations and then reflecting the complementary colors. Before the middle of the 19^{th} century, dyes are made from natural materials like beetroot. Natural dyes can be derived from plants, animals, insects, and minerals. They are generally less allergenic and toxic than synthetic dyes and generate wastewater that can be treated by biodegradation [52, 53].

The textile, leather, paper, paint, and printing industries are among the many industries where organic dyes and pigments are thought to be the most frequent sources of water pollution. For instance, among paints, food dyes, food colorants, and other substances, textile industrial dyes contain many hazardous organic components and account for around 20% of all water contamination [54]. Dyes are categorized according to the functional groups present in their chemical structures, which determine their color and other characteristics. This results in a division into cationic and anionic dyes. When a basic dye dissociates from an aqueous solution, it releases a positively charged ion, which is known as a cationic dye. Since the majority of them have onium groups as function groups, the majority of the cations are N^+ ions. The cationic dye comprises crystal violet, malachite green, Rhodamine B, and methyl blue. The water-soluble anionic dye also referred to as acidic dye, contains anion as a functional group. The produced nano photocatalyst interacts well with anionic dyes that have a hydrophilic surface [55]. Malachite green and Congo red are among the commonly used industrial dyes in manufacturing industries, such as textile, paper, and food processing. An anionic dye, Congo red has a pKa of 4.5 and it is frequently utilized in the rubber, plastic, textile, and paper industries. It produces a red colloidal solution in water, which is thought to metabolize into benzidine, a substance that is mutagenic and carcinogenic to aquatic life. Triphenyl methane is the parent compound of malachite green, a cationic dye. Its auxochrome group has a positive charge density (pKa = 10.3) after being protonated in water at a low pH. Cotton, jute, paper, silk, wool, and leather products can all be dyed using malachite green. Furthermore, it is utilized in the fish farming industry for the treatment of bacterial, fungal, and parasitic diseases. Malachite green has many uses, but considering its

toxicity, it is hazardous for aquatic life and human health when it is present in water. It causes infections on the skin, eyes, lungs, and bones; it harms the liver, spleen, kidney, and heart; and it produces teratogenic effects on the brain and nervous system. In general, the release of dyes, even in trace amounts, into water resources is visually undesirable, hinders light penetration, and affects the gas solubility required for respiration and photosynthesis. However, human skin and eyes may get irritated when dissolved dyes come into physical touch with humans. Dyes, which are water-soluble and exhibit inherent chemical structures stable to photo-degradation and bio-degradation, pose a challenge for wastewater treatment. While a number of physicochemical and biological methods have been reported for their removal, biological treatment is often preferred for pilot-scale remediation of dye effluents. However, this method can be slow in achieving the desired removal state [50]. The complex aromatic structure of Congo red ($C_{32}H_{22}N_6Na_2O_6S_2$) makes it a diazo dye that is non-biodegradable and fairly stable as shown in Figure 3. It is almost impossible to extract from water due to its high solubility. It can be fatal and affect the skin, eyes, reproductive system, and respiratory system because of its carcinogenic qualities. The textile, culinary, wool, and silk industries all utilize Congo red. In addition, it serves as an indicator in acidic media as a biological stain for the diagnosis of amyloidosis in medicine [56, 57].

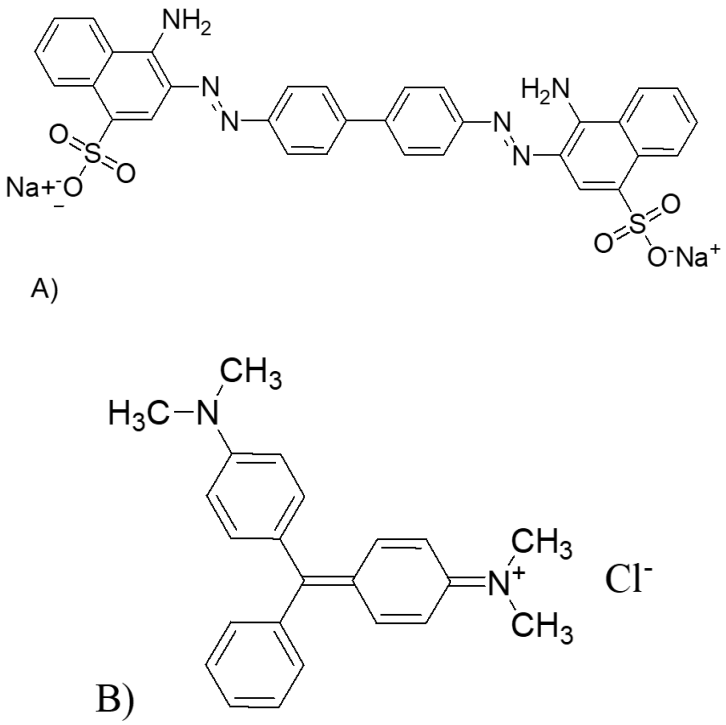

Figure 3: Chemical structure of the Congo red (A) and Malachite green (B) dyes

2.7. Factors influencing the photocatalytic degradation

The degradation of dye by a photocatalyst is influenced by specific factors including the catalyst dosage, temperature, initial dye concentration, pH, and intensity of light exposition. These parameters are considered to have an impact on the photodegradation process of organic dyes.

2.7.1. Catalyst dosage

Typically, as the amount of catalyst is increased, the rate of photodegradation also increases. This is because more active sites are available to absorb photons during irradiation, leading to the production of more $OH^{\bullet}$ radicals and positive holes. However, beyond a certain threshold, further increasing the catalyst dosage can decrease the rate of photodegradation. This decrease may be attributed to the formation of a turbid solution, hindering the penetration of UV/Vis radiation into the water. The agglomeration of nanoparticles can reduce the availability of active surface sites for exposure, resulting in the coagulation of catalyst particles [58].

2.7.2. Temperature

Temperature can affect the stability of the photocatalyst, the kinetics of chemical reactions, and adsorption/desorption processes. The adsorption of dye molecules onto the photocatalyst surface and their subsequent desorption are influenced by temperature. Higher temperatures may result in a reduction of adsorption and an increase in desorption, which could affect the degradation process's overall efficiency. The rate of reaction and the kinetics of degradation can be greatly influenced by temperature. Because of the improved molecular mobility and increased collision frequency at higher temperatures, reaction rates are frequently higher. The relation, potentially represented by the Arrhenius equation or other appropriate kinetic models, between temperature and the rate of photocatalytic degradation. The impact of temperature on the nanocomposite's long-term performance and reusability. Modifications in the composition and nature of degradation products brought on by temperature. Changes in the byproducts produced during the photocatalytic reaction as a result of temperature fluctuations [59].

2.7.3. Initial dye concentration

The degradation reaction of organic dyes is significantly influenced by their initial concentration. Several monolayers of adsorbed dye formed as the initial dye concentration

increased, increasing the number of adsorbed dye molecules that might be broken down. The surface is fully covered, resulting in a constant reaction rate until it reaches the critical level. On the other hand, as the dye concentration increases further, the degradation rate decreases. Photocatalysis depends on the adsorption of dyes onto the surface of the photocatalyst. In the photocatalytic process, only the amount of dye adsorbed on the photocatalyst's surface contributes to the reaction; the dye present in the bulk of the solution does not play a role. The adsorption of dye is influenced by its initial concentration, which an important factor to consider in any is given photocatalytic reaction. Generally speaking, the percentage of degradation decreases as the dye concentration increases, while keeping the amount of catalyst fixed [58].

2.7.4. pH of dyes

The pH plays a crucial role in the degradation of azo dyes by photocatalysts. It influences the ionization level of the photocatalyst, affecting the oxidation process. When the pH changes, it impacts the formation of hydroxyl radicals through the reaction of hydroxide ions and positive holes. At lower pH levels, positive holes are important for oxidation, while at neutral or higher pH levels, hydroxyl radicals become the primary oxidizing species. As the charge depends on the pH of a given solution, it follows that both pH and the nature of a particular dye influence the photocatalyst activity [60, 61].

2.7.5. Reaction time

Reaction time is an important factor in photocatalytic degradation because it influences how long the dye molecules and photocatalyst are in contact, which in turn impacts how much degradation proceeds. Reaction time also affects the process's overall efficiency and the kinetics of degradation. The relationship between dye degradation efficiency and reaction time. Influence on the kinetics of degradation, potentially determined with pseudo-zero order, pseudo-first-order, and pseudo-second-order kinetic models. Impact of reaction time on the adsorption of dye molecules onto the photocatalyst and their subsequent desorption during the degradation process. Variations in the degradation route are caused by variations in the formation of hydroxyl radicals and reactive oxygen species as a function of reaction time. Degradation product identification and concentration as a function of reaction time sheds light on the understanding of the degradation process over time [60, 62].

2.8. Photocatalysis

Among various chemical methods, photocatalysis, which utilizes clean solar energy to decompose organic compounds, offers a non-toxic and effective way to treat dye wastewater and is one of the most promising approaches. The process generally involves two steps: (1) generation of charge carriers under external excitation (e.g. light, electric, and thermal signals); and (2) reaction of these charge carriers with water to produce reactive species such as hydroxyl radicals ($^{\bullet}OH$) and superoxide anions ($^{\bullet}O_2^-$) that decompose the dyes [63]. Some specific steps involved in the degradation process such as photo-generation of electrons (e^-) and holes (h^+) pairs by excitation of an electron from the valence band (VB) to the conduction band (CB), separation of electrons (e^-) and holes (h^+) pairs then diffusion through the surface of the catalyst, photo-oxidation, and reduction of pollutants on the surface of the catalyst to convert them into harmless products like CO_2 and H_2O [65].

Heterogeneous photocatalysis reactions typically take place on the surface of semiconductor photocatalysts upon exposure to light photons. Generally, when a photocatalyst is irradiated under light having photon energy higher than the bandgap energy of the semiconductor, e^-(s) get excited from the valence band (VB) of the nanoparticles (NPs) to the conduction band (CB) and creates positive holes (h^+) in the VB. These photo-excited e^-/h^+ pairs may recombine to produce thermal energy, which prevents the photocatalysis process, or diffuses to the surface of the photocatalyst and reacts with the adsorbed molecules. The positive holes (h^+) react with H_2O, resulting in the production of hydroxyl radicals ($^{\bullet}OH$) while the conduction band electrons are trapped by the O_2 molecule to generate superoxide anion radical ($^{\bullet}O_2^-$). These reactive radicals rapidly and non-selectively degrade pollutants into more unaffected species [66].

2.9. Pseudo Kinetics of Photocatalytic Degradation

According to Langmuir-Hinshelwood (L-H), catalytic reaction proceeds in two steps. In the first step, the reactants are adsorbed on the surface of the photocatalyst, and in the second step; the adsorbed reactants react and give the final products [59, 67]. For quantification of the heterogeneous photocatalytic degradation activity, the Langmuir-Hinshelwood (L-H) model is considered, as shown in equation (1).

$$-\frac{dc}{dt} = \frac{kKC}{1 + KC'} \tag{1}$$

Where K and k are the thermodynamic adsorption constant, and degradation rate constant respectively, and C is the concentration of the dyes. Because one of the reactants acts as a catalyst whose concentration remains unchanged, the reaction kinetics can be simplified, and the term "pseudo" is used to prefix the reaction rate expression. At high concentrations of dye, the catalyst surfaces are fully covered, leading to the approximation of $(1 + KC)$ to the catalyst [68], since the photocatalytic degradation rate is independent of the change in the dye concentration, as shown in equation(2).

$$-\frac{dc}{dt} = k \tag{2}$$

Integrating the equation under the boundary conditions $C = C_0$ at $t = 0$, and $C = {}^{1}/_{2}\, C_0$ at $t = t\,{}^{1}/_{2}$ respectively yields

$$C_0 - C = k_0 t \tag{3}$$

$$t\,{}^{1}/_{2} = \frac{C_0}{2k_0} \tag{4}$$

A plot of $Co - C$ versus reaction time gives a slope equal to the zero-order rate constant(k_o). Additionally, half-life $\left(t\frac{1}{2}\right)$ is the time required to degrade half of the initial dye concentration, which is used to quantitatively compare the degradation reaction. Therefore, the zero-order $t\,{}^{1}/_{2}$ can be expressed by equation (4), and it increases with the initial concentration of dye molecules. On the other hand, at low initial concentrations of dye molecules, i.e., $(KC + 1) \approx 1$, a pseudo-first-order rate expression is obtained [69], as shown in Equation(5). The equation is valid by assuming the driving force of degradation is constantly proportional to the dye concentration.

$$-\frac{dc}{dt} = k_1 C \tag{5}$$

Where k_1 corresponds to the first-order rate constant. Integrating the equation under the two boundary conditions yields

$$\ln\frac{Co}{C_t} = k_1 t \tag{6}$$

$$t_{\frac{1}{2}} = \frac{ln2}{k_1} = \frac{0.693}{k_1} \tag{7}$$

The linear region can be obtained from the plot of $ln\frac{C_O}{C}$ versus reaction time, in which the slope gives the rate constant of degradation. This model is the most common one used to represent the entire degradation process. Here, the half-life is derived from Equation(7). The $t_{1/2}$ of the first-order model is independent of the dye concentration. A second-order reaction in which a single reactant is involved is characterized by the chemical reaction (2C→products). At equilibrium, the second-order kinetics depends on the amount of dye molecules adsorbed on the catalyst surface.

$$-\frac{dc}{dt} = k_2 C^2 \tag{8}$$

Similarly, by integrating the equation under the two boundary conditions the second-order rate constant (k_2), as well as $t_{1/2}$ can be obtained. The second-order $t_{1/2}$ increase as the initial concentration is decreased.

$$\frac{1}{c} - \frac{1}{c_o} = k_2 t \tag{9}$$

$$t_{\frac{1}{2}} = \frac{1}{k_2 C_o} \tag{10}$$

2.10. Advanced Oxidation Process (AOP)

Catalysts are generally used to speed up chemical reactions; photocatalysts are utilized to speed up chemical reactions in the presence of ultra-violet (UV) and visible lights. The photocatalytic system is characterized by sufficient bandgap, stability, adequate morphology, high surface area, and reusability. There are two types of photocatalytic reactions, i.e., homogeneous and heterogeneous photocatalytic reactions. The photocatalytic reagents are largely used to degrade or mineralize hazardous materials into CO_2 and H_2O, deactivate and destruction of microorganisms, decomposition of air pollutants, and degradation of waste plastics. The MONPs and their composite materials are well known for their photocatalytic behavior in the presence of UV radiation. The photocatalysis on the surface of MONPs is mediated by valence and conduction bands. The valence and conduction bands are regarded as holes and electrons [24]. The degradation of photocatalytic dyes depends on the adsorption of dyes on the surface of the photocatalyst and the separation of photo-generated charges. When exposed to light irradiation, electrons, and holes are photochemically generated at the surface of the photocatalyst. These photogenerated electrons transfer from the valence band (VB) of the photocatalyst to its conduction band

(CB), creating a positively charged hole (h^+) in the VB. The photocatalyst helps reduce the recombination of the photogenerated holes (h^+) and electrons (e^-) by stimulating electrons at higher energy levels. The oxidation and reduction reaction takes place on the photocatalyst surface, and molecular oxygen is reduced to superoxide radical $^{\bullet}O_2^-$ (free radical) by exciting electrons. The hydroxyl ion is oxidized to OH free radical through a hole generated after the excitation of an electron. Holes and electrons, primary active species, undergo redox reactions and convert O_2 and water/OH ions to $^{\bullet}OH/^{\bullet}O_2^-$ secondary active species/ free radicals and degrade into nontoxic free radicals (Figure 4). Photogenerated electrons transfer to the valence and conduction bands. Reductive processes cause these electrons to react with molecular oxygen, yielding the less toxic superoxide anion radical ($^{\bullet}O_2^-$). Oxidative processes cause holes in the valence band to attract electrons from hydroxyl ions or water, forming highly reactive hydroxyl radicals ($^{\bullet}OH$).

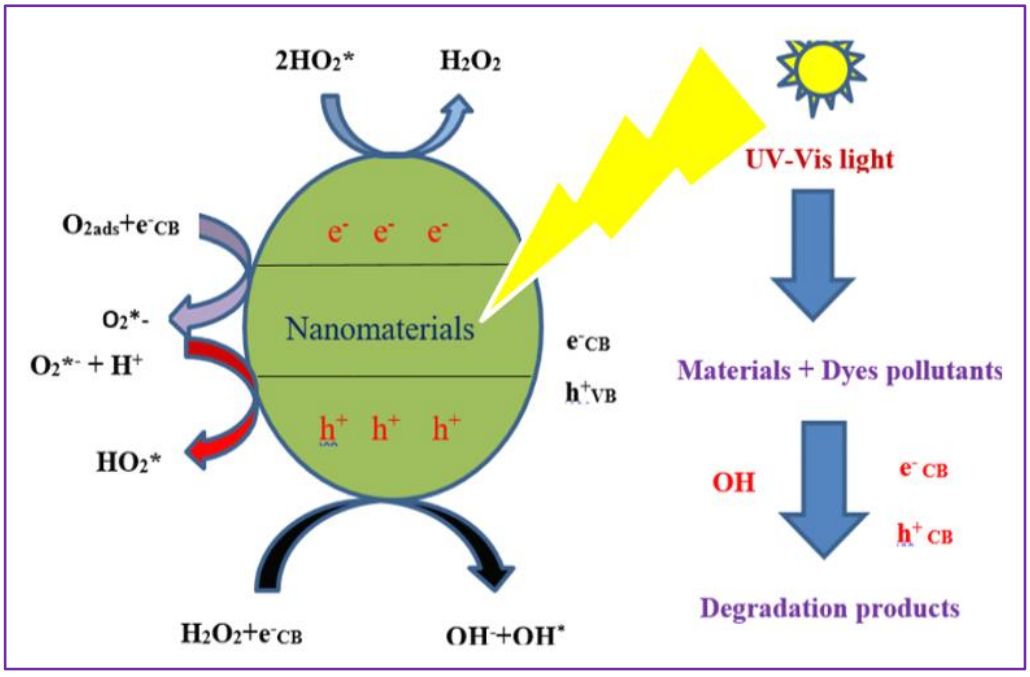

Figure 4: Schematic illustration of the dye degradation mechanism

The mechanistic detail is described in below equations (11)–(20).

$$\text{Photocatalyst} + h\upsilon\ (\geq Eg) \rightarrow \text{Photocatalyst}\ (e^-_{CB} + h^+_{VB}) \quad (11)$$

$$OH^-_{ads} + h^+_{VB} \rightarrow OH^{\bullet} \quad (12)$$

$$O_{2\ ads} + e^-_{CB} \rightarrow O_2{}^{\bullet}- \quad (13)$$

$$O_2{}^*- + H^+ \rightarrow HO_2{}^{\cdot} \quad (14)$$

$$2HO_2^{\bullet}. \rightarrow H_2O_2 + O_2 \quad (15)$$

$$H_2O_2 + e^-_{CB} \rightarrow OH^- + OH^{\bullet} \quad (16)$$

$$H_2O + h^+_{VB} \rightarrow OH^{\bullet} + H^+ \quad (17)$$

$$\text{Dye} + OH^{\bullet} \rightarrow \text{dye decolorization} \quad (18)$$

$$\text{Dye} + h^+_{VB} \rightarrow \text{dye oxidation} \quad (19)$$

$$\text{Dye} + e^-_{CB} \rightarrow \text{dye reduction} \quad (20)$$

The $^{\bullet}OH$ and $^{\bullet}O_2$ were enhanced under visible light. A visible light photon can be absorbed by metal nanoparticles during irradiation. The electron is transferred to the semiconductor through the Scorttky barrier, and the space charge layer may transport the excited electron from the surface of the metal to the bulk of the semiconductor. The electron could also be transferred to molecular oxygen from the surface of the catalyst to generate superoxide ($^{\bullet}O_2^-$) and induce the degradation of a dye. Similarly, holes located on the metal nanoparticles could also combine with H_2O molecules, adsorbed on the surface of the catalyst, to obtain $^{\bullet}OH$ radicals. These radicals can also introduce the degradation in the dye [70].

CHAPTER THREE

3. MATERIALS AND METHODS

3.1. Chemicals and Reagents

The following analytical grade reagents were used directly as obtained, without any further treatment throughout the work: Iron (II) chloride tetrahydrate ($FeCl_2 \cdot 4H_2O$, 98.0%, FARDIBAD, INDIA) and iron (III) chloride hexahydrate ($FeCl_3 \cdot 6H_2O$, 99.0%, FARDIBAD, INDIA) were employed as metal ion precursors for the synthesis of iron oxide (Fe_3O_4) NPs. Cobalt (II) nitrate hexahydrate ($Co(NO_3)_2 \cdot 6H_2O$, ≥99.0% purity from Sigma Aldrich, Darmstadt, Germany) was used as a metal ion precursor for the synthesis of cobalt oxide (Co_3O_4) NPs. Congo red, ($C_{32}H_{22}N_6Na_2O_6S_2$) (SAMIRTECH-CHEM, LTD) an ionic, and Malachite green, ($C_{23}H_{25}ClN_2$) (from Sigma-Aldrich), cationic dyes were chosen as organic pollutants. Ethanol (CH_3CH_2OH) (98% ± 1%, Ranchem industry, Turkey) was used to wash the samples of nanomaterials during recycling, while sodium hydroxide (NaOH) (99.9%, Ranchem industry, Turkey) was employed to adjust the pH of the samples. Distilled water was used to prepare all necessary solutions and washing purposes throughout the experiment.

3.2. Instrument and Apparatus

An electric grinder (National) was utilized to powder the *B. spectabilis* flower samples. The mass of the flower samples and all chemical reagents was measured using a digital electronic balance (Sartorius AG, Germany) with a loading capacity of 160 g. A muffle furnace (INSIF, India, Ho) was used for the calcination of the biosynthesized Fe_3O_4 NPs, Co_3O_4 NPs, and Fe_3O_4/Co_3O_4 NCs. Centrifugation was performed using a centrifuge (PLC. 02, Taiwan), while a pH meter (Bante 902p, Shanghai, China) was used for pH adjustment. Samples were filtered with Whatman No. 1 filter paper (made in India). A magnetic stirrer hot plate (INSIF, H-359) was used for stirring and measuring the required temperature of the metal ion precursor and plant extract. To preserve the biosynthesized nanomaterials and *B. spectabilis* flower extract for subsequent analysis, a desiccator (Bo MEX, USA) and a refrigerant (Standard Laboratory, Thermo Fisher Scientific Inc., USA) were utilized. A UV-Vis spectrophotometer (SM-1600 Spectrophotometer) was used for absorbance measurement. Common laboratory apparatus and equipment were used for multiple purposes.

3.3. Preparation of *Bougainvillea spectabilis* Flower Extract

A matured and healthy *B. spectabilis* flowers were collected from Hawassa University Garden, Sidama, Regional State which was approximately 275 km from Addis Ababa, the capital city of Ethiopia. The preparation of fresh *B. spectabilis* flowers were thoroughly cleaned or washed with running tap water to remove dust particles and other contaminants, followed by distilled water. The flowers were shade-dried at room temperature to remove residual moisture. The dried flowers were ground into a fine powder using a mechanical grinder, followed by packing in airtight glassware. The extraction was carried out by placing 10 g of *B. spectabilis* flower powder in a 250 ml Erlenmeyer flask containing 100 ml of distilled water and boiling at 60 °C for 20 min until the color changed. Then, the extract was cooled to room temperature and filtered using Whatman No.1 filter paper, as shown in Figure 5. Finally, the extract was stored in a refrigerator at 4 °C to be used for further experiments [71].

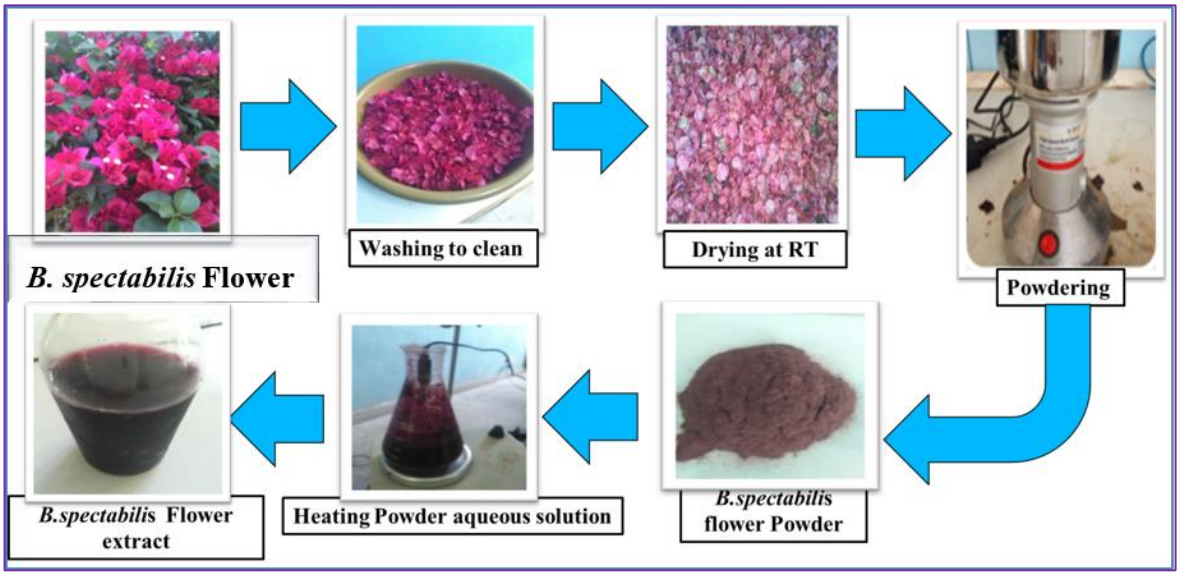

Figure 5: Flow chart for the preparation of *B. spectabilis* flower extract

3.4. Biosynthesis of Iron Oxide (Fe_3O_4), Cobalt Oxide (Co_3O_4) NPs and Fe_3O_4/Co_3O_4 Nanocomposites

3.4.1. Biosynthesis of Fe_3O_4 NPs

Fe_3O_4 NPs was synthesized with some modifications as follows. Briefly, 0.2 M of $FeCl_3.6H_2O$ and 0.1 M of $FeCl_2.4H_2O$ in a 2:1 ratio were measured and dissolved with 200 ml of distilled water placed in a 500 ml beaker. Then, 20 ml of *B. spectabilis* flower aqueous

extract as a reducing agent was added to the solution. It was mixed by magnetic stirring for 10 min. Subsequently, 1.0 M of NaOH was added dropwise to the solution under continuous stirring. NaOH (1.0 M) as a precipitator was slowly added to reach the pH of the solution to 11 followed by vigorous stirring for 30 min. The solution was placed into the oven at 160 °C for 4 h. Finally, the black precipitate was obtained and it was washed twice with distilled water and then dried in the oven at 80 °C for 24 h and calcinated 2 h at 450 °C, and ground finely as shown in Figure 6 [72]. The relevant chemical reaction (Eq. 21) can be expressed as follows:

$$Fe^{2+} + 2Fe^{3+} + 8OH^- \rightarrow Fe_3O_4 + 4H_2O \quad (21)$$

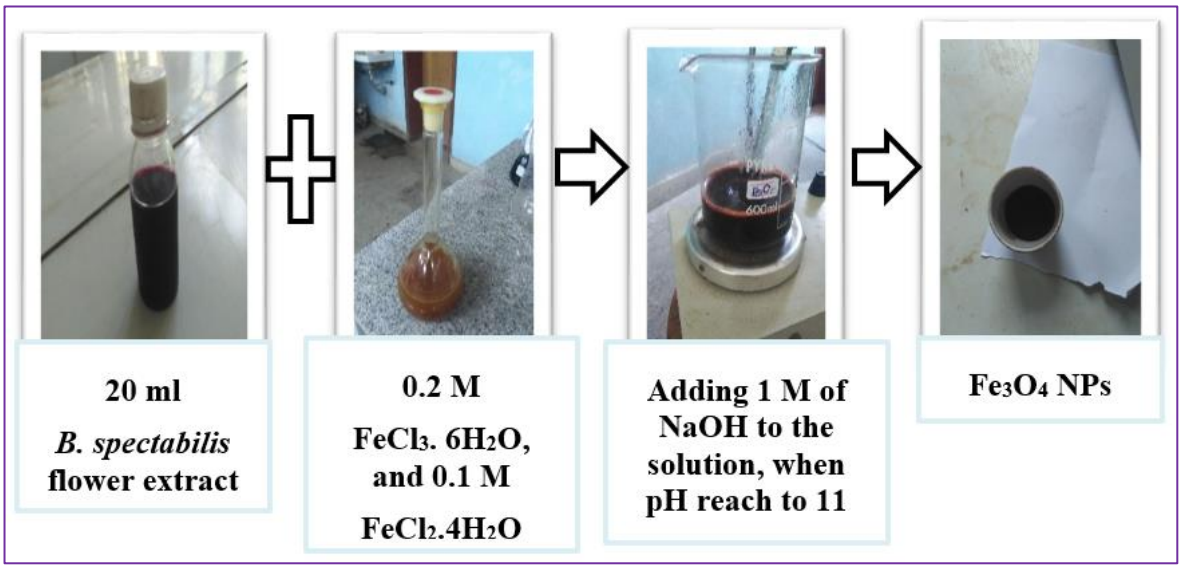

Figure 6: Flow diagram of the synthesis of Fe_3O_4 NPs

3.4.2. Biosynthesis of Co_3O_4 NPs

Co_3O_4 NPs were synthesized with some modifications as follows. A 0.2 M of $Co(NO_3)_2 \cdot 6H_2O$ was measured and dissolved with 200 ml of distilled water placed in a 500 ml beaker. Then, 20 ml of *B. spectabilis* flower aqueous extract was added to the beaker and thoroughly mixed using a magnetic stirrer. Next, 1.0 M of NaOH was carefully added drop by drop under stirring to the solution at a pH equal to 12 for 30 min at 25 °C. Upon mixing, the solution turned from pink to a red-brown color. The stirring was continued for another 2 hours at 80 °C. Then, after natural cooling to room temperature, the formed precipitates were collected by centrifugation, washed with distilled water, and dried at room temperature. Finally, calcinated 2 h at 450 °C a dark brown colored powder was obtained, and the particles

were stored in an air-tight container for further characterization and photocatalytic analysis, as shown in Figure 7 [73].

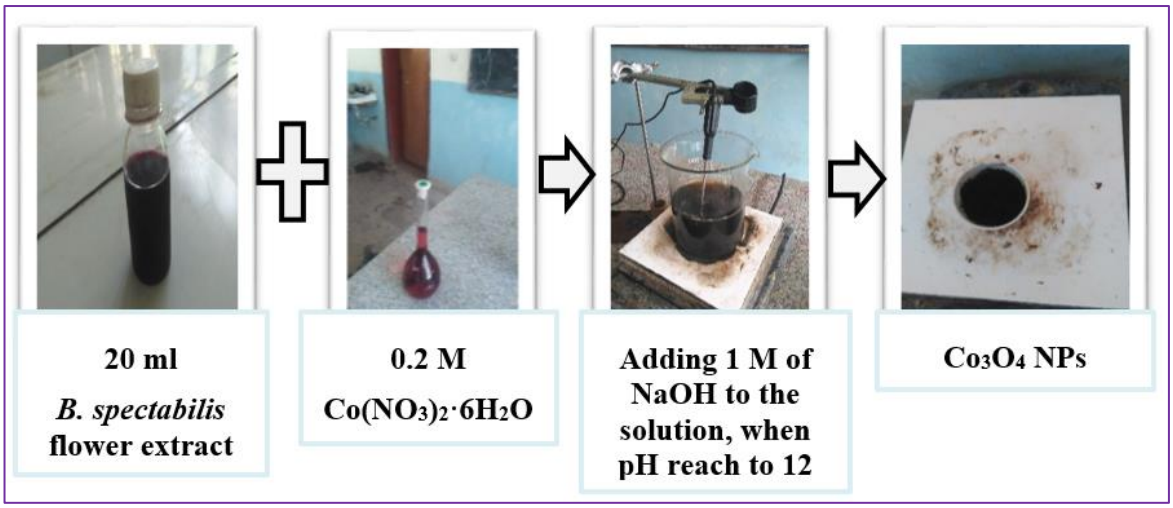

Figure 7: Flow diagram of the synthesis of Co_3O_4 NPs

3.4.3. Biosynthesis of Fe_3O_4/Co_3O_4 NCs

The Fe_3O_4/Co_3O_4 NCs was synthesized using a green method, which involved a straightforward co-precipitation process with some modifications as follows; in the presence of a reducing agent *B.spectabilis* flower aqueous extract. During the experimental procedure, 0.2 M of $FeCl_3.6H_2O$, and 0.1 M of $FeCl_2.4H_2O$ precursors in a 2:1 ratio were measured and dissolved with 200 ml of distilled water placed in one 500 ml beaker, and 0.2 M of $Co(NO_3)_2{\cdot}6H_2O$ was measured and dissolved with 200 ml of distilled water placed in another 500 ml of beaker. Subsequently, the two solutions were combined in an equal volume 1:1 ratio of 200 ml placed in a single beaker and stirred with a magnetic stirrer for a duration of 1 h to ensure thorough mixing. Throughout this process, the temperature was maintained at 90 °C. Next, a volume of 40 ml of *B. spectabilis* flower aqueous extract was added to the solution, followed by continuous stirring for a duration of 2 h, ensuring the temperature remained constant. A 1.0 M of NaOH solution was added to this reaction mixture to achieve a pH of 12. The color of the solution changed from pink to reddish brown, indicating the formation of the Fe_3O_4/Co_3O_4 NCs. The solution was placed into the oven at 160 °C for 4 h. Finally, the black precipitate was obtained and it was washed twice to remove impurities with distilled water and ethanol. Finally, the precipitate was dried in the oven at 80 °C for 24 h, and calcinated 2 h at 450 °C, and ground finely. As Figure 8 shows a schematic illustration of the preparation of Fe_3O_4/Co_3O_4 NCs [74].

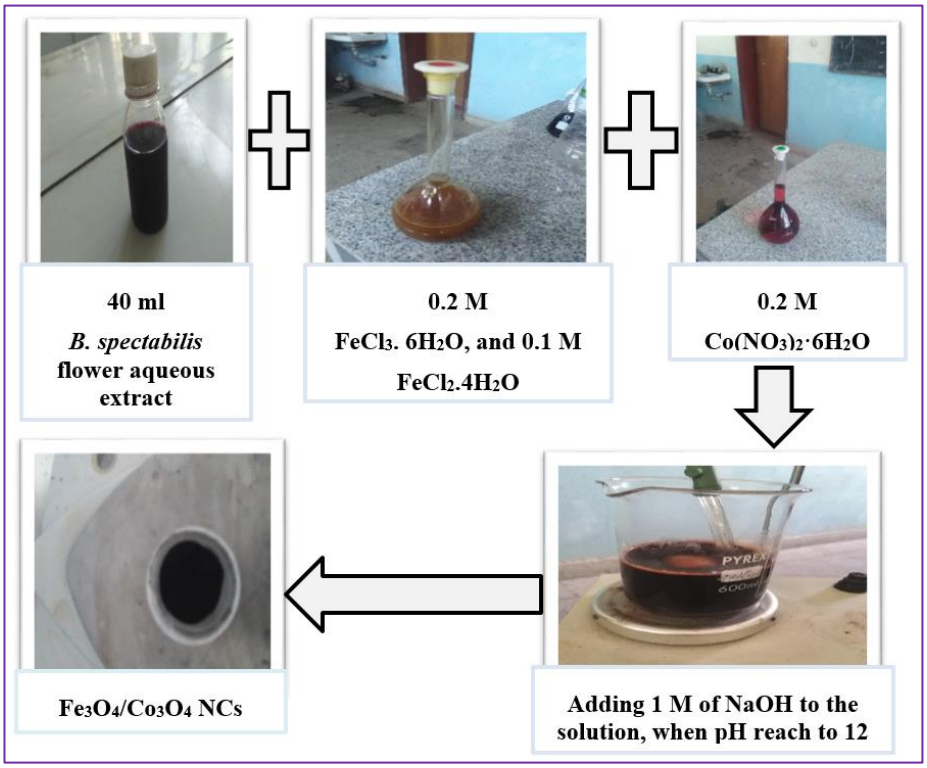

Figure 8: Flow diagram of the synthesis of Fe_3O_4/Co_3O_4 NCs

3.5. Characterizations of Nanoparticles and Nanocomposites

The optical properties of the synthesized Fe_3O_4, Co_3O_4 NPs, and Fe_3O_4/Co_3O_4 NCs, were investigated using UV-Vis diffuse reflectance spectroscopy with a T80 UV/VIS spectrophotometer (PG Instrument Ltd). This analysis was conducted in the wavelength range of 200-800 nm at the Central Laboratory of Sciences, Hawassa University. The functional groups and metal-oxygen bond present on the surface of the synthesized NPs were characterized using Fourier Transform Infrared Spectroscopy (FT-IR) at Central Laboratory of sciences, Hawassa University, with a Perkin Elmer FT-IR BX spectrophotometer, scanning spectra in the range of 4000 cm^{-1} to 400 cm^{-1}. The biosynthesized samples were mixed with solid KBr pellets uniformly and properly, which were compressed to settle down on a thin transparent film. The thin transparent film was used for FT-IR analyses, which were kept in the chamber of the instrument for scanning. The morphological structure and generating particle size distribution of the Fe_3O_4, Co_3O_4 NPs, and Fe_3O_4/Co_3O_4 NCs were analyzed through Scanning electron microscopy (SEM) images obtained at the Laboratory of Applied Biology, Adama Science and Technology University. The particle size distribution was calculated using J software based on the SEM images. The crystalline

structure, phase purity, and size of the synthesized Fe_3O_4 NPs, Co_3O_4 NPs, and Fe_3O_4/Co_3O_4 NCs were determined through X-ray diffraction analysis (XRD-7000, Shimadzu Corporation, Japan) was conducted at the Laboratory of Material Sciences at Adama Science and Technology University. The patterns were obtained using Cu-filtered CuKα radiation (λ = 1.5406 Å) as the X-ray source, energized at a voltage of 40 kV and a current of 30 mA. The sample measurements were taken over a 2θ range of 10° to 80° at room temperature.

3.6. Photocatalytic Degradation of Congo red and Malachite green Dyes

The photocatalytic activity of biosynthesized Fe_3O_4, Co_3O_4 NPs, and Fe_3O_4/Co_3O_4 NCs was studied by degradation of CR and MG in the presence of sunlight irradiations. To evaluate the effectiveness of the Fe_3O_4, Co_3O_4 NPs, and Fe_3O_4/Co_3O_4 NCs, an optimized amount of the synthesized nanoparticle was added into beakers containing initial concentration 20 ppm, 0.09g/25 ml of prepared CR and initial concentration 15 ppm, 0.06g/25 ml of MG aqueous solutions separately. Before sunlight irradiation, a beaker containing the mixture of NPs and dye solution was magnetically stirred or shaken by a shaker for 30 minutes in the dark with magnetic stirring. This is to maintain equilibrium between the adsorption and desorption process between dye molecules and nanoparticles surface. A control was also prepared without the addition of nanoparticles. Then, after 30 minutes, a beaker containing the dye solutions with nanoparticles was placed under exposure to sunlight irradiation within time with the highest light intensity from 11:00 AM - 3:00 PM. At certain time intervals, the dye solution with nanoparticles in the beaker was centrifuged using Centrifuge at 1400 rpm for 5 minutes. Centrifugation is to separate nanoparticles from degraded dye solution by preventing the dispersion of nanoparticles. The extent of the degradation was recorded by measuring the absorbance using a UV-Vis spectrophotometer before and after degradation at 497 and 618 nm for CR and MG respectively.

3.6.1. Photocatalyst dosage

For the optimization of photocatalyst doses from 0.01 gm to 0.15 gm with a range of 0.03 gm were taken per 25 ml of 20 ppm CR and 15 ppm of MG at a constant value of the other parameter. Then the photocatalytic degradation efficiency was calculated by using (Eq. 22).

The degradation percent of the dye solution was calculated by taking the absorbance values recorded at λmax of 497 nm and 618 nm for CR and MG respectively before and after photocatalytic degradation. The equation was provided as shown:-

$$Degradation\ percentage = \frac{C_o - C_t}{C_o} * 100 \ \ or \ \ \frac{A_o - A_t}{A_o} * 100 \quad (22)$$

Where: C_o, A_o is the initial concentration and absorbance of dye solution before exposure to sunlight and C_t, A_t Concentration and absorbance of dye solution respectively, at different time intervals.

3.6.2. Initial concentration of the dye

To investigate the effect of the initial concentration of dyes on photocatalytic degradation efficiency, different initial concentrations were used for both dyes (5, 10, 15, 20, 25, and 30 ppm for CR and MG), while keeping other parameters constant.

3.6.3. Exposure time

For the investigation of the total reaction time required for the total degradation of the Congo red and Malachite green, six trials were taken by intervals of 30-minute gap from 11:00 AM to 3:00 PM. The other parameters optimized before, catalyst dose, and initial concentration of the dyes were applied.

3.6.4. pH of dyes

To study the effects of pH, on the degradation of CR and MG dyes, the other parameters optimized were kept constant and the pH was varied from pH 2 to pH 12 and the optimum pH was investigated.

3.7. Instrumental Calibration

The standard stock solutions of dyes were used to calibrate the instrument for the experiment. To calibrate the instrument, 1000 ppm stock solutions of each dye were prepared, and an intermediate standard solution containing 100 ppm was placed in a 500 ml volumetric flask. The intermediate standards were further diluted with distilled water to obtain six working standards for each dye. Calibration of the instrument was essential to determine the linearity of the instrument's response and to calculate the remaining concentration of the dyes after degradation to investigate the kinetics of the degradation experiment.

3.8. Kinetics Study

In this investigation, all measurements were carried out under optimized experimental conditions. Calibration curves were constructed for both CR and MG dyes to calculate their concentrations after degradation at different time intervals. A constant concentration (initial

concentration with high degradation efficiency) was prepared for both dyes, and the extent of degradation was studied within 15-minute intervals. The concentration of the dye was then calculated by applying the Beer-Lambert law.

$$A = \varepsilon bC \tag{23}$$

Where, A - Absorbance, ε - Molar absorptivity constant, b - Path length, and C – Concentration

This equation is related to $y = mX+b$ and from absorbance versus concentration data slope (m) was calculated and used to calculate the concentration after degradation. Finally, pseudo-zero order, pseudo-first order, and pseudo-second-order kinetics were investigated according to equations 3, 6, and 9 mentioned in the literature review section.

3.9. Study on Catalyst Reusability

The reusability of the biosynthesized Fe_3O_4 NPs, Co_3O_4 NPs, and Fe_3O_4/Co_3O_4 NCs was investigated in the degradation process under identical experimental conditions, including the optimum photocatalyst dosage, concentration of the CR and MG solution, exposure time, and pH. After the completion of the reaction, the photocatalyst was separated from the reaction mixture by centrifugation, washed with distilled water, dried, and then reused for four consecutive cycles.

CHAPTER FOUR

4. RESULTS AND DISCUSSION

4.1. Characterization of Synthesized Nanoparticles and Nanocomposites

4.1.1. Ultraviolet-Visible (UV-Vis) Spectroscopy Analysis

The UV-Vis absorption spectra of the biosynthesized Fe_3O_4 NPs, Co_3O_4 NPs, and Fe_3O_4/Co_3O_4 NCs, were scanned over a wavelength range of 200–800 nm, as shown in Figure 9. UV-Vis spectroscopy is a vital technique for identifying nanoparticle formation through the detection of surface plasmon resonance (SPR) peaks, while also facilitating the estimation of their band gap energy. The presence of absorption peaks at 409 nm, 391 nm, and 422 nm within the SPR region of the UV-Vis spectrum confirms the successful synthesis of Fe_3O_4, Co_3O_4 NPs, and Fe_3O_4/Co_3O_4 NCs, respectively [75, 76], indicating their characterization as nanoscale entities. The UV-Vis absorption spectra of Fe_3O_4, Co_3O_4 NPs, and Fe_3O_4/Co_3O_4 NCs exhibit a broad absorption band in the ultraviolet and visible regions, which can be attributed to their narrow bandgap energy.

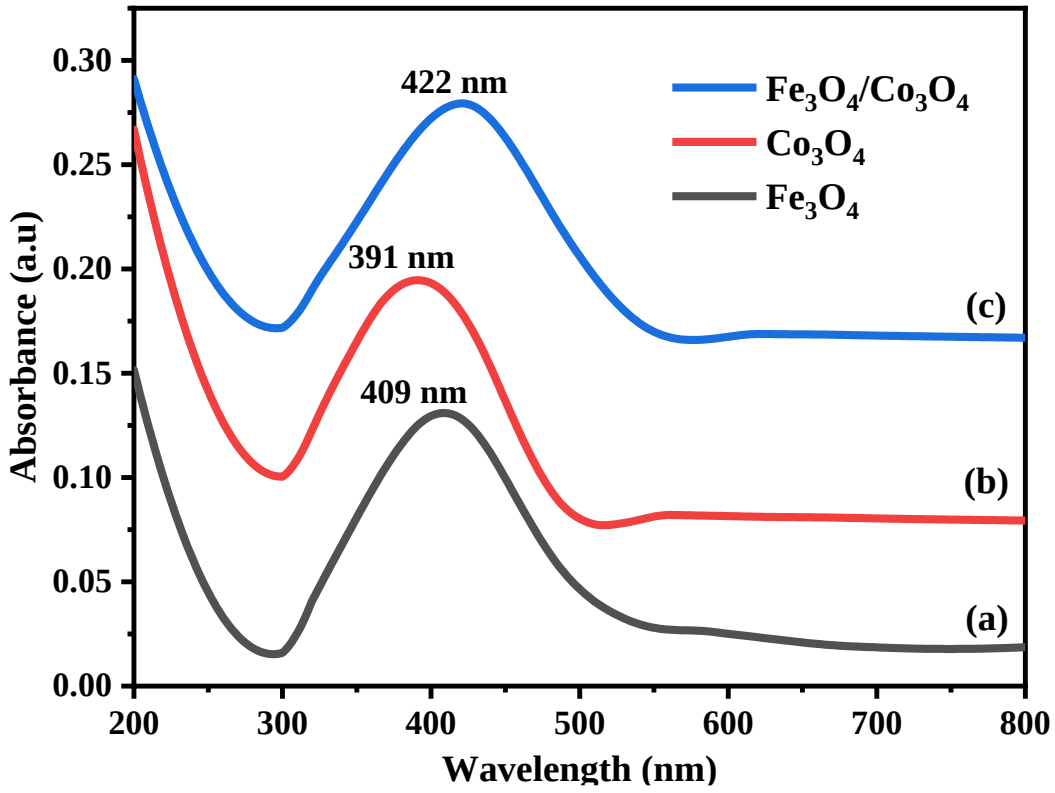

Figure 9: UV-Vis spectra of biosynthesized pure Fe_3O_4 NPs (a), Co_3O_4 NPs (b), and Fe_3O_4/Co_3O_4 NCs (c)

The bandgap energy of the Fe_3O_4, Co_3O_4 NPs, and Fe_3O_4/Co_3O_4 NCs were determined using the Tauc model [77]. The bandgap energy was determined based on the numerical derivative of the optical absorption coefficient using 'Tauc's relation.

$$(\alpha h\nu)^n = A(h\nu - E_g) \quad (24)$$

Where A is the constant, hν for photon energy, E_g for bandgap, α for absorption coefficient, and n = 2 for direct and n =1/2 for indirect allowed transition in these cases n = 2 for the determination of optical bandgap of Fe_3O_4, Co_3O_4 NPs and Fe_3O_4/Co_3O_4 NCs. The bandgap energy (E_g) of the materials can be calculated by using Eq.25.

$$E_g(eV) = 1240/\lambda\ (nm) \quad (25)$$

Where E_g is bandgap energy in electron volt, λ is the wavelength (nm) corresponding to the absorption edge. The bandgap was determined from the $(\alpha h\nu)^2$ Vs hν curve by drawing an extrapolation of the data point to the photon energy axis where $(\alpha h\nu)^2 = 0$, giving the optical bandgap (E_g) as shown in Figure 10 (a, b, and c). Insertion of the slope of $(\alpha h\nu)^2$ Vs hν curve provides bandgap energy of the sample. The optical bandgap (E_g) values were determined by extrapolating the linear portion of the plots of $(\alpha h\nu)^2$ vs. hν to α = 0, as illustrated in Figure 10.

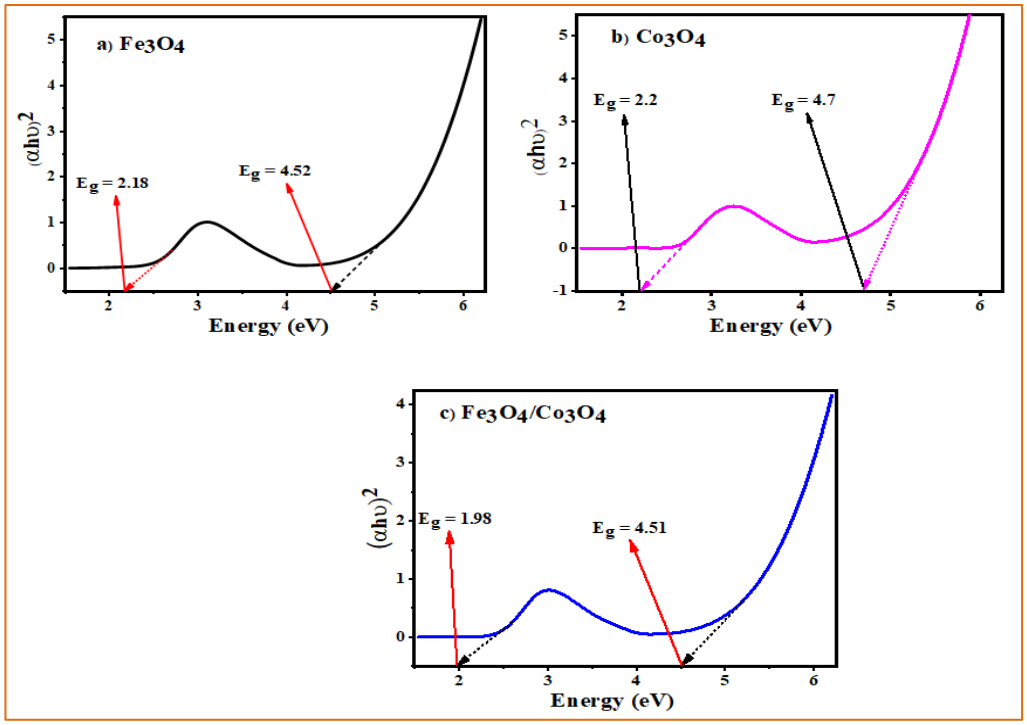

Figure 10: Tauc's plot bandgap energy of biosynthesized Fe_3O_4 NPs (a), Co_3O_4 NPs (b) and Fe_3O_4/Co_3O_4 NCs (c)

The determined bandgap energy results of Fe_3O_4, Co_3O_4 NPs, and Fe_3O_4/Co_3O_4 NCs by using Tauc's plot are shown in Table 1.

Table 1: The optical band gap energies of biosynthesized Fe_3O_4, Co_3O_4 NPs, and Fe_3O_4/Co_3O_4 NCs

Sample	E_{g1} (eV)	E_{g2} (eV)
Fe_3O_4 NPs	2.18	4.52
Co_3O_4 NPs	2.2	4.7
Fe_3O_4/Co_3O_4 NCs	1.98	4.51

The results indicate that the bandgap energy (E_g) values of Fe_3O_4/Co_3O_4 NCs are reduced compared to those of Fe_3O_4 and Co_3O_4 NPs. This reduction can be attributed to changes in particle size associated with the surface modification by Co_3O_4 NPs. This phenomenon is related to the direct bandgap mechanism arising from electron transitions between the valence band (VB) and the conduction band (CB). The Fe_3O_4/Co_3O_4 NCs, formed through the heterojunction between Co_3O_4 and Fe_3O_4, demonstrate an absorption band spanning from 350 to 500 nm, which significantly enhances their capacity for visible light absorption.

The presence of Co_3O_4 NPs on the surface of Fe_3O_4 NPs mitigates light energy dissipation caused by intense light scattering resulting from interactions between incident light and Co_3O_4 NPs. The UV-Vis analysis reveals a minor redshift in the absorption spectrum of Fe_3O_4/Co_3O_4 NCs compared to pure Fe_3O_4 NPs and Co_3O_4 NPs. This redshift suggests that Fe_3O_4/Co_3O_4 NCs possess enhanced energy absorption capabilities, making them more suitable for a variety of photocatalytic applications. The observed alteration in bandgap energy within the Fe_3O_4/Co_3O_4 NCs further agrees with the effective deposition of Co_3O_4 NPs onto the surface of Fe_3O_4 NPs. This phenomenon can be attributed to significant electron-electron interactions within the d-orbital of cobalt (Co), as well as its interactions with the s- and p-orbitals of iron (II, III) oxide (Fe_3O_4). The renormalization effect observed in pure Fe_3O_4 is a consequence of the exchange of sp-d band electrons between Fe_3O_4 and the localized d-electrons of Co^{2+}. This observation provides additional evidence supporting the substantial potential of Fe_3O_4/Co_3O_4 NCs in photocatalytic applications, particularly due to their effective utilization of sunlight. Figure 9 illustrates the respective bandgap values of

2.18 eV, 2.20 eV, and 1.98 eV for Fe_3O_4, Co_3O_4 NPs, and Fe_3O_4/Co_3O_4 NCs, respectively. The findings indicate that the incorporation of Co_3O_4 NPs onto Fe_3O_4 NPs resulted in a shift in the bandgap of Fe_3O_4 from 2.20 eV to 2.18 eV. This transition can be attributed to the presence of oxygen vacancies, which enhance electron mobility from the valence band (VB) to the conduction band (CB) with increased efficiency [74].

4.1.2. Fourier Transform Infrared Spectroscopy (FT-IR) Analysis

FT-IR analysis was conducted to identify the functional groups associated with the biomolecules and metal-oxygen bonds involved in the biosynthesis of Fe_3O_4, Co_3O_4 NPs, and Fe_3O_4/Co_3O_4 NCs. The spectra were recorded within the wavenumber range of 4000–400 cm^{-1}, as illustrated in Figure 11. This spectroscopic technique provides valuable insights into the interactions between phytochemicals present in plant extracts and metal ions that facilitate the production and stabilization of biosynthesized nanoparticles. The individual band intensities observed in the *B.spectabilis* extracts and their corresponding nanoparticles confirm these interactions.

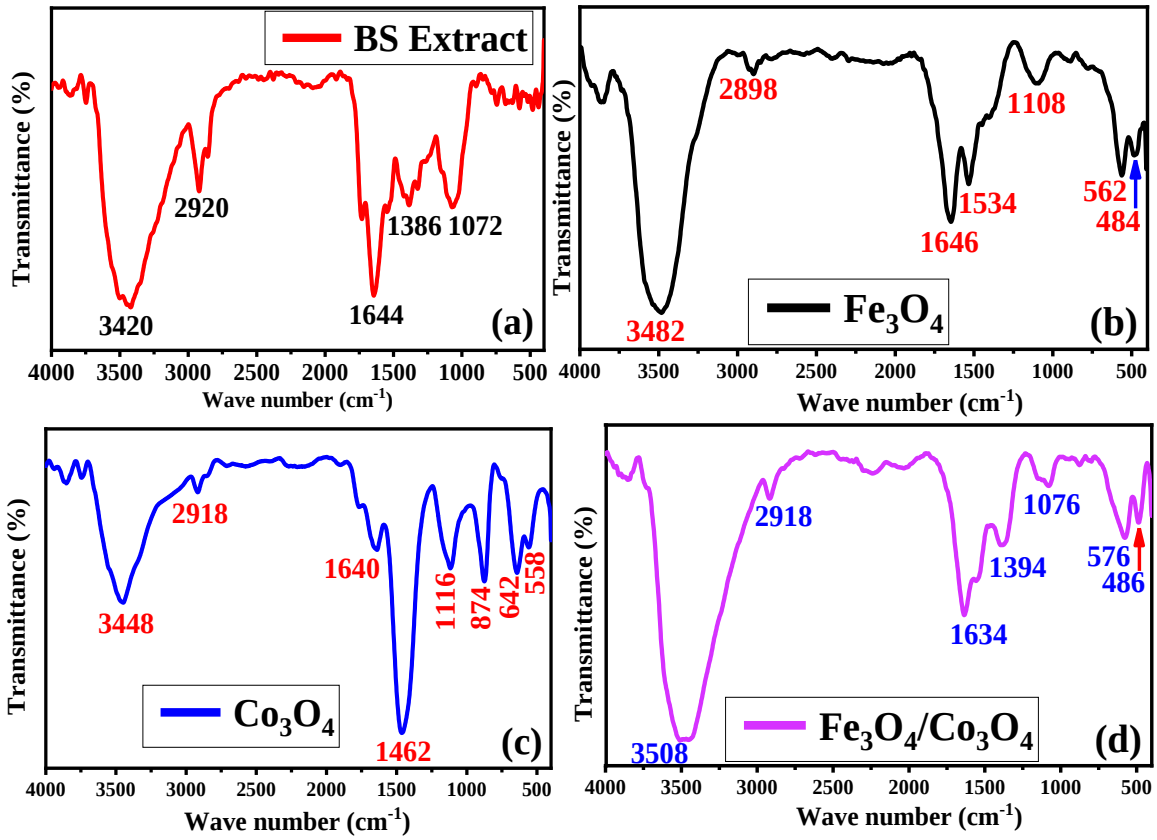

Figure 11: FT-IR spectra of the *B. Spectabilis* flower extract (a), Fe_3O_4 NPs (b), Co_3O_4 NPs (c) and Fe_3O_4/Co_3O_4 NCs (d)

The FT-IR spectrum of the *B.spectabilis* flower extract (Figure 11a) reveals bands at 3420 cm^{-1} (O-H stretching vibrations of polyphenols), 2920 cm^{-1} (C–H and CH_2 vibrations of aliphatic hydrocarbons), 1644 cm^{-1} (C-O stretching of carbonyl groups), 1386 cm^{-1} (C-O bond bending), and 1072 cm^{-1} (C-O stretching, possibly from esters or ethers). Analysis of these spectra strongly suggests the presence of flavonoids and phenols, which serve as natural capping and reducing agents for the biosynthesis of Fe_3O_4, Co_3O_4 NPs, and Fe_3O_4/Co_3O_4 NCs from the aqueous flower extract of *B. spectabilis* [71].

The FT-IR spectrum of Fe_3O_4 is shown in Figure 11b. The absorption bands at 3482 cm^{-1}, 2898 cm^{-1}, and 1646 cm^{-1} correspond to O-H stretching vibrations of water molecules adsorbed on the nanoparticle surface, symmetric and asymmetric vibrations of methyl groups, and C-O stretching vibrations of carbonyl groups, respectively. The peak at 484 cm^{-1} for Fe_3O_4 NPs is attributed to the characteristic stretching vibrations of the Fe-O bond in the spinel iron oxide crystal phase, confirming the successful biosynthesis of these Fe-O nanoparticles, consistent with previous literature [26].

The FT-IR spectrum of Co_3O_4 NPs is displayed in Figure 11c. Major bands at 3448 cm^{-1} can be attributed to O-H stretching vibrations of water molecules adsorbed on the nanoparticle surface, 2918 cm^{-1} symmetric and asymmetric vibrations of methyl groups, 1640 cm^{-1} stretching vibrations of carbonyl groups (C-O), 1462 cm^{-1} C–N functional groups, and 1116 cm^{-1}, 874 cm^{-1} aromatic C–H bending bands, respectively. Notably, two strong bands at 642 cm^{-1} and 558 cm^{-1} correspond to vibration modes (υ) of Co–O bonds, indicating the formation of Co_3O_4 spinel oxide [40, 76].

The FT-IR spectrum of Fe_3O_4/Co_3O_4 is presented in Figure 11d. The characteristic absorptions for the Fe-O and Co–O bond at 486 cm^{-1} suggest successful hybridization between Co_3O_4 and Fe_3O_4, confirming the formation of nanocomposites. Notably, the transmittance of Fe_3O_4/Co_3O_4 NCs is higher than that of bare Fe_3O_4 NPs due to reduced nanoparticle aggregation [26, 78]. Overall, the observed shifts in all bands indicate the interactions between nanoparticles and *B. spectabilis* flower extract, highlighting intrinsic stretching vibrations of metals at tetrahedral sites as well as metal-to-metal interactions during the formation of Fe_3O_4/Co_3O_4 NCs [79].

4.1.3. Scanning Electron Microscope (SEM) Analysis

The surface morphologies, particle sizes, and distributions of the biosynthesized Fe_3O_4 NPs and Co_3O_4 NPs, as well as the Fe_3O_4/Co_3O_4 NCs, were investigated using scanning electron microscopy (SEM) and J software at a magnification of 20 µm, as illustrated in Figures 12(a-c). Figure 12(a) presents the SEM topography of the biosynthesized Fe_3O_4 NPs, which display a smooth surface with non-uniform, rough, and closely packed irregular granular structures. The average particle size of the Fe_3O_4 NPs was determined to be approximately 1949 nm. Figure 12(b) illustrates the SEM topography of the biosynthesized Co_3O_4 NPs, which exhibit a sponge-like morphology characterized by numerous irregular pores and voids; the average particle size of the Co_3O_4 NPs was found to be approximately 1437 nm. Figure 12(c) shows the SEM images of the Fe_3O_4/Co_3O_4 NCs at a magnification of 20 µm. Based on SEM observations and nanoparticle size distribution tests conducted using J software, the average diameter of the NCs was approximately 1622 nm. These SEM results indicate successful surface functionalization of the Fe_3O_4 NPs with Co_3O_4 NPs. Notably, a moderate degree of particle agglomeration was observed as smooth and uniform morphology, which can be attributed to the high surface area, leading to the formation of medium-sized particles.

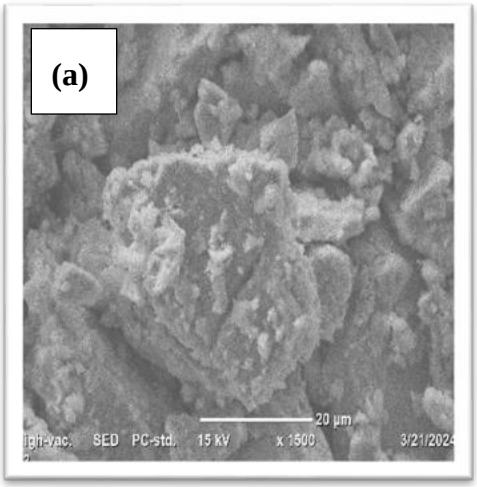

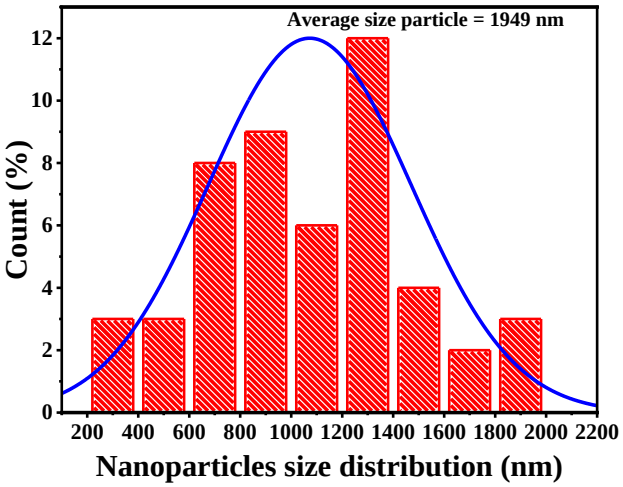

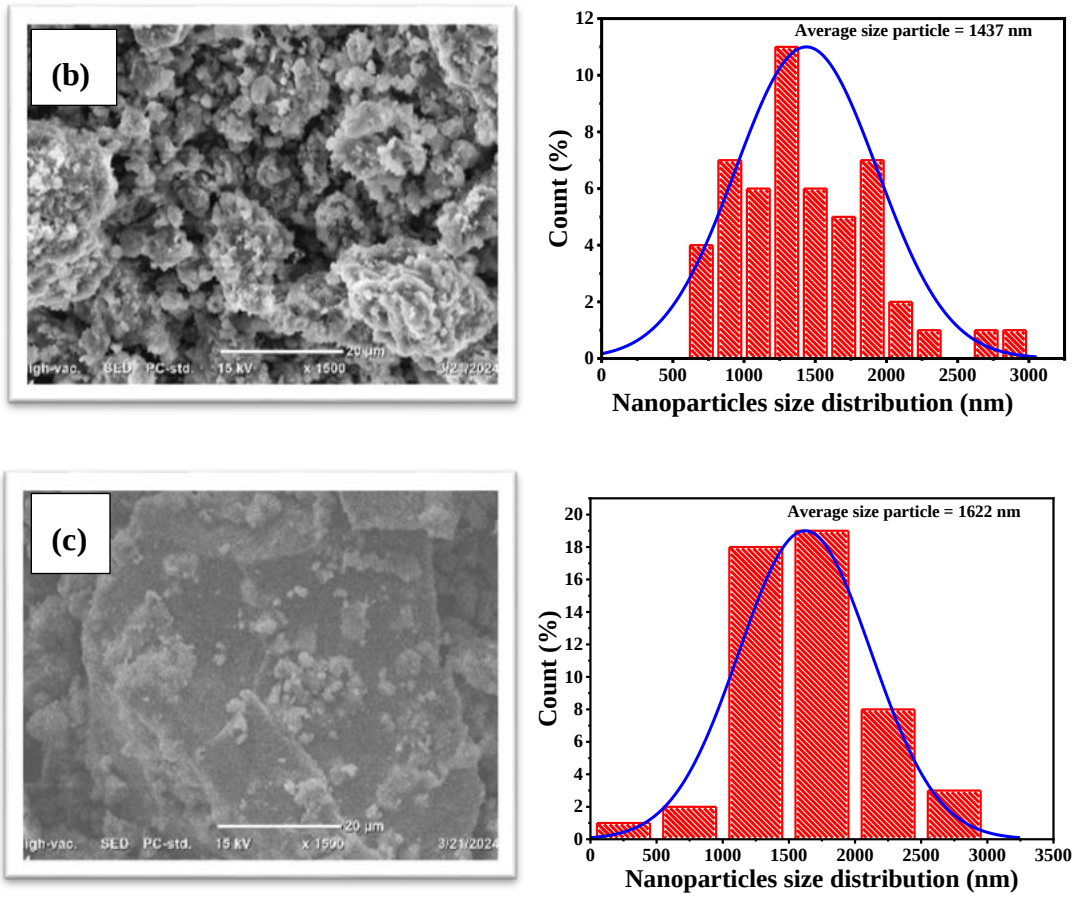

Figure 12: SEM images and histogram of particle size distribution analysis for the Fe_3O_4 NPs (a), Co_3O_4 NPs (b), and Fe_3O_4/Co_3O_4 NCs (c)

The observed porosity and voids are attributed to the combustion process during the synthesis of the photocatalyst. These features may enhance light absorption through increased light reflection and expand the contact area between the particles and pollutants, thereby resulting in higher photocatalytic efficiency [80].

4.1.4. X-Ray Diffraction (XRD) Analysis

The crystallographic information of pure Fe_3O_4, Co_3O_4 NPs, and Fe_3O_4/Co_3O_4 NCs was obtained through X-ray diffraction (XRD) analysis, with the combined diffraction peaks illustrated in Figure 13.

The diffraction peaks of the synthesized Fe_3O_4 NPs (Figure 13a) were detected at 2θ values of 30.56°, 35.86°, 43.46°, 54.01°, 57.38°, 63.00°, and 74.46°, corresponding to the (220), (311), (400), (422), (511), (440), and (533) planes of spinel Fe_3O_4 (JCPDS: 19–0629) [81]. The presence of sharp and intense peaks indicates a high degree of crystallinity in the iron oxide phase.

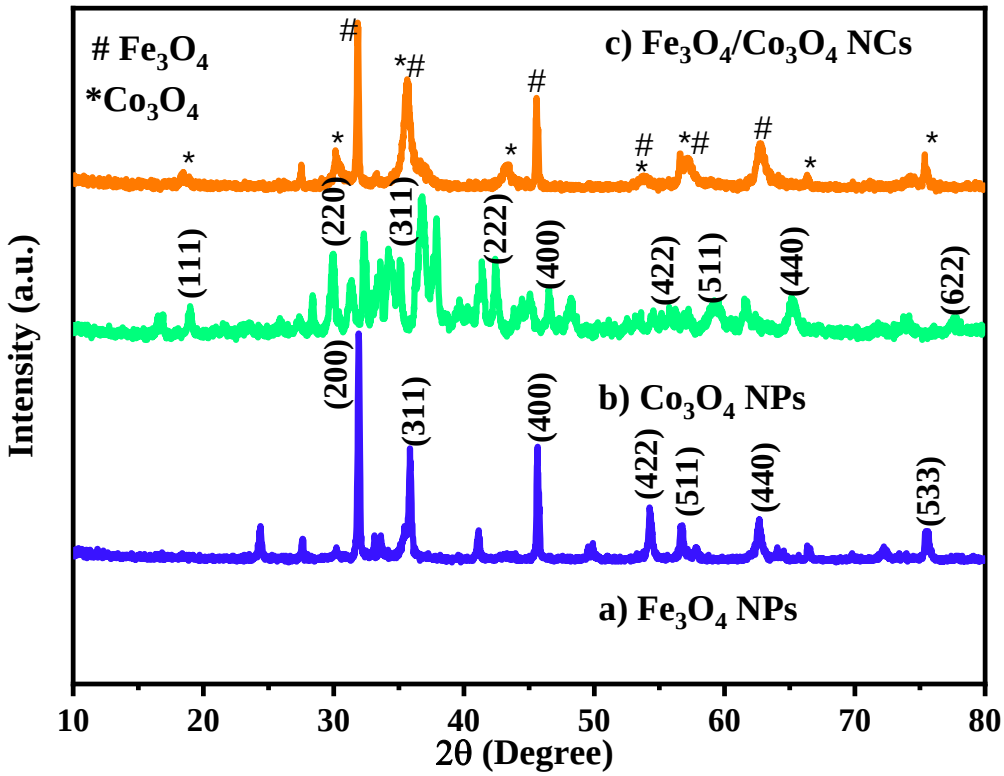

Figure 13: XRD patterns for Fe_3O_4 NPs (a), Co_3O_4 NPs (b) and Fe_3O_4/Co_3O_4 NCs (c)

In the XRD pattern of Co_3O_4 NPs (Figure 13b), eight sharp peaks were observed, which correspond to the cubic spinel structure of cobalt oxide, located at 2θ values of 19.95°, 31.27°, 36.79°, 44.66°, 55.67°, 59.28°, 65.26°, and 77.65°. These peaks are indexed to the (111), (220), (311), (400), (222), (511), (440), and (622) planes of the cubic crystal system, belonging to the Fd-3m space group of spinel cobalt oxide, as per JCPDS No. 00-042-1467 [73].

The XRD patterns of the Fe_3O_4/Co_3O_4 NCs in Figure 13c exhibit multiple diffraction peaks that coincide well with the spinel structures of both Fe_3O_4 and Co_3O_4 [40], confirming the successful synthesis of the nanocomposite via the *B. spectabilis* flower extract-assisted method. Although the crystal phases of Fe_3O_4 retained their positions, their intensities were weaker than those of Co_3O_4 due to the shielding effect of the Co_3O_4 shell. This observation suggests that no significant reactions occurred between Fe_3O_4 and Co_3O_4, as no additional peaks were detected. The estimation of interplanar spacing in the lattice and the crystallite size of the synthesized materials was conducted and tabulated in Table 2 using Bragg's law and the Debye-Scherrer equation, respectively [54]. The relationships are expressed in

Equations (26) and (27) below, which illustrate the correlation between X-ray diffraction peak broadening and crystallite size:

$$n\lambda = 2d \sin\theta, \tag{26}$$

$$D = \frac{k\lambda}{\beta cos\theta} \tag{27}$$

In these equations, n is an integer, λ is the X-ray wavelength for Cu Kα (1.5406 Å), and θ is the angle between the incident ray and the scattering planes. D represents the crystallite size (in nm), k is the Scherrer constant 0.94, which depends on the Miller index of the reflecting plane and the shape of the crystal, and β is the full-width at half maximum (FWHM) of the crystallite peak (measured in radians). The value of β, obtained from the XRD data, was converted to radians using the equation shown below:

$$\beta = \frac{FWHM\ in\ 2\theta \times \pi}{180^\circ} \tag{28}$$

Table 2: X-ray diffraction (XRD) analysis of biosynthesized nanomaterials

Nanocatalysts	Peak No	2θ (°)	d-spacing (nm)	FWHM (°)	Miller indices (hkl)	D (nm)	Average D (nm)
Fe_3O_4 NPs	1	31.93	0.2810	0.1917	200	45.17	31.02
	2	35.86	0.2511	0.3193	311	27.40	
	3	45.67	0.1991	0.2217	400	40.74	
	4	56.71	0.1627	0.3542	511	26.71	
	5	62.66	0.1486	0.4642	440	20.99	
	6	75.54	0.1262	0.4200	533	25.07	

Co_3O_4 NPs	1	29.94	0.1549	0.4666	220	20.59	19.05
	2	32.37	0.1444	0.3912	311	25.20	
	3	34.36	0.1370	1.4673	222	6.87	
	4	36.79	0.1291	0.7708	400	13.49	
	5	37.84	0.1260	0.5386	422	19.58	
	6	48.20	0.1036	0.5544	511	22.53	
	7	59.29	0.0899	1.072	440	15.20	
	8	65.26	0.0851	0.6880	622	28.92	
Fe_3O_4/Co_3O_4 NCs	1	31.85	0.2817	0.19255	220	44.97	24.2
	2	35.65	0.2525	0.82166	311	10.64	
	3	45.60	0.1995	0.22474	400	40.19	
	4	57.06	0.1618	1.12524	422	8.42	
	5	62.80	0.1484	0.84169	511	11.59	
	6	75.43	0.1264	0.35785	622	29.41	

4.2. Evaluation of Photocatalytic Activity

The photocatalytic activity of biosynthesized pure Fe_3O_4 NPs, Co_3O_4 NPs, and Fe_3O_4/Co_3O_4 NCs was evaluated for the degradation of CR and MG. Dye degradation was visually detected by a gradual change in color to a colorless solution. The degradation process supported by Fe_3O_4, Co_3O_4 NPs, and Fe_3O_4/Co_3O_4 NCs was studied by varying parameters like photocatalyst dosage, initial concentration of dyes, exposure time, and pH. Preliminary screening for the occurrence of degradation was done by observing the color disappearing of dye in an aqueous solution and then calculating the presence of degradation from the absorbance values measured before and after degradation.

4.2.1. Effect of photocatalyst dosage

To investigate the effect of catalyst dosage on the degradation of CR and MG dyes were carried out by varying the amount of Fe_3O_4, Co_3O_4 NPs, and Fe_3O_4/Co_3O_4 NCs dose loading from 0.01 to 0.15 gm with a 0.03 gm interval and keeping other reaction parameters constant.

The degradation outlines of aqueous CR (20 ppm) and MG (15 ppm) solution over the different Fe_3O_4, Co_3O_4 NPs, and Fe_3O_4/Co_3O_4 NCs doses presented, as shown in Figure 14.

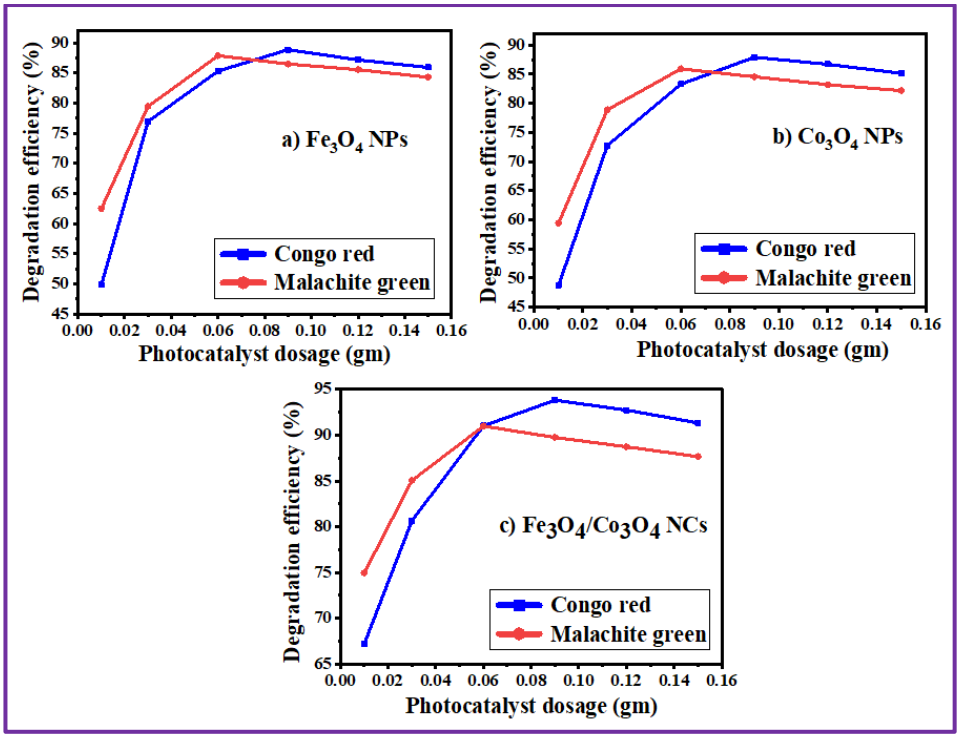

Figure 14: Effect of nano photocatalyst loading on the photocatalytic degradation CR and MG by biosynthesized pure Fe_3O_4 NPs (a), Co_3O_4 NPs (b), and Fe_3O_4/Co_3O_4 NCs (c), with 20 ppm/25 mL for CR and 15 ppm/25 mL for MG

The results displayed in Figure 14 and Appendix 1 show that an increase in the nano photocatalyst loading from 0.01 to 0.09 gm sharply increased the degradation for CR to a maximum of 88.85% for Fe_3O_4 NPs, 87.93% Co_3O_4 NPs and 93.81% Fe_3O_4/Co_3O_4 NCs, and from 0.01 to 0.06 gm sharply increased the degradation for MG to a maximum of 87.84% by Fe_3O_4 NPs, 85.93% Co_3O_4 NPs and 90.98% Fe_3O_4/Co_3O_4 NCs respectively. This enhancement could be attributed to the greater accessibility of hydroxyl and superoxide radicals on the surface of active sites, which resulted from the increased availability of electrons (e^-) and holes (h^+). However, a further increase in the nano photocatalyst loading beyond the optimal point for pure Fe_3O_4 NPs, Co_3O_4 NPs, and Fe_3O_4/Co_3O_4 NCs for the degradation of both CR and MG dyes respectively, resulted in a decrease in the photocatalytic degradation rate. This phenomenon could have been due to factors such as nano photocatalyst aggregation which in turn tends to reduce the number of active sites, hindrance and blocking of light penetration, and low availability of degradation dye caused

by the excessive amount of photocatalyst. This is recognized as the higher accessibility of surface active sites for the adsorption of dye molecules with the increase in Fe_3O_4, Co_3O_4 NPs, and Fe_3O_4/Co_3O_4 NCs dose [5, 60].

4.2.2. Effect of the initial concentration of CR and MG

This investigation was done the impact the initial concentration of six aqueous CR and MG solutions of different concentrations ranging gap of 5 ppm from 5 ppm to 30 ppm with a fixed photocatalyst dosage of 0.09 and 0.06 grams of Fe_3O_4, Co_3O_4 NPs, and Fe_3O_4/Co_3O_4 NCs of both dyes respectively.

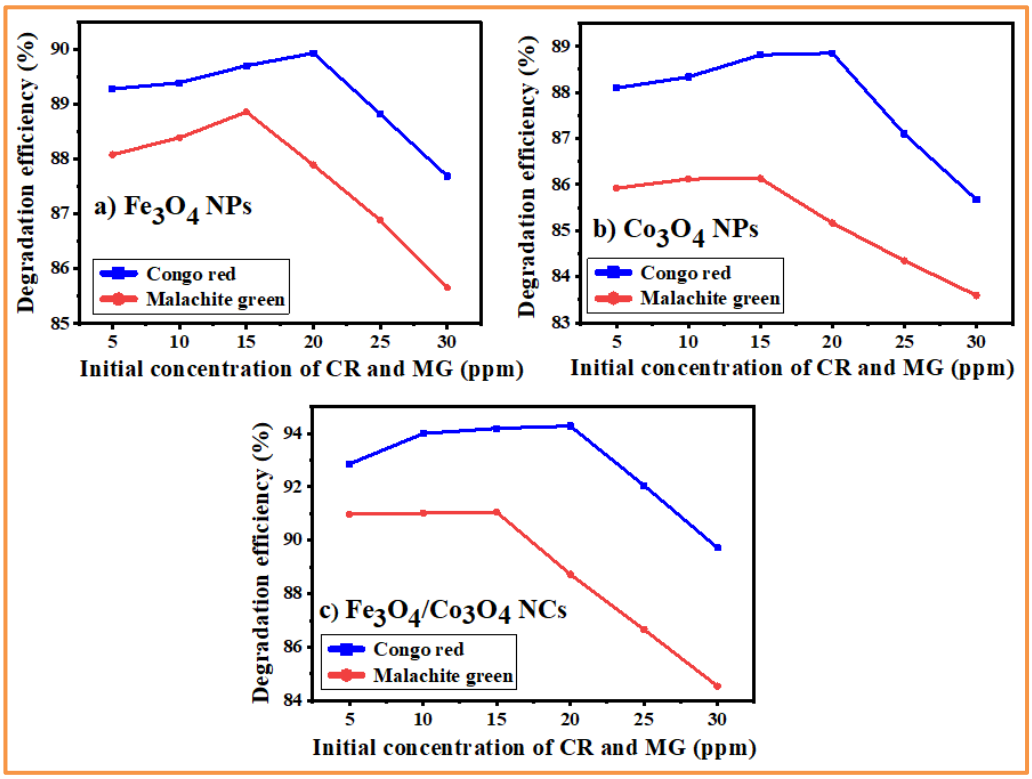

Figure 15: Effect of initial concentration of CR and MG on the photocatalytic degradation by biosynthesized Fe_3O_4 NPs (a), Co_3O_4 NPs (b), and Fe_3O_4/Co_3O_4 NCs (c), photocatalyst dosage: 0.09 gm/25mL for CR and photocatalyst dosage: 0.06 gm /25mL for MG

As shown in Figure 15 and refer to Appendix 2, an initial concentration of CR increased from 5 ppm to 20 ppm, and the photocatalytic degradation shows the maximum efficiencies 89.94% for Fe_3O_4 NPs, 88.85% Co_3O_4 NPs and 94.27% Fe_3O_4/Co_3O_4 NCs, and an initial concentration of MG increased from 5 ppm to 15 ppm, the photocatalytic degradation shows with the maximum efficiencies 88.87% for Fe_3O_4 NPs, 86.13% Co_3O_4 NPs and 91.05%

Fe_3O_4/Co_3O_4 NCs at optimum level, then after these two optimum values of initial concentration of the dyes, the efficiency decreased in minimal differences. This is because the nanoparticles have a large surface area available for adsorption and interaction with photons, resulting in more active sites. However, beyond 20 ppm of CR and 15 ppm of MG, the efficiency was exponentially decreased. This decline can be attributed to the excessive amount of adsorbed CR and MG, which could block active sites and reduce the interaction of light with these active sites for hydroxyl radical generation.

As can be understood, the degradation efficiency increases with an increase in concentration from 5-20 ppm for CR, and the degradation efficiency increases with an increase in concentration from 5-15 ppm for MG. The rate of the degradation decreased with increasing concentration of dye, this decrease in rate is due to the reduction of the electron transfer process on the nanoparticles and nanocomposite photocatalyst surface with organic dyes [1, 59]. Then, after these two optimum values of initial concentrations, the efficiency decreased. The increment in degradation with increasing the initial dye concentration is just because more dyes are available for degradation, and this will be true up to the optimum point. This decrease in degradation efficiency with increasing initial dye concentration above the optimum value is primarily due to a large amount of adsorbed dye, which may also inhibit reactions between dye molecules and reactive radicals. Since the excessive dye concentration may hinder light penetration into the solution, fewer photons can reach the photocatalyst surface [5, 82].

4.2.3. Effect of exposure time

The effect of reaction time on the photocatalytic degradation of CR and MG by biosynthesized Fe_3O_4, Co_3O_4 NPs, and Fe_3O_4/Co_3O_4 NCs was investigated by measuring the degradation efficiency at 15-minute intervals while keeping all other parameters at the optimal points for each nanocatalyst, as discussed earlier.

As shown in Figure 16 and Appendix 3, the photocatalytic degradation for CR increased sharply to 91.80%, 90.87% and 95.20% degradation efficiency as the reaction time increased to 75 min by Fe_3O_4 NPs, Co_3O_4 NPs and Fe_3O_4/Co_3O_4 NCs respectively, and photocatalytic degradation for MG increased up to 90.71%, 89% and 93.03% degradation efficiency as the reaction time increased to 90 min for pure Fe_3O_4 NPs, Co_3O_4 NPs and Fe_3O_4/Co_3O_4 NCs respectively. The effective irradiation time required for the photocatalysts to interact with the available CR and MG led to degradation that was proportional to the availability of active

sites. However, beyond 75 minutes for CR and 90 minutes for MG, further exposure to light did not result in any significant increase in degradation efficiency for any of the samples. This is because at the beginning formation of %OH radicals is faster and the availability of more active sites for pollutants adsorption. After a particular reaction time, the remaining active site is not easy to fill because of the repulsive force between the molecules on the surface with the bulk phase, and thus %degradation tends to be constant after some time. If the time of total degradation of dyes reaches up to the degradation efficiency of the photocatalyst then further exposition time will not be useful, as it cannot bring more results beyond the efficiency of the catalyst [62, 66].

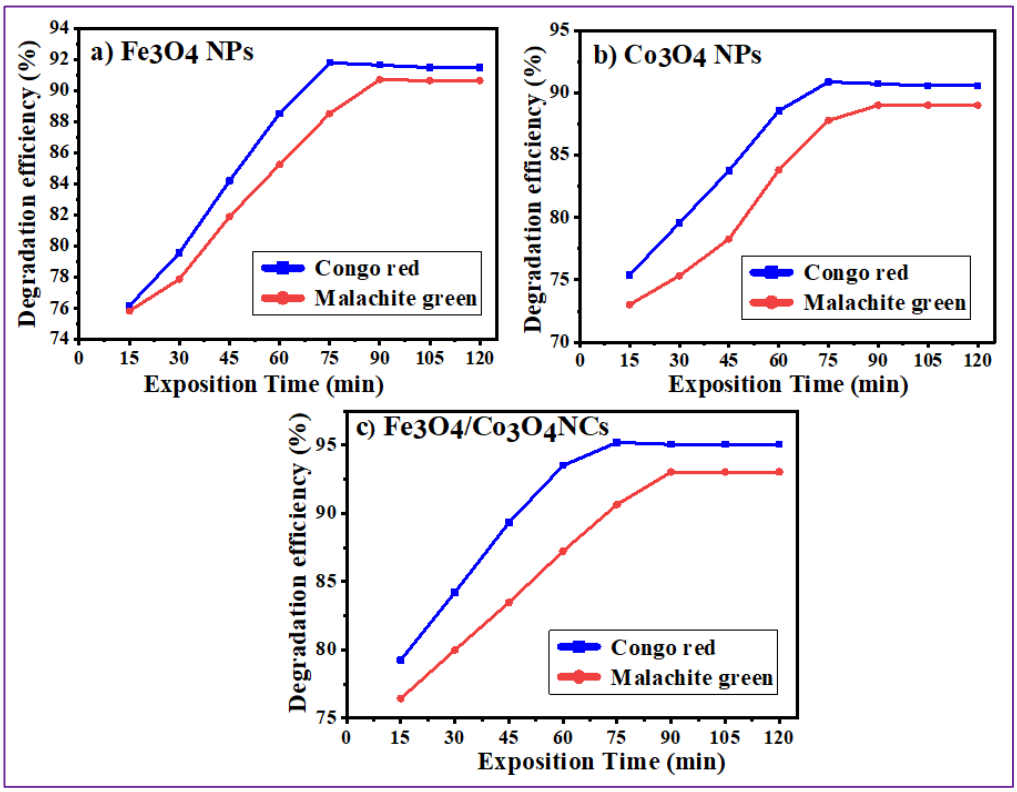

Figure 16: Effect of exposition time on the photocatalytic degradation of CR and MG by biosynthesized Fe_3O_4 NPs (a), Co_3O_4 NPs (b), and Fe_3O_4/Co_3O_4 NCs (c), photocatalyst dosage: 0.09 gm/25 mL, initial concentration 20 ppm for CR and photocatalyst dosage: 0.06 gm/25mL, initial concentration 15 ppm for MG

4.2.4. Effect of the solution pH

The influence of pH on the CR and MG photocatalytic degradation by biosynthesized Fe_3O_4, Co_3O_4 NPs, and Fe_3O_4/Co_3O_4 NCs was studied in the pH range of 2–12 at a constant nano photocatalyst dose (0.09, 0.06) g, initial concentration of CR and MG (20, 15) ppm and

irradiation time (75, 90) min for degradation of CR and MG, respectively. The optimal photocatalytic degradation efficiencies for CR 93.65%, 92.57%, and 96.13% at pH 6 by the Fe_3O_4 NPs, Co_3O_4 NPs, and Fe_3O_4/Co_3O_4 NCs respectively, and the optimal photocatalytic degradation efficiencies for MG 91.39% and 90.57% at pH 10 by the Fe_3O_4 NPs and Co_3O_4 NPs, 94.40% at pH 8 Fe_3O_4/Co_3O_4 NCs, respectively were determined as shown in Figure 17 and Appendix 4 for detailed information. The photocatalytic degradation efficiencies of CR and MG by all the biosynthesized nanocatalysts increased to the optimal pH of the solution and then decreased slightly. This is because the surface of the nano photocatalyst is negatively charged in an alkaline medium (OH^-**)** and positively charged in an acidic medium (H^+). Because CR is an ionic dye, its structure becomes negatively charged when it is dissolved in water, and MG is a cationic dye, its structure becomes positively charged when it is dissolved in water. The degradation process is affected suggestively by pH. As the solution gets more acidic, the H^+ concentration increases, thus, degradation increases [5, 59].

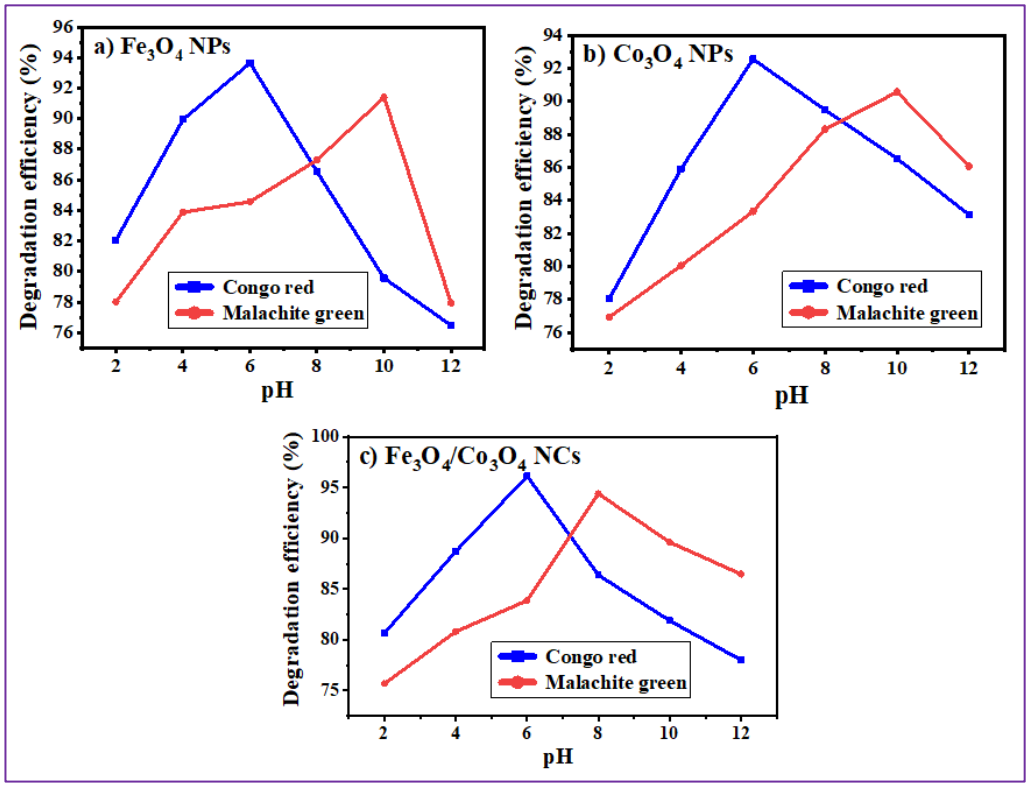

Figure 17: Effect of solution pH on the photocatalytic degradation of CR and MG by biosynthesized Fe_3O_4 NPs (a), Co_3O_4 NPs (b), and Fe_3O_4/Co_3O_4 NCs (c), photocatalyst dosage: 0.09 gm/25mL, Initial concentration; 20 ppm, reaction time 75 min for CR and photocatalyst dosage 0.06 gm/25mL, Initial concentration; 15 ppm and reaction time 90 min for MG

4.3. Kinetics Study

Kinetic models have been exploited to test the experimental data and to determine the mechanism. In the current study, three kinetic models have been established to predict the photocatalytic degradation reaction data of dyes; the pseudo-zero-order, pseudo-first-order, and pseudo-second-order kinetic models. The degradation of the pseudo kinetics experiment was carried out at different reaction time ranges from 15 to 75 min for CR and 15 to 90 min for MG under optimum experimental conditions of biosynthesized nanoparticles. During this work all other experimental parameters optimized were constant. To investigate the pseudo kinetics, calibration curves were constructed as shown in Figure 18, which was aimed at calculating the concentration of the dyes after degradation at a different time interval. Data for the calibration curves of CR and MG can be seen in Appendix 5.

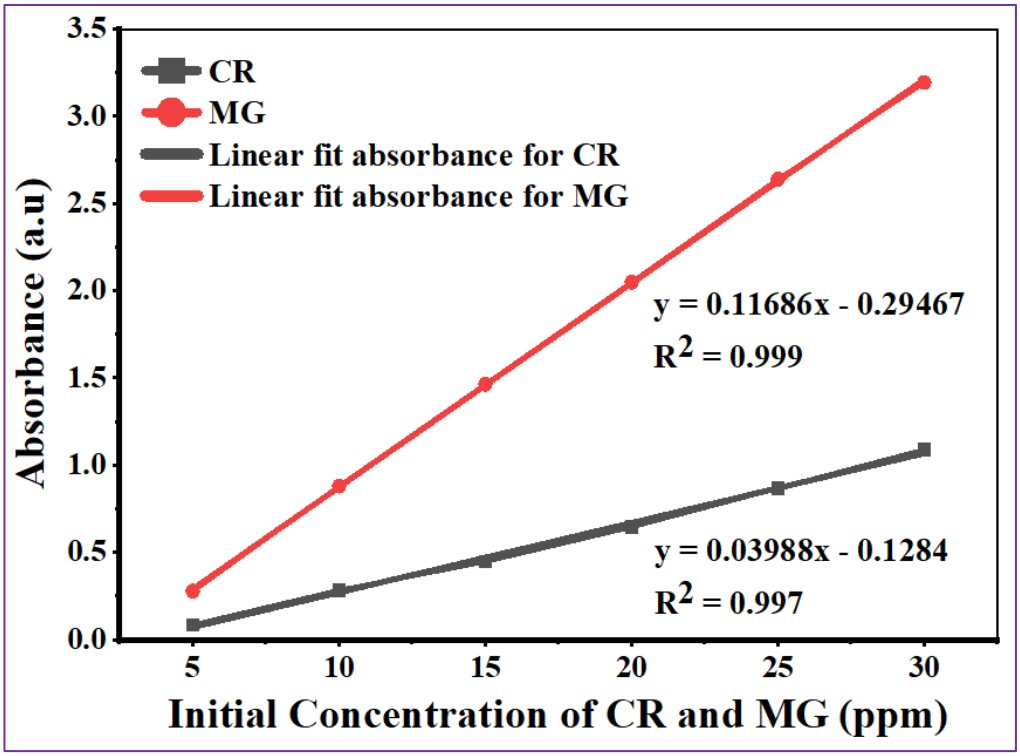

Figure 18: Calibration curves of initial concentration of CR and MG

The pseudo kinetics experiments were conducted and the data was used for calculating the remaining concentration of the dyes with the help of Appendix 5, the final concentration of both CR and MG was calculated using their respective calibration curve, and other quantities were used for investigating the pseudo kinetics were calculated and data collected in Appendix 6. This was done to determine the degradation rate of CR and MG by biosynthesized pure Fe_3O_4 NPs, Co_3O_4 NPs, and Fe_3O_4/Co_3O_4 NCs.

4.3.1. Pseudo-zero-order kinetics

To investigate the degradation kinetics of CR and MG dyes facilitated by biosynthesized Fe_3O_4 NPs, Co_3O_4 NPs, and Fe_3O_4/Co_3O_4 NCs, the linearized pseudo-zero-order kinetics equation is shown in Equation 3. The plot of the pseudo-zero-order kinetics model for both dyes as shown in Figure 19. As stated in Equation 3 and the data presented in Appendix 6 was used to plot the graph as C_O-C_t versus time gives pseudo-zero-order kinetics, where C_O initial concentration before degradation while C_t is the concentration at a time t on the degradation. In this zero order-pseudo kinetics study, a high correlation coefficient close to unity (0.995) for CR degradation by biosynthesized Fe_3O_4 NPs and (0.991, 0.969) for MG degradation by Fe_3O_4 and Co_3O_4 NPs respectively compared to other models, which indicates it, seems to follow pseudo-zero-order kinetics. A pseudo-zero-order reaction is thus, observed for saturation coverage on the surface of the photocatalyst, and the degradation rate is independent of the dye concentration. The pseudo-zero-order rate constant of the photocatalytic degradation was found to be 0.04346 (ppm/min) for CR degradation by Fe_3O_4 NPs and (0.02619, 0.02929) (ppm/min) for MG degradation by Fe_3O_4 and Co_3O_4 NPs respectively, as shown in Table 3.

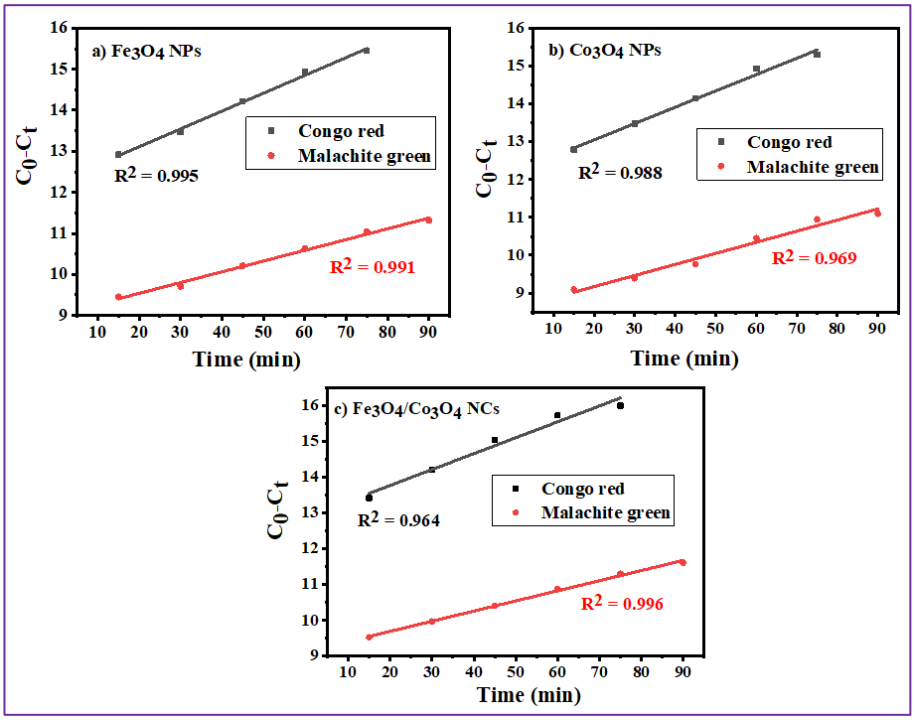

Figure 19: Pseudo zero-order kinetic model for the photocatalytic degradation of CR and MG by biosynthesized pure Fe_3O_4 NPs (a), Co_3O_4 NPs (b), and Fe_3O_4/Co_3O_4 NCs (c) respectively

4.3.2. Pseudo-first-order kinetics

The linearized pseudo-first order equation is shown in equation 6. On the equation, C_O is the initial concentration of the dyes before degradation while C_t is the concentration at time t. The equation is valid by assuming the driving force of degradation is constantly proportional to dye concentration. Figure 20 was the graph constructed for CR and MG dyes in investigating the pseudo-first-order kinetics.

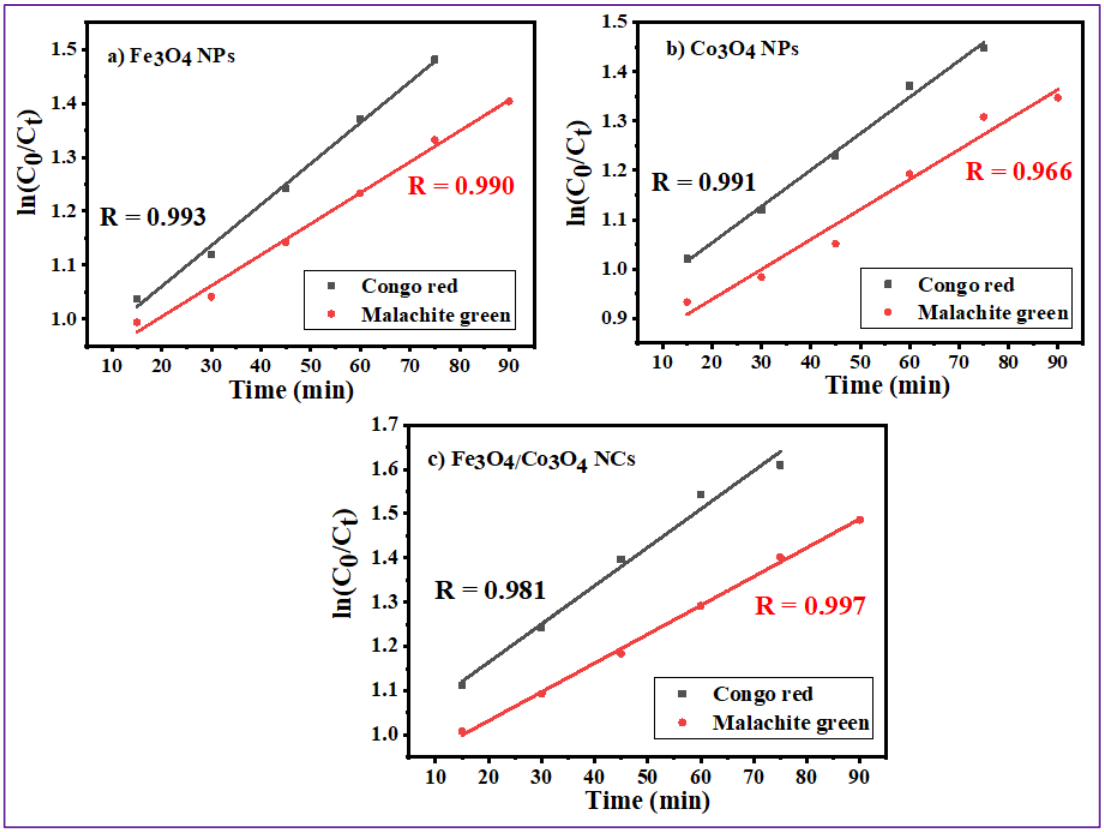

Figure 20: Pseudo-first-order kinetic model for the photocatalytic degradation of CR and MG by biosynthesized Fe_3O_4 NPs (a), Co_3O_4 NPs (b), and Fe_3O_4/Co_3O_4 NCs (c) respectively

The most linear graph with a correlation coefficient (R^2) of (0.991) for CR degradation by biosynthesized Co_3O_4 NPs and (0.997) for MG degradation by Fe_3O_4/Co_3O_4 NCs respectively. The photocatalytic degradation of CR and MG follows the pseudo-first-order on the photocatalyst surface of Co_3O_4 NPs and Fe_3O_4/Co_3O_4 NCs respectively, when compared relatively with other kinetic models. It also indicates the photocatalytic degradation of CR on the surface of Co_3O_4 NPs and degradation of MG on the surface of Fe_3O_4/Co_3O_4 NCs photocatalyst seems to follow pseudo-first-order kinetics i.e. rate of

degradation and concentration of dye is directly proportional [8]. The pseudo-first-order rate constant of the photocatalytic degradation was found to be 0.00738 min^{-1} for CR degradation by pure Co_3O_4 NPs and 0.00652 min^{-1} for MG degradation by Fe_3O_4/Co_3O_4 NCs respectively, as shown in Table 3.

4.3.3. Pseudo-second-order kinetics

Pseudo-second-order kinetics was also investigated for the photocatalytic degradation of CR and MG dyes. The linear graph with a correlation coefficient of (0.988) for CR degradation by biosynthesized Fe_3O_4/Co_3O_4 NCs. The linearized equation for plotting the graph is found in Equation 9. According to Equation 9 and the data presented in Appendix 6 was used to plot the graph as $1/C_t$-$1/C_O$ versus time t displays a pseudo-second-order kinetics. Figure 21 shows a graph of the pseudo-second-order kinetics of both dyes. The pseudo-second-order rate constant of the photocatalytic degradation was found to be 0.00172 min/ppm for CR degradation by biosynthesized Fe_3O_4/Co_3O_4 NCs, as shown in Table (3).

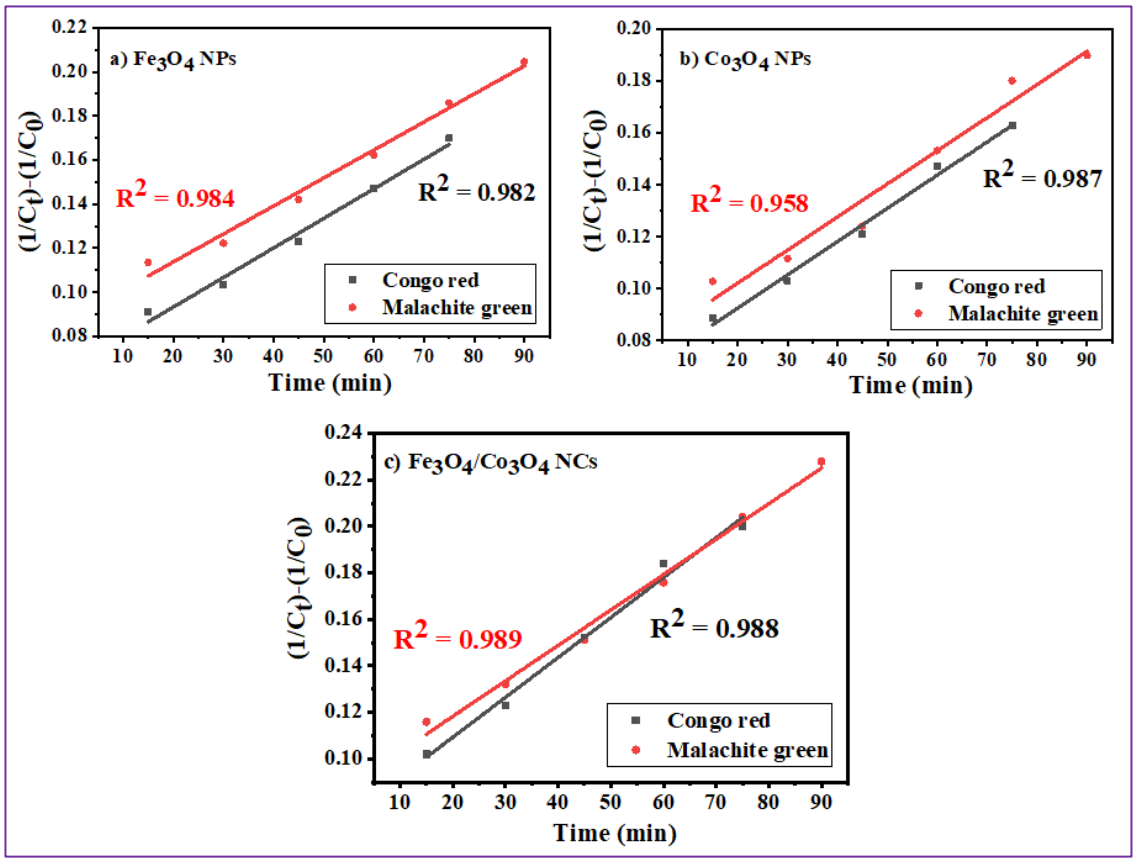

Figure 21: Pseudo-second-order kinetic model for the photocatalytic degradation of CR and MG by biosynthesized Fe_3O_4 NPs (a), Co_3O_4 NPs (b), and Fe_3O_4/Co_3O_4 NCs (c) respectively

Table 3: Rate constant (k) and correlation coefficient (R^2) calculated for the kinetic model for the photocatalytic degradation of CR and MG by biosynthesized Fe_3O_4 NPs, Co_3O_4 NPs, and Fe_3O_4/Co_3O_4 NCs

			Kinetic models		
Photocatalyst	Organic dyes	Parameters	Pseudo 0^{th} order (ppm/min)	Pseudo 1^{st} order (min^{-1})	Pseudo 2^{nd} order (min/ppm)
Fe_3O_4 NPs	CR	k	0.04346	0.00758	0.00134
		R^2	0.995	0.993	0.982
	MG	k	0.02619	0.00574	0.00127
		R^2	0.991	0.991	0.984
Co_3O_4 NPs	CR	k	0.04313	0.00738	0.00128
		R^2	0.988	0.991	0.987
	MG	k	0.02929	0.00608	0.00128
		R^2	0.969	0.966	0.958
Fe_3O_4/Co_3O_4 NCs	CR	k	0.04447	0.00866	0.00172
		R^2	0.964	0.981	0.988
	MG	k	0.02833	0.00652	0.00152
		R^2	0.996	0.997	0.989

4.4. Photocatalytic Degradation Mechanisms

The photocatalytic degradation of CR and MG dye over biosynthesized Fe_3O_4/Co_3O_4 NCs under visible light occurs when sunlight is irradiated on the photocatalyst (Fe_3O_4, Co_3O_4, or Fe_3O_4/Co_3O_4), leading to the generation of electron-hole pairs in conduction/valence bands on the surface of the photocatalyst (equation (29)) shown in Figure 22 [78]. In the conduction

band (CB), atmospheric oxygen on the surface of the photocatalyst combines with the excited electron and forms $^{\bullet}O_2^-$ (superoxide radical; equation (30)), which prevents the recombination of e^-/h^+ pairs by converting them into $^{\bullet}OH$ radicals through hydroperoxyl radicals ($HOO^{\bullet}$) and H_2O_2 intermediates (equation (31)). Simultaneously, holes produced in the valence band (VB) react with surface water to produce hydroxyl radicals ($^{\bullet}OH$; equation (32)). These hydroxyl radicals act as a strong oxidizing agent and degrade CR and MG molecules into simple inorganic molecules, such as water, carbon dioxide, and inorganic ions (equation (33)).

$$\text{Photocatalyst surface} + hv \rightarrow e^-_{CB} + h^+_{VB} \quad (29)$$

$$2e^-_{CB} + 2O_2 \rightarrow 2^{\bullet}O_2^-, \quad (30)$$

$$2^{\bullet}O_2^- + 2H^+ \rightarrow 2HOO^{\bullet} \rightarrow H_2O_2 \rightarrow 2^{\bullet}OH \text{ (oxidizing agent)} \quad (31)$$

$$h^+_{VB} + H_2O \rightarrow H^+ + {}^{\bullet}OH \text{ (oxidizing agent)} \quad (32)$$

$$^{\bullet}OH + \text{CR and MG} \rightarrow \text{Degradation products } (CO_2 + H_2O + \text{Simple inorganic ions}) \quad (33)$$

Fe_3O_4/Co_3O_4 NCs were illuminated under sunlight irradiation which leads to the formation of e^- in the CB and h^+ in the VB. As the photo-generated electrons are transferred to the CB and VB. The electron reacts with molecular oxygen to produce less toxic super oxide anion radical ($^{\bullet}O_2^-$) through a reductive process. The hole in the VB can attract electrons from water or hydroxyl ions to generate the most reactive hydroxyl radical ($^{\bullet}OH$) through an oxidative process. The superoxide anions react with electron-hole pairs and generate H_2O_2. The combination of metal oxide generates more active catalytic centers which facilitate the photodegradation performance [83]. The decrease in dye absorption intensity over time and its eventual disappearance when using Fe_3O_4/Co_3O_4 NCs can be attributed to the breakdown of the heterocyclic conjugated structure of CR and MG molecules into simpler molecules such as water, carbon dioxide, and inorganic ions. Additionally, the photocatalytic efficiency of Fe_3O_4/Co_3O_4 NCs was found to be superior to that of Fe_3O_4 and Co_3O_4 NPs. Fe_3O_4 NPs have a narrow bandgap, leading to rapid recombination of e^-/h^+ pairs under irradiation, thereby limiting the survival time of charge carriers for the photocatalysis process. In contrast, in Fe_3O_4/Co_3O_4 NCs, the energy levels of the CB and VB of Fe_3O_4 differ from those of Co_3O_4 NPs. During irradiation, some photogenerated electrons from Fe_3O_4 NPs are captured by Co_3O_4 NPs at the interface of the composite, where they react with surface oxygen to form superoxide radicals. Simultaneously, some holes transfer to the VB of Co_3O_4

from Fe_3O_4 and react with surface water to produce hydroxyl radicals (˙OH). This phenomenon at the interface prevents electron-hole recombination in Fe_3O_4, leading to an increase in the generation of reactive species at the junction of Fe_3O_4/Co_3O_4. This enhanced generation of reactive species at the heterojunction of the two different semiconductor materials accelerates the degradation of dye molecules. Therefore, the efficient charge transfer separation at the heterojunction of Fe_3O_4/Co_3O_4 NCs is responsible for their enhanced photocatalytic activity in degrading CR and MG solutions [77, 78, and 80].

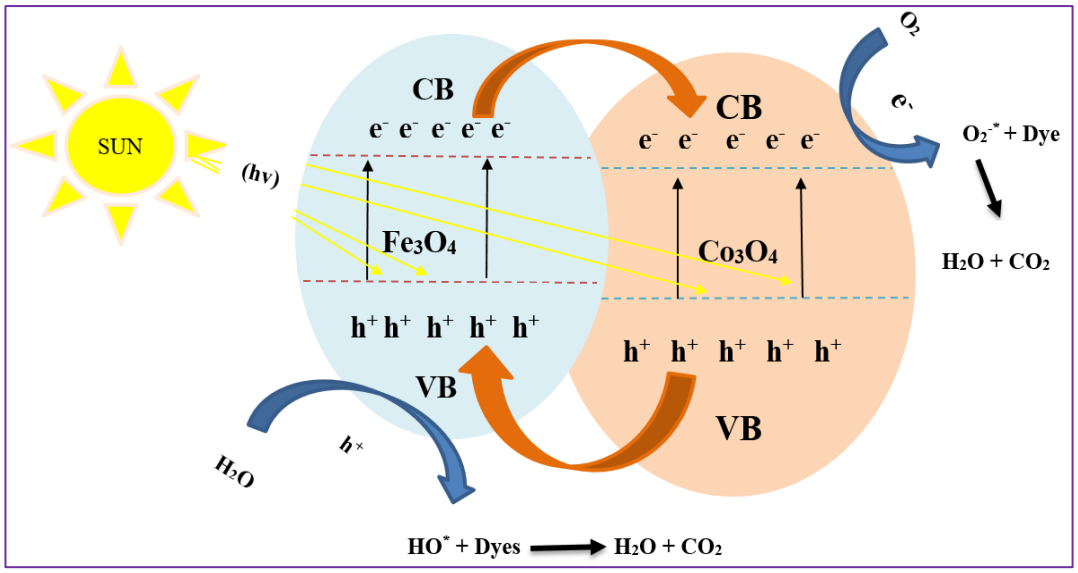

Figure 22: Possible mechanisms of photocatalytic degradation of CR and MG in the presence of sunlight irradiation with *B. spectabilis* flower extract-mediated biosynthesized Fe_3O_4/Co_3O_4 NCs

4.5. Catalyst Reusability Tests

In this study, the recyclability test was conducted to assess the stability and reusability of the biosynthesized NPs and NCs under sunlight conditions. The objective was to evaluate their effectiveness as nanocatalysts in degrading CR and MG dye molecules. The recyclability assessment was performed after demonstrating the effectiveness of the degradation of CR and MG dyes under optimal experimental conditions. All the biosynthesized nanocatalysts were tested over four cycles under solar irradiation. As shown in Figure 23 and Appendix 7, the maximum photocatalytic degradation efficiencies for CR within 75 minutes were 92.88%, 92.12%, and 95.05% for Fe_3O_4 NPs, Co_3O_4 NPs, and Fe_3O_4/Co_3O_4 NCs, respectively. Similarly, the maximum photocatalytic degradation efficiencies for MG within 90 minutes were 90.71%, 90.23%, and 93.92% for Fe_3O_4 NPs, Co_3O_4 NPs, and Fe_3O_4/Co_3O_4

NCs, respectively. The degradation of CR and MG was observed to occur in the presence of sunlight even after four consecutive cycles. The results regarding the reusability of Fe_3O_4 NPs, Co_3O_4 NPs, and Fe_3O_4/Co_3O_4 NCs highlight their potential as photocatalysts for the photodegradation of CR and MG dye molecules. However, it is expected that the efficiency of Fe_3O_4 NPs, Co_3O_4 NPs, and Fe_3O_4/Co_3O_4 NCs as photocatalysts will diminish after four consecutive cycles due to the inevitable loss of the samples during each cycle's collection and centrifugation procedures.

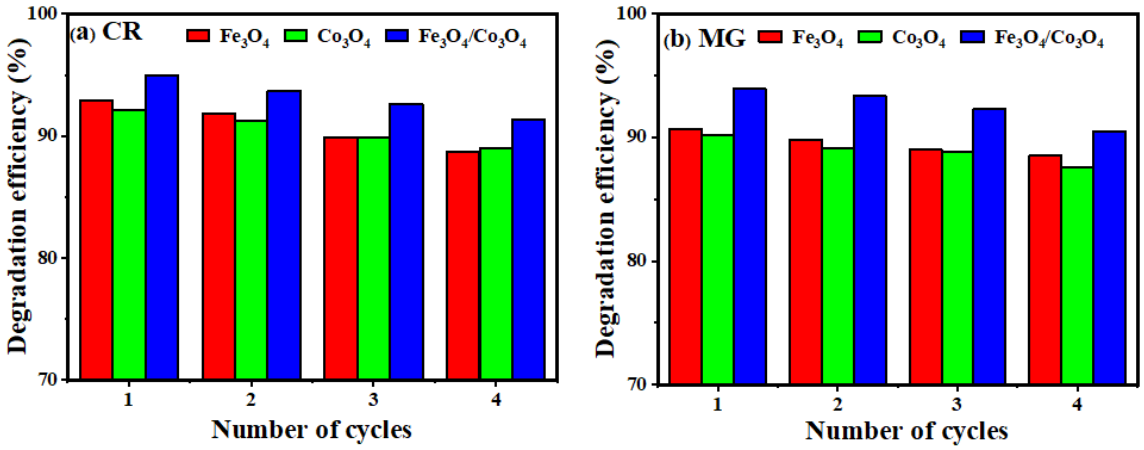

Figure 23**:** Recyclability of pure Fe_3O_4, Co_3O_4 NPs, and Fe_3O_4/Co_3O_4 NCs for the degradation of CR (a) and MG (b)

In general, the findings of this study indicate that the biosynthesized pure Fe_3O_4, Co_3O_4 NPs, and Fe_3O_4/Co_3O_4 NCs exhibit recyclability and can serve as a photocatalyst in the photodegradation of CR and MG molecules [74, 78]. Furthermore, it demonstrates a photocatalytic window that can effectively degrade various CR and MG dye molecules.

CHAPTER FIVE

5. CONCLUSION AND RECOMMENDATION

5.1. Conclusion

In this study, Fe_3O_4, Co_3O_4 NPs, and Fe_3O_4/Co_3O_4 NCs were successfully synthesized using a green method that utilized the flower extract of *B. spectabilis* as a natural reducing and capping agent. The photocatalytic efficiency of the Fe_3O_4/Co_3O_4 NCs was evaluated through sunlight irradiation by investigating the photocatalytic degradation of CR and MG under ambient reaction conditions. Characterization of Fe_3O_4 NPs, Co_3O_4 NPs, and Fe_3O_4/Co_3O_4 NCs was performed using various analytical techniques, including UV-Vis, FT-IR, SEM, and XRD. UV-Visible analysis confirmed the successful synthesis of Fe_3O_4, Co_3O_4 NPs, and Fe_3O_4/Co_3O_4 NCs at the nanoscale via green methods, revealing energy band gaps of 2.18 eV, 2.2 eV, and 1.98 eV, respectively. FT-IR analysis indicated the presence of characteristic peaks corresponding to Fe-O 484 cm^{-1}, and Co-O 558 cm^{-1} bonds. SEM analysis revealed that the biosynthesized Fe_3O_4 NPs, Co_3O_4 NPs, and Fe_3O_4/Co_3O_4 NCs exhibited a smooth surface with non-uniform, rough, and closely packed irregular granular structures. A sponge-like morphology characterized by numerous irregular pores was observed, along with surface functionalization of Fe_3O_4 due to Co_3O_4 nanoparticle agglomeration, which displayed a smooth and uniform morphology. The average particle size distributions were found to be 1949 nm, 1437 nm, and 1622 nm respectively. XRD analysis confirmed the successful synthesis of Fe_3O_4 and Co_3O_4 NPs, as well as Fe_3O_4/Co_3O_4 NCs, revealing planes indicative of a high degree of crystallinity in the iron oxide phase and a cubic spinel structure for cobalt oxide. Multiple diffraction peaks corresponding to the spinel structures of both Fe_3O_4 and Co_3O_4 were observed, with crystallite sizes determined to be 31.02 nm for Fe_3O_4, 19.05 nm for Co_3O_4, and 24.2 nm for Fe_3O_4/Co_3O_4 NCs. The photocatalytic degradation studies of maximum degradation efficiency for CR 93.65%, 92.57%, 96.13% and degradation efficiency for MG 91.39%, 90.57%, 94.40% by biosynthesized pure Fe_3O_4 NPs, Co_3O_4 NPs and Fe_3O_4/Co_3O_4 NCs reached under optimal conditions. Kinetic studies of CR and MG degradation rates revealed high correlation coefficients (R^2) close to unity (0.995) for CR degradation by pure Fe_3O_4 NPs and (R^2 = 0.991, 0.969) for MG degradation by Fe_3O_4 and Co_3O_4 NPs follow pseudo-zero-order kinetics. Degradation for CR (R^2 = 0.991) by pure Co_3O_4 NPs and (R^2 = 0.997) for MG degradation by Fe_3O_4/Co_3O_4 NCs follow pseudo-first-order kinetics and degradation for MG (R^2 = 0.988) for CR degradation by Fe_3O_4/Co_3O_4

NCs follow pseudo-second-order kinetics. The reusability and stability of the biosynthesized nanocatalysts were evaluated, showing efficient catalytic performance with a slight decrease in degradation rate multiple uses. The results from this study demonstrate the highest photocatalytic activity of biosynthesized Fe_3O_4/Co_3O_4 NCs provides a cost-effective, environmentally friendly, and high potential for the photocatalytic degradation of toxic organic dyes in environmental remediation exertions.

5.2. Recommendation

Based on the major findings of the current study the following recommendations are forwarded for future work. The ideas that have to be recommended further are:

- Future studies should consider the utilization of biosynthesized pure Fe_3O_4, Co_3O_4 NPs, and Fe_3O_4/Co_3O_4 NCs as photocatalysts for degrading commercial dyes in wastewater treatment applications.
- For further research, a comprehensive characterization of biosynthesized pure Fe_3O_4, Co_3O_4 NPs, and Fe_3O_4/Co_3O_4 NCs is needed to fully investigate the particle size and detailed morphology of the prepared samples. Therefore, the samples should undergo characterization using Transmission Electron Microscopy (TEM) to provide detailed information. Additionally, the elemental distribution of the synthesized samples should be analyzed using Energy Dispersive X-Ray (EDX) spectroscopy.
- Further research is required to identify and analyze the intermediate products that are produced during the degradation of dyes to fully understand their characteristics.

REFERENCES

1. Aroob, S.; Carabineiro, S. A.; Taj, M. B.; Bibi, I.; Raheel, A.; Javed, T.; ... & Sillanpää, M. Green synthesis and photocatalytic dye degradation activity of CuO nanoparticles. *Catalysts*. **2023**, 13(3), 502.
2. Pinheiro, L. R. S.; Gradíssimo, D. G.; Xavier, L. P. & Santos, A. V. Degradation of azo dyes: bacterial potential for bioremediation. *Sustainability*. **2022**, 14(3), 1510.
3. Rauf, M. A. & Ashraf, S. S. Fundamental principles and application of heterogeneous photocatalytic degradation of dyes in solution. *Chemical engineering journal*. **2009**, 151(1-3), 10-18.
4. Zhuang, Y.; Zhu, Q.; Li, G.; Wang, Z.; Zhan, P.; Ren, C.; ... & Qin, P. Photocatalytic degradation of organic dyes using covalent triazine-based framework. *Materials Research Bulletin*. **2022**, 146, 111619.
5. Sibhatu, A. K.; Weldegebrieal, G. K.; Sagadevan, S.; Tran, N. N. & Hessel, V. Photocatalytic activity of CuO nanoparticles for organic and inorganic pollutants removal in wastewater remediation. *Chemosphere*. **2022**, 300, 134623.
6. Aarthye, P. & Sureshkumar, M. Green synthesis of nanomaterials: An overview. *Materials Today: Proceedings*. **2021**, 47, 907-913.
7. Bukhari, A.; Ijaz, I.; Gilani, E.; Nazir, A.; Zain, H.; Saeed, R.; Alarfaji, S.S.; Hussain, S.; Aftab, R. & Naseer, Y. Green Synthesis of Metal and Metal Oxide Nanoparticles Using Different Plants' Parts for Antimicrobial Activity and Anticancer Activity: A Review Article. *Coatings.* **2021**, 11, 1374.
8. Sacco, O.; Stoller, M.; Vaiano, V.; Ciambelli, P.; Chianese, A. & Sannino, D. Photocatalytic degradation of organic dyes under visible light on N-doped TiO_2 photocatalysts. *International Journal of Photoenergy*. **2012**, (1), 626759.
9. Falcaro, P.; Ricco, R.; Yazdi, A.; Imaz, I.; Furukawa, S.; Maspoch, D.; Ameloot, R.; Evans, J. D. & Doonan, C. J. Application of metal and metal oxide nanoparticles@MOFs. *Coordination Chemistry Reviews*. **2016**, 307, 237-254.
10. Rasmussen, J.W.; Martinez, E.; Louka, P. & Wingett, D.G. Zinc oxide nanoparticles for selective destruction of tumor cells and potential for drug delivery applications. *Expert Opinion on Drug Delivery*. **2010**, 7, 1063-1077.

11. Valášková, M.; Tokarský, J.; Pavlovský, J.; Prostějovský, T. & Kočí, K. α-Fe_2O_3 Nanoparticles/Vermiculite Clay Material: Structural, Optical and Photocatalytic Properties. *Materials*. **2019**, 12(11), 1880.
12. Liu, Y.; Sun, N.; Hu, J.; Li, S. & Qin, G. Photocatalytic degradation properties of α-Fe_2O_3 nanoparticles for dibutyl phthalate in aqueous solution system. *Royal Society open science*. **2018**, 5(4), 172196.
13. Dewi, N. O. M.; Yulizar, Y. & Apriandanu, D. B. Green synthesis of Co_3O_4 nanoparticles using Euphorbia heterophylla L. leaves extract: characterization and photocatalytic activity. In *IOP Conference Series: Materials Science and Engineering*. **2019**, 509, 1, 012105.
14. Ngnintedem Yonti, C.; Kenfack Tsobnang, P.; Lontio Fomekong, R.; Devred, F.; Mignolet, E.; Larondelle, Y.; Hermans, S.; Delcorte, A. & Lambi Ngolui, J. Green Synthesis of Iron-Doped Cobalt Oxide Nanoparticles from Palm Kernel Oil via Co-Precipitation and Structural Characterization. *Nanomaterials*. **2021**, 11(11), 2833.
15. Safdar, A.; Mohamed, H. E. A.; Hkiri, K.; Muhaymin, A. & Maaza, M. Green synthesis of cobalt oxide nanoparticles using hyphaene thebaica fruit extract and their photocatalytic application. *Applied Sciences*. **2023**, 13(16), 9082.
16. Pavel, M.; Anastasescu, C.; State, R. N.; Vasile, A.; Papa, F. & Balint, I. Photocatalytic degradation of organic and inorganic pollutants to harmless end products: assessment of practical application potential for water and air cleaning. *Catalysts*. **2023**, 13(2), 380.
17. Ghogar, A.; Jiraungkoorskul, K. & Jiraungkoorskul, W. Paper Flower, Bougainvillea spectabilis: Update properties of traditional medicinal plant. *Journal of Natural Remedies*. **2016**, 82-87.
18. S. Senapati. Biosynthesis and immobilization of nanoparticles and their applications, Ph.D. thesis, University of Pune, Mumbai. (**2005**)
19. Banuraman, S. & Meikandaan, T. P. Treatability study of tannery effluent by enhanced primary treatment. *International Journal of Modern Engineering Research*. **2013**, 3(1), 119-122.
20. Hussain, I.; Singh, N. B.; Singh, A.; Singh, H. & Singh, S. C. Green synthesis of nanoparticles and its potential application. *Biotechnology letters*. **2016**, 38, 545-560.
21. Baker, S.; Harini, B.; Rakshith, D. & Satish, S. Marine microbes: Invisible nano factories. *Journal of Pharmacy Research*. **2013**, 6(3), 383-388.

22. Parveen, K.; Banse, V. & Ledwani, L. Green synthesis of nanoparticles: Their advantages and disadvantages. In *AIP conference proceedings*. **2016**, 1, 1724.
23. Ashour, M.; Mansour, A.T.; Abdelwahab, A.M. & Alprol, A.E. Metal Oxide Nanoparticles' Green Synthesis by Plants: Prospects in Phyto- and Bioremediation and Photocatalytic Degradation of Organic Pollutants. *Processes*. **2023**, 11, 3356.
24. Joshi, N. C.; Gururani, P. & Gairola, S. P. Metal oxide nanoparticles and their nanocomposite-based materials as photocatalysts in the degradation of dyes. *Biointerface Research in Applied Chemistry*. **2022**, 12(5), 6557-6579.
25. Goswam, B. & Mahanta, D. Fe_3O_4-Polyaniline Nanocomposite for Non-enzymatic Electrochemical Detection of 2, 4-Dichlorophenoxyacetic Acid. *ACS Omega*. **2021**, 6(27), 17239-17246.
26. Yew, Y.P.; Shamel, K.; Miyake, M.; Kuwano, N.; Khairudin, N.B.A.; Mahamad, S.E. & Lee, K.X. Green Synthesis of Magnetite (Fe_3O_4) Nanoparticles Using Seaweed (*Kappaphycus alvarezii*) Extract. *Nanoscale Research Letters*. **2016**, 11, 276.
27. Pandurang, A. Electrochromic thin films and devices, in Transition Metal Oxide Thin Film based Chromogenics and Devices. *Elsevier*. **2017**, 73–151.
28. Pagar, T.; Ghotekar, S.; Pagar, K.; Pansambal, S. & D, R.O. A Review on Bio-Synthesized Co_3O_4 Nanoparticles using Plant Extracts and Their Diverse Applications. *Journal of Chemical Reviews*. **2019**, 1(4), 260-270.
29. Huston, M.; DeBella, M.; DiBella, M. & Gupta, A. Green Synthesis of Nanomaterials. *Nanomaterials*. **2021**, 11, 2130.
30. Thunugunta, T.; Reddy, A. & Reddy D.C., L. Green synthesis of nanoparticles: current prospectus. *Nanotechnology Reviews*. **2015**, 4(4), 303-323.
31. Nadaroğlu, H.; Güngör, A. & İnce, S. Synthesis of Nanoparticles by Green Synthesis Method. *International Journal of Innovative Research and Reviews (INJIRR)*. **2017**, 1(1), 6-9.
32. Jafarzadeh, S.; Nooshkam, M.; Zargar, M.; Garavand, F.; Ghosh, S.; Hadidi, M. & Forough, M. Green synthesis of nanomaterials for smart biopolymer packaging: challenges and outlooks. *Journal of Nanostructure in Chemistry*. **2024**, 14(2), 113-136.
33. Ali, A.; Zafar, H.; Zia, M.; ul Haq, I.; Phull, A. R.; Ali, J. S. & Hussain, A. Synthesis, characterization, applications, and challenges of iron oxide nanoparticles. *Nanotechnology, science and applications*. **2016**, 49-67.

34. A. Vogel, C.F.A.; Charrier, J.G.; Wu, D.; McFall, A.S.; Wen Li, Abid, A.; M, I.; et al. Physicochemical properties of iron oxide nanoparticles that contribute to cellular ROS-dependent signaling and acellular production of hydroxyl radical. *Free Radical Research*. **2016**, 50(11), 1153-1164.
35. Zhu, N.; Ji, H.; Yu, P.; Niu, J.; Farooq, M. U.; Akram, M. W.; Udego, I. O.; Li, H. & Niu, X. Surface Modification of Magnetic Iron Oxide Nanoparticles. *Nanomaterials*. **2018**, 8(10), 810.
36. Sun, S. N.; Wei, C.; Zhu, Z. Z.; Hou, Y. L.; Venkatraman, S. S. & Xu, Z. C. Magnetic iron oxide nanoparticles: Synthesis and surface coating techniques for biomedical applications. *Chinese Physics B*. **2014**, 23(3), 037503.
37. Shahabuddin, S.; Sarih, N. M.; Mohamad, S. & Baharin, S. N. A. Synthesis and characterization of Co_3O_4 nanocube-doped polyaniline nanocomposites with enhanced methyl orange adsorption from aqueous solution. *RSC advances*. **2016**, 6(49), 43388-43400.
38. Shahid, M. M.; Pandikumar, A.; Golsheikh, A. M.; Huang, N. M. & Lim, H. N. Enhanced electrocatalytic performance of cobalt oxide nanocubes incorporating reduced graphene oxide as a modified platinum electrode for methanol oxidation. *RSC Advances*. **2014**, 4(107), 62793-62801.
39. Raman, V.; Suresh, S.; Savarimuthu, P. A.; Raman, T.; Tsatsakis, A. M.; Golokhvast, K. S. & Vadivel, V. K. Synthesis of Co_3O_4 nanoparticles with block and sphere morphology, and investigation into the influence of morphology on biological toxicity. *Experimental and therapeutic medicine*. **2016**, 11(2), 553-560.
40. Chen, Q.; Su, K.; Zhang, M. & Ma, Q. Fe_3O_4/Co_3O_4 core-shell nanocomposites modified structure and properties of heavy metal oxide diamagnetic glasses. *Journal of Non-Crystalline Solids*. **2019**, 509, 10–22.
41. Al-Senani, G. M. & Al-Saeedi, S. I. The use of synthesized CoO/Co_3O_4 nanoparticles as a corrosion inhibitor of low-carbon steel in 1 M HCl. *Materials*. **2022**, 15(9), 3129.
42. Abu-Dief, A. M. & Abdel-Fatah, S. M. Development and functionalization of magnetic nanoparticles as powerful and green catalysts for organic synthesis. *Beni-Suef University Journal of Basic and Applied Sciences*. **2018**, 7(1), 55-67.
43. Yew, Y. P.; Shameli, K.; Miyake, M.; Khairudin, N. B. B. A.; Mohamad, S. E. B.; Naiki, T., & Lee, K. X. Green biosynthesis of superparamagnetic magnetite Fe_3O_4 nanoparticles

and biomedical applications in targeted anticancer drug delivery system: A review. *Arabian Journal of Chemistry*. **2020**, 13(1), 2287-2308.

44. Rajendran, R. & Mani, A. Photocatalytic, antibacterial and anticancer activity of silver-doped zinc oxide nanoparticles. *Journal of Saudi Chemical Society*. **2020**, 24(12), 1010-1024.
45. Yadav, S.; Rani, N. & Saini, K. A review on transition metal oxides based nanocomposites, their synthesis techniques, different morphologies and potential applications. In *IOP Conference Series: Materials Science and Engineering*. **2022**, 1225, 1, 012004.
46. Yulizar, Y.; Bakri, R.; Apriandanu, D. O. B. & Hidayat, T. ZnO/CuO nanocomposite prepared in one-pot green synthesis using seed bark extract of Theobroma cacao. *Nano-Structures & Nano-Objects*. **2018**, 16, 300-305.
47. Madhusudhan, K. N.; Vinayarani, G.; Moorthy, S. M.; Satish, L.; Maheshwari, C.; Prakash, H. S.; ... & Sivaprasad, V. Isolation, purification and characterization of antibacterial bioactive compounds from Bougainvillea spectabilis Leaf. *Journal of Pharmacognosy and Phytochemistry*. **2019**, 8(3), 2668-2673.
48. Kenari, R. E. & Razavi, R. Encapsulation of bougainvillea (*Bougainvillea spectabilis*) flower extract in Urtica dioica L. Seed gum: Characterization, antioxidant/antimicrobial properties, and in vitro digestion. *Food Science & Nutrition*. **2022**, 10(10), 3436-3443.
49. Silveira, E.; Marques, P.; Silva, S.; Lima-Filho, J.; Porto, A. & Tambourgi, E. Selection of Pseudomonas for industrial textile dyes decolourization. *International Biodeterioration & Biodegradation*. **2009**, 63(2), 230-235.
50. Gautam, D.; Kumari, S.; Ram, B.; Chauhan, G. S. & Chauhan, K. A new hemicellulose-based adsorbent for malachite green. *Journal of Environmental Chemical Engineering*. **2018**, 6(4), 3889-3897.
51. Swan, N. B. & Zaini, M. A. A. Adsorption of malachite green and congo red dyes from water: recent progress and future outlook. *Ecological chemistry and engineering S*. **2019**, 26(1), 119-132.
52. Benkhaya, S.; M'rabet, S. & El Harfi, A. A review on classifications, recent synthesis and applications of textile dyes. *Inorganic Chemistry Communications*. **2020**, 115, 107891.

53. Chowdhury, A. P.; Anantharaju, K. S.; Keshavamurthy, K. & Rokhum, S. L. Recent Advances in Efficient Photocatalytic Degradation Approaches for Azo Dyes. *Journal of Chemistry*. **2023**, (1), 9780955.
54. Nazim, M.; Khan, P.; Asiri, A.M. & Kim, H. Exploring Rapid Photocatalytic Degradation of Organic Pollutants with Porous CuO Nanosheets: Synthesis, Dye Removal, and Kinetic Studies at Room Temperature. *ACS Omega*. **2021**, 6(4), 2601−2612.
55. Tejashwini, D.; Harini, H.; Nagaswarupa, H.; Naik, R.; Deshmukh, V. & Basavaraju, N. An in-depth exploration of eco-friendly synthesis methods for metal oxide nanoparticles and their role in photocatalysis for industrial dye degradation. *Chemical Physics Impact*. **2023**, 7, 100355.
56. Madan, S.; Shaw, R.; Tiwari, S. & Tiwari, S. K. Adsorption dynamics of Congo red dye removal using ZnO functionalized high silica zeolitic particles. *Applied Surface Science*. **2019**, 487, 907-917.
57. Sasmal, D.; Maity, J.; Kolya, H. & Tripathy, T. Study of congo red dye removal from its aqueous solution using sulfated acrylamide and N, N- dimethyl acrylamide grafted amylopectin. *Journal of Water Process Engineering*. **2017**, 18, 7-19.
58. Kumar, A. & Pandey, G. A review on the factors affecting the photocatalytic degradation of hazardous materials. *Material Science and Engineering International Journal*. **2017**, 1(3), 1-10.
59. Chiu, Y. H.; Chang, T. F. M.; Chen, C. Y.; Sone, M. & Hsu, Y. J. Mechanistic insights into photodegradation of organic dyes using heterostructure photocatalysts. *Catalysts*. **2019**, 9(5), 430.
60. Ahmed, S.; Rasul, M. G.; Brown, R. & Hashib, M. A. Influence of parameters on the heterogeneous photocatalytic degradation of pesticides and phenolic contaminants in wastewater: a short review. *Journal of environmental management*. **2011**, 92(3), 311-330.
61. Akpan, U. G. & Hameed, B. H. Parameters affecting the photocatalytic degradation of dyes using TiO_2-based photocatalysts: a review. *Journal of hazardous materials*. **2009**, 170(2-3), 520-529.
62. Venkatesan, S.; Suresh, S.; Ramu, P.; Arumugam, J.; Thambidurai, S. & Pugazhenthiran, N. Methylene blue dye degradation potential of zinc oxide nanoparticles bioreduced using Solanum trilobatum leaf extract. *Results in Chemistry*. **2022**, 4, 100637.

63. You, H.; Wu, Z.; Jia, Y.; Xu, X.; Xia, Y.; Han, Z. & Wang, Y. High-efficiency and mechano-/photo- bi-catalysis of piezoelectric-ZnO@ photoelectric-TiO_2 core-shell nanofibers for dye decomposition. *Chemosphere*. **2017**, 183, 528-535.
64. Sartape, A. S.; Mandhare, A. M.; Jadhav, V. V.; Raut, P. D.; Anuse, M. A. & Kolekar, S. S. Removal of malachite green dye from aqueous solution with adsorption technique using Limonia acidissima (wood apple) shell as low-cost adsorbent. *Arabian Journal of Chemistry*. **2017**, 10, S3229-S3238.
65. Yadav, S.; Shakya, K.; Gupta, A.; Singh, D.; Chandran, A. R.; Varayil Aanappalli, A., ... & Saini, K. A review on degradation of organic dyes by using metal oxide semiconductors. *Environmental Science and Pollution Research*. **2023**, 30(28), 71912-71932.
66. Khan, I.; Saeed, K.; Ali, N.; Khan, I.; Zhang, B. & Sadiq, M. Heterogeneous photodegradation of industrial dyes: An insight to different mechanisms and rate affecting parameters. *Journal of environmental chemical engineering*. **2020**, 8(5), 104364.
67. Mahdiani, M.; Soofivand, F.; Ansari, F. & Salavati-Niasari, M. Grafting of $CuFe_{12}O_{19}$ nanoparticles on CNT and graphene: Eco-friendly synthesis, characterization and photocatalytic activity. *Journal of Cleaner Production*. **2018**, 176, 1185–1197.
68. Khorshidi, N.; Khorrami, S.; Olya, M. & Mottiee, F. Photodegradation of Basic Dyes using Nanocomposite (Silver Zinc Oxide-Copper Oxide) and Kinetic Studies. *Oriental Journal of Chemistry*. **2016**, 32, 1205–1214.
69. Vasanth Kumar, K.; Porkodi, K. & Selvaganapathi, A. Constrain in solving Langmuir–Hinshelwood kinetic expression for the photocatalytic degradation of Auramine O aqueous solutions by ZnO catalyst. *Dyes Pigments*. **2007**, 75, 246–249.
70. Lanjwani, M. F.; Tuzen, M.; Khuhawar, M. Y. & Saleh, T. A. Trends in photocatalytic degradation of organic dye pollutants using nanoparticles: a review. *Inorganic Chemistry Communications*. **2024**, 159, 111613.
71. Bharathi, D.; Kalaichelvan, P. T.; Atmaram, V. & Anbu, S. Biogenic synthesis of silver nanoparticles from aqueous flower extract of *Bougainvillea spectabilis* and their antibacterial activity. *Journal of Medicinal Plants Studies*. **2016**, 4(5), 248-252.
72. Khaghani, S.; Ghanbari, D. & Khaghani, S. Green synthesis of iron oxide palladium nanocomposites by pepper extract and its application in removing of colored pollutants from waste. *Jornal of nanostructure*. **2017**, 7(3), 175-182.

73. Honarmand, M. & Mahjoore, M. Sunlight-Assisted Degradation of Bromocresol Green Using Co_3O_4 Nanoparticles as a High-Performance Photocatalyst. *Journal of Geomine*. **2023**, 1(1), 7-12.
74. Albeladi, A.; Khan, Z.; Al-Thabaiti, S. A.; Patel, R.; Malik, M. A. & Mehta, S. Fe_3O_4-CdO Nanocomposite for Organic Dye Photocatalytic Degradation: Synthesis and Characterization. *Catalysts*. **2024**, 14(1), 71.
75. Haghir Ebrahim Abadi, A. & Bagheri-Mohagheghi, M. M. Study of structure, morphology, optical absorption, and gap modulation of Activated carbon (AC)/NiO, Fe_3O_4, and Co_3O_4 oxide nanocomposites. *Progress in Physics of Applied Materials*. **2023**, 3(1), 15-28.
76. Sundar, L. S.; Singh, M. K.; Pereira, A. M. & Sousa, A. C. The cobalt oxide-based composite nanomaterial synthesis and its biomedical and engineering applications. In *Cobalt Compounds and Applications*. IntechOpen. (**2019**)
77. Abhilash, M. R.; Akshatha, G. & Srikantaswamy, S. Photocatalytic dye degradation and biological activities of the Fe_2O_3/Cu_2O nanocomposite. *RSC advances*. **2019**, 9(15), 8557-8568.
78. Dwivedi, P.; Jatrana, I.; Khan, A. U.; Khan, A. A.; Satiya, H.; Khan, M.; ... & Alam, M Photoremediation of methylene blue by biosynthesized ZnO/Fe_3O_4 nanocomposites using Callistemon viminalis leaves aqueous extract: a comparative study. *Nanotechnology Reviews*. **2021**, 10(1), 1912-1925.
79. Safdar, A.; Mohamed, H. E. A.; Hkiri, K.; Muhaymin, A. & Maaza, M. Green synthesis of cobalt oxide nanoparticles using hyphaene thebaica fruit extract and their photocatalytic application. *Applied Sciences*. **2023**, 13(16), 9082.
80. Alkanad, K.; Hezam, A.; Shekar, G. S.; Drmosh, Q. A.; Kala, A. A.; AL-Gunaid, M. Q. & Lokanath, N. K. Magnetic recyclable α-Fe_2O_3–Fe_3O_4/Co_3O_4–CoO nanocomposite with a dual Z-scheme charge transfer pathway for quick photo-Fenton degradation of organic pollutants. *Catalysis Science and Technology*. **2021**, 11(9), 3084-3097.
81. Yusefi, M.; Shameli, K.; Ali, R. R.; Pang, S. W. & Teow, S. Y. Evaluating anticancer activity of plant-mediated synthesized iron oxide nanoparticles using Punica granatum fruit peel extract. *Journal of Molecular Structure*. **2020**, 1204, 127539.
82. Aaga, G. F. & Anshebo, S. T. Green synthesis of highly efficient and stable copper oxide nanoparticles using an aqueous seed extract of Moringa stenopetala for sunlight-assisted catalytic degradation of Congo red and alizarin red s. *Heliyon*. **2023**, 9(5).

83. Karthik, K.; Dhanuskodi, S.; Gobinath, C.; Prabukumar, S. & Sivaramakrishnan, S. Multifunctional properties of microwave assisted CdO–NiO–ZnO mixed metal oxide nanocomposite: enhanced photocatalytic and antibacterial activities. *Journal of Materials Science: Materials in Electronics*. **2018**, 29, 5459-5471.

APPENDICES

Appendix 1: Effect of Photocatalyst Dosage

Photocatalytic degradation of CR and MG by biosynthesized pure Fe_3O_4 NPs, degradation condition for CR with volume of sample 25 mL, A_0 = 0.646, concentration 20 ppm, and a volume of sample 25 mL, A_0 = 1.464, concentration 15 ppm for MG at different photocatalyst dosage

Photocatalyst dosage in grams (g)	Absorbance (A_t) for CR	Degradation percentage (%)	Photocatalyst dosage in grams (g)	Absorbance (A_t) for MG	Degradation percentage (%)
0.01	0.324	49.85	0.01	0.549	62.5
0.03	0.149	76.93	0.03	0.301	79.44
0.06	0.095	85.29	0.06	0.178	87.84
0.09	0.072	88.85	0.09	0.198	86.48
0.12	0.083	87.15	0.12	0.212	85.52
0.15	0.091	85.91	0.15	0.23	84.29

Photocatalytic degradation of CR and MG by biosynthesized pure Co_3O_4 NPs, degradation condition for CR with volume of sample 25 mL, A_0 = 0.646, concentration 20 ppm, and a volume of sample 25 mL, A_0 = 1.464, concentration 15 ppm for MG at different photocatalyst dosage

Photocatalyst dosage in grams (g)	Absorbance (A_t) of CR	Degradation percentage (%)	Photocatalyst dosage in grams (g)	Absorbance (A_t) of MG	Degradation percentage (%)
0.01	0.331	48.76	0.01	0.594	59.43
0.03	0.176	72.76	0.03	0.309	78.89

0.06	0.108	83.28	0.06	0.206	85.93
0.09	0.078	87.93	0.09	0.226	84.56
0.12	0.086	86.69	0.12	0.246	83.20
0.15	0.096	85.14	0.15	0.261	82.17

Photocatalytic degradation of CR and MG by biosynthesized Fe_3O_4/Co_3O_4 NCs, degradation condition of CR with volume of sample 25 mL, A_0 = 0.646, concentration 20 ppm, and a volume of sample 25 mL, A_0 = 1.464, concentration 15 ppm for MG at different photocatalyst dosage

Photocatalyst dosage in grams (g)	Absorbance (A_t) of CR	Degradation percentage (%)	Photocatalyst dosage in grams (g)	Absorbance (A_t) of MG	Degradation percentage (%)
0.01	0.212	67.18	0.01	0.367	74.93
0.03	0.125	80.65	0.03	0.219	85.04
0.06	0.058	91.02	0.06	0.132	90.98
0.09	0.04	93.81	0.09	0.15	89.75
0.12	0.047	92.72	0.12	0.165	88.73
0.15	0.056	91.33	0.15	0.181	87.64

Appendix 2: Effect of Initial Concentration of CR and MG

Photocatalytic degradation of CR and MG by biosynthesized pure Fe_3O_4 NPs, degradation condition of CR with photocatalyst dosage 0.09 gm/25 mL, A_0 = 0.646 and photocatalyst dosage 0.06 gm/25 mL, A_0 = 1.464 for MG at the different initial concentration

Initial concentration (ppm)	Absorbance (A_t) of CR	Degradation percentage (%)	Initial concentration (ppm)	Absorbance (A_t) of MG	Degradation percentage (%)

5	0.009	89.29	5	0.033	88.09
10	0.03	89.40	10	0.102	88.40
15	0.046	89.71	15	0.163	88.87
20	0.065	89.94	20	0.248	87.90
25	0.097	88.82	25	0.346	86.89
30	0.134	87.70	30	0.458	85.66

Photocatalytic degradation of CR and MG by biosynthesized pure Co_3O_4 NPs, degradation condition of CR with photocatalyst dosage 0.09 gm/25 mL, A_0 = 0.646 and photocatalyst dosage 0.06 gm/25 mL, A_0 = 1.464 for MG at the different initial concentration

Initial concentration (ppm)	Absorbance (A_t) of CR	Degradation percentage (%)	Initial concentration (ppm)	Absorbance (A_t) of MG	Degradation percentage (%)
5	0.01	88.10	5	0.039	85.92
10	0.033	88.34	10	0.122	86.12
15	0.05	88.81	15	0.203	86.13
20	0.072	88.85	20	0.304	85.16
25	0.112	87.10	25	0.413	84.35
30	0.156	85.67	30	0.524	83.59

Photocatalytic degradation of CR and MG by biosynthesized Fe_3O_4/Co_3O_4 NCs, degradation condition of CR with photocatalyst dosage 0.09 gm/25 mL, A_0 = 0.646 and photocatalyst dosage 0.06 gm/25 mL, A_0 = 1.464 for MG at the different initial concentration

Initial concentration (ppm)	Absorbance (A_t) of CR	Degradation percentage (%)	Initial concentration (ppm)	Absorbance (A_t) of MG	Degradation percentage (%)
5	0.006	92.86	5	0.025	90.97
10	0.017	93.99	10	0.079	91.01
15	0.026	94.18	15	0.131	91.05
20	0.037	94.27	20	0.231	88.73
25	0.069	92.05	25	0.352	86.66
30	0.112	89.72	30	0.494	84.53

Appendix 3: Effect of Exposure Time

Photocatalytic degradation of CR and MG by biosynthesized pure Fe_3O_4 NPs, degradation condition of CR with photocatalyst dosage 0.09 gm/25mL, A_0 = 0.646, initial concentration 20 ppm, and photocatalyst dosage 0.06 gm/25mL, A_0 = 1.464, initial concentration 15 ppm for MG at different exposition time

Exposition time (minute)	Absorbance (A_t) of CR	Degradation percentage (%)	Exposition time (minute)	Absorbance (A_t) of MG	Degradation percentage (%)
15	0.154	76.16	15	0.354	75.82
30	0.132	79.57	30	0.324	77.87
45	0.102	84.21	45	0.265	81.90
60	0.074	88.54	60	0.216	85.25

75	0.053	91.80	75	0.168	88.52
90	0.054	91.64	90	0.136	90.71
105	0.055	91.49	105	0.137	90.64
120	0.055	91.49	120	0.137	90.64

Photocatalytic degradation of CR and MG by biosynthesized pure Co_3O_4 NPs, degradation condition of CR with photocatalyst dosage 0.09 gm/25mL, A_0 = 0.646, initial concentration 20 ppm, and photocatalyst dosage 0.06 gm/25mL, A_0 = 1.464, initial concentration 15 ppm for MG at different exposition time

Exposition time (minute)	Absorbance (A_t) of CR	Degradation percentage (%)	Exposition time (minute)	Absorbance (A_t) of MG	Degradation percentage (%)
15	0.159	75.39	15	0.395	73.02
30	0.132	79.57	30	0.361	75.34
45	0.105	83.75	45	0.318	78.28
60	0.074	88.54	60	0.237	83.81
75	0.059	90.87	75	0.179	87.77
90	0.06	90.71	90	0.161	89.00
105	0.061	90.56	105	0.161	89.00
120	0.061	90.56	120	0.161	89.00

Photocatalytic degradation of CR and MG by biosynthesized Fe_3O_4/Co_3O_4 NCs, degradation condition of CR with photocatalyst dosage 0.09 gm/25mL, A_0 = 0.646, initial concentration 20 ppm, and photocatalyst dosage 0.06 gm/25mL, A_0 = 1.464, initial concentration 15 ppm for MG at different exposition time

Exposition time (minute)	Absorbance (A_t) of CR	Degradation percentage (%)	Exposition time (minute)	Absorbance (A_t) of MG	Degradation percentage (%)
15	0.134	79.26	15	0.345	76.43
30	0.102	84.21	30	0.293	79.99
45	0.069	89.32	45	0.242	83.47
60	0.042	93.50	60	0.187	87.23
75	0.031	95.20	75	0.137	90.64
90	0.032	95.05	90	0.102	93.03
105	0.032	95.05	105	0.102	93.03
120	0.032	95.05	120	0.102	93.03

Appendix 4: Effect of pH

Photocatalytic degradation of CR and MG by biosynthesized pure Fe_3O_4 NPs, degradation condition for CR with photocatalyst dosage 0.09 gm/25 mL, A_0 = 0.646, initial concentration 20 ppm, exposure time 75 min, and photocatalyst dosage 0.06 gm/25 mL, A_0 = 1.464, initial concentration 15 ppm, exposure time 90 min for MG at different pH

pH	Absorbance (A_t) of CR	Degradation percentage (%)	pH	Absorbance (A_t) of MG	Degradation percentage (%)
2	0.116	82.04	2	0.322	78.01
4	0.065	89.94	4	0.236	83.88

6	0.041	93.65	6	0.226	84.56
8	0.087	86.53	8	0.186	87.30
10	0.132	79.57	10	0.126	91.39
12	0.152	76.47	12	0.323	77.94

Photocatalytic degradation of CR and MG by biosynthesized pure Co_3O_4 NPs, degradation condition for CR with photocatalyst dosage 0.09 gm/25 mL, A_0 = 0.646, initial concentration 20 ppm, exposure time 75 min, and photocatalyst dosage 0.06 gm/25 mL, A_0 = 1.464, initial concentration 15 ppm, exposure time 90 min for MG at different pH

pH	Absorbance (A_t) of CR	Degradation percentage (%)	pH	Absorbance (A_t) of MG	Degradation percentage (%)
2	0.142	78.02	2	0.338	76.91
4	0.121	81.27	4	0.292	80.05
6	0.091	85.91	6	0.244	83.33
8	0.048	92.57	8	0.171	88.32
10	0.087	86.53	10	0.138	90.57
12	0.124	80.80	12	0.204	86.07

Photocatalytic degradation of CR and MG by biosynthesized Fe_3O_4/Co_3O_4 NCs, degradation condition for CR with photocatalyst dosage 0.09 gm/25 mL, A_0 = 0.646, initial concentration 20 ppm, exposure time 75 min, and photocatalyst dosage 0.06 gm/25 mL, A_0 = 1.464, initial concentration 15 ppm, exposure time 90 min for MG at different pH

pH	Absorbance (A_t) of CR	Degradation percentage (%)	pH	Absorbance (A_t) of MG	Degradation percentage (%)

2	0.125	80.65	2	0.356	75.68
4	0.073	88.70	4	0.281	80.81
6	0.025	96.13	6	0.236	83.88
8	0.088	86.38	8	0.082	94.40
10	0.117	81.89	10	0.152	89.62
12	0.142	78.02	12	0.198	86.48

Appendix 5: Calibration Curve Data

Data for calibration curves of Congo red (CR) and Malachite green (MG) dyes

Initial Conc. of CR (ppm)	Absorbance (A_0) of CR	Initial Conc. of MG (ppm)	Absorbance (A_0) of MG
5	0.084	5	0.277
10	0.283	10	0.879
15	0.447	15	1.464
20	0.646	20	2.049
25	0.868	25	2.639
30	1.089	30	3.194

Appendix 6: Kinetic Data

To determine the photocatalytic degradation rate of CR and MG dye on the surface of the biosynthesized pure Fe_3O_4 NPs, Co_3O_4 NPs, and Fe_3O_4/Co_3O_4 NCs under sunlight irradiation, the kinetic data presented in Appendix 6 were analyzed based on the observed experimental data and plotted according to pseudo-zero-order, pseudo-first-order, and pseudo-second-order kinetic models.

Kinetics study modes						Zero - Order		First - Order	Second - Order
Photocatalyst	Dyes	Time (min)	Abs at time t. (A_t)	C_0 (ppm)	C_t (ppm)	$C_0 - C_t$	$\frac{C_0}{C_t}$	$\ln\frac{C_0}{C_t}$	$\frac{1}{C_t} - \frac{1}{C_0}$
Fe_3O_4 NPs	CR	15	0.154	20	7.081	12.918	2.824	1.038	0.091
		30	0.132	20	6.529	13.470	3.062	1.119	0.103
		45	0.102	20	5.777	14.222	3.461	1.242	0.123
		60	0.074	20	5.075	14.925	3.941	1.371	0.147
		75	0.053	20	4.548	15.451	4.397	1.481	0.170
	MG	15	0.354	15	5.551	9.449	2.702	0.994	0.113
		30	0.324	15	5.294	9.706	2.833	1.041	0.122
		45	0.265	15	4.789	10.210	3.132	1.142	0.142
		60	0.216	15	4.369	10.630	3.433	1.233	0.162
		75	0.168	15	3.959	11.040	3.788	1.332	0.186
		90	0.136	15	3.685	11.314	4.070	1.404	0.205
Co_3O_4 NPs	CR	15	0.159	20	7.207	12.793	2.775	1.021	0.089
		30	0.132	20	6.529	13.470	3.063	1.119	0.103
		45	0.105	20	5.853	14.147	3.417	1.229	0.121
		60	0.074	20	5.075	14.925	3.941	1.371	0.147
		75	0.059	20	4.699	15.301	4.256	1.448	0.163

	MG	15	0.395	15	5.902	9.098	2.542	0.933	0.103
		30	0.361	15	5.611	9.389	2.673	0.984	0.112
		45	0.318	15	5.243	9.757	2.861	1.051	0.124
		60	0.237	15	4.549	10.450	3.297	1.193	0.153
		75	0.179	15	4.053	10.946	3.701	1.309	0.180
		90	0.161	15	3.899	11.100	3.847	1.347	0.190
Fe_3O_4/ Co_3O_4 NCs	CR	15	0.134	20	6.580	13.420	3.040	1.112	0.102
		30	0.102	20	5.777	14.223	3.462	1.242	0.123
		45	0.069	20	4.950	15.050	4.041	1.396	0.152
		60	0.042	20	4.273	15.727	4.681	1.543	0.184
		75	0.031	20	3.997	16.003	5.004	1.610	0.200
	MG	15	0.345	15	5.474	9.526	2.740	1.00	0.116
		30	0.293	15	5.029	9.971	2.983	1.093	0.132
		45	0.242	15	4.592	10.407	3.266	1.184	0.151
		60	0.187	15	4.122	10.878	3.639	1.292	0.176
		75	0.137	15	3.694	11.306	4.061	1.401	0.204
		90	0.102	15	3.394	11.606	4.419	1.486	0.228

Appendix 7: Photocatalyst Reusability

Reusability of biosynthesized pure Fe_3O_4 NPs for the photocatalytic degradation of CR and MG at optimum condition

Number of cycles	Absorbance (At) of CR	Degradation efficiency %	Number of cycles	Absorbance (At) of MG	Degradation efficiency %
First	0.046	92.88	First	0.136	90.71
Second	0.053	91.80	Second	0.149	89.82
Third	0.065	89.94	Third	0.161	89.00
Fourth	0.073	88.70	Fourth	0.168	88.52

Reusability of biosynthesized pure Co_3O_4 NPs for the photocatalytic degradation of CR and MG at optimum condition

Number of cycles	Absorbance (At) of CR	Degradation efficiency %	Number of cycles	Absorbance (At) of MG	Degradation efficiency %
First	0.051	92.11	First	0.143	90.23
Second	0.056	91.18	Second	0.159	89.14
Third	0.065	89.94	Third	0.164	88.80
Fourth	0.071	89.01	Fourth	0.182	87.57

Reusability of biosynthesized Fe_3O_4/Co_3O_4 NCs for the photocatalytic degradation of CR and MG at optimum condition

Number of cycles	Absorbance (At) of CR	Degradation efficiency %	Number of cycles	Absorbance (At) of MG	Degradation efficiency %
First	0.032	95.05	First	0.089	93.92
Second	0.041	93.65	Second	0.097	93.37
Third	0.048	92.57	Third	0.112	92.35
Fourth	0.056	91.33	Fourth	0.139	90.51